A phase-field model of dislocations in ductile single crystals

Thesis by

Marisol Koslowski

In Partial Fulfillment of the Requirements

for the Degree of

Doctor of Philosophy

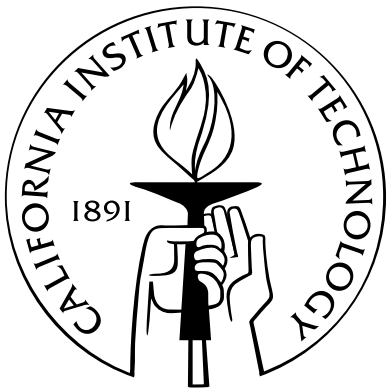

California Institute of Technology

Pasadena, California

2003

(Submitted December 6, 2002)

To Kasimir Kozlowski

Acknowledgements

I would like to express my gratitude to Professor Michael Ortiz, whose encouragement, guidance and ideas made this possible. I am also thankful to Professor Alberto Cuitiño, for his continuous support, collaboration and friendship.

It would be not fair to forget all the people in Ortiz's group, specially Marta, Lydia, Adrian, Matt, Rena, Olivier, Puru, Olga, Bill and John.

I will be eternally grateful to my husband, Alejandro, for his unconditional support and love.

The support of the DOE through Caltech's ASCI Center for the Simulation of the Dynamic Response of Materials is gratefully acknowledged.

Abstract

A phase-field theory of dislocations, strain hardening and hysteresis in ductile single crystals is developed. The theory accounts for an arbitrary number and arrangement of dislocation lines over a slip plane; the long-range elastic interactions between dislocation lines; the core structure of the dislocations; the interaction between the dislocations and an applied resolved shear stress field; and the irreversible interactions with short-range obstacles, resulting in hardening, path dependency and hysteresis.

We introduce a variational formulation for the statistical mechanics of dissipative systems. The influence of finite temperature as well as the mechanics in the phase-field theory are modeled with a Metropolis Monte Carlo algorithm and a mean field approximation.

A chief advantage of the present theory is that at zero temperature it is analytically tractable, in the sense that the complexity of the calculations may be reduced, with the aid of closed form analytical solutions, to the determination of the value of the phase field at point-obstacle sites.

The theory predicts a range of behaviors which are in qualitative agreement with observation, including hardening and dislocation multiplication in single slip under monotonic loading; the Bauschinger effect under reverse loading; the fading memory effect; the evolution of the dislocation density under cycling loading; temperature softening; strain rate dependence; and others.

The model also reproduces the formation of dislocation networks observed in grain boundaries for different crystal structures and orientations. Simultaneously with the stable configurations the theory naturally predicts the equilibrium dislocation density independently of initial values or sources.

Contents

List of Figures

Chapter 1

Introduction

Dislocation networks, grain boundaries, second-phase particles and their interactions are the key elements that govern the mechanical properties of materials. The properties of each individual element can be characterized from an atomistic point of view; on the other hand, the macroscopic properties of materials can be described by empirical laws based on experimental data. However, the ultimate goal should be to develop macroscopic constitutive laws based on the unit mechanisms that operate at the atomic scales. Phase-field representations are a promising approach to bridge that gap.

Theoretical, experimental and computational effort has been made to incorporate micro-mechanical features of the plastic flow into macroscopic modeling. See for example (4; 5; 6; 7) for reviews and (8; 9; 10) for more recent developments.

Phase-field models were originally developed to study phase transformations. Since then, they were used to simulate a wide variety of microscopic processes, such as mesoscopic microstructure evolution in multiphase systems, grain boundary evolution and solidification (11; 12). In continuum mechanics, phase-fields are widely used to model fracture, interfacial motion in the presence of strain, stress voiding, mixture of incompressible fluids, among others (13; 14; 15). More recently phase-fields have been extended to model dislocation dynamics (16; 17; 18).

Mesoscopic simulations of dislocations have been performed by Kubin (19), Ghoniem (20), Zbib (21; 22) among others. In these models the system and its dynamics are completely described by a geometry of dislocation lines. During the simulation process, all information concerning the individual dislocation segments has to be tracked in order to update the evolving system. The necessity of tracking each dislocation line and computing the force acting on each segment is the

most challenging and time-consuming part of this approach.

A clear advantage of a phase-field theory over other mesoscopic dislocation dynamic models is that the slip is represented by means of a scalar phase-field without the necessity of tracking individual dislocations at each time step. The value of the phase-field at a point may alternatively be regarded as recording the number of dislocations, with proper accounting for their sign, which have crossed the point. Thus, the individual dislocation lines may be identified with the lines over which the phase-field jumps by one. The phase-field approach furnishes a simple yet efficient means of representing arbitrary dislocation geometries, possibly involving very large numbers of individual dislocations.

Here we present the formulation of a phase-field theory of dislocations, strain hardening and hysteresis in ductile single crystals. The present theory accounts for an arbitrary number and arrangement of dislocation lines over a slip plane; the long-range elastic interactions between dislocation lines; the core structure of the dislocations described by means of a Peierls potential; the interaction between the dislocations and an applied resolved shear stress field; and the irreversible interactions with short-range obstacles and lattice friction, resulting in hardening, path dependency and hysteresis.

The central objective of the theory is to characterize the evolution of the phase-field. The theory is couched within a general variational framework for dissipative systems developed by Ortiz *et al.* (23; 24; 25; 26; 27), and accounts for energetic and kinetic effects.

In Chapter 2, we focus our attention on systems consisting of a dislocation ensemble moving within a single slip plane through a random array of discrete forest dislocations under the action of an applied shear stress. At zero temperature the phase-field can be obtained by direct minimization of the energy. A chief advantage is that *no numerical grid is required in calculations.* On the sole basis of the value of the phase-field at the obstacle sites, the theory reconstructs, analytically and in closed form, the location of—possibly large numbers of—discrete dislocation lines, often in complex arrangements and undergoing intricate topological transitions, and endows each dislocation line with a well-defined core. This allows to track the evolution of the dislocation lines and at the same time compute macroscopic values as plastic slip and dislocation density. This drastic reduction in complexity may open the way for embedding the theory within a finite-deformation formulation of single-crystal elastic-plastic behavior (e. g., (26; 28)), with a view to its use in large-scale finite

element calculations of macroscopic samples. By virtue of these attributes, the theory has many advantages in comparison to other recent phase-field models of dislocation dynamics (17), which require the use of large computational grids and time integration over large numbers of time steps.

In Chapter 3, we propose a generalization of classical statistical mechanics which describes the behavior of dissipative systems placed in contact with a heat bath. The interaction between dislocations and obstacles in the glide plane is dissipative in nature, resulting in path dependency and hysteresis. The central objective of this chapter is to characterize the evolution of the phase-field at finite temperatures. The dislocation ensemble is solved using a Path Integral Metropolis Monte Carlo algorithm and a mean field approximation. The model predicts a range of behaviors that are in agreement with experimental observation and results obtained by other methods in single crystals (29; 30; 31; 1).

Direct observation of dislocations and electron microscopy studies have shown that the distribution of dislocations is not random (2; 32; 33). Dislocations rearrange into configurations of lower energy forming patterns that have the form of dislocation sub-grains. In Chapter 4, we extend the phase-field theory of dislocations to a multicomponent phase-field, to study the formation of dislocation networks in twist boundaries. We use a Metropolis Monte Carlo algorithm in order to find the stable configurations of a stress-free grain boundary in crystals with different structures and orientations. The theory predicts the formation square and hexagonal patterns that are in agreement with the ones observed in twist boundaries (2; 32). Simultaneously with the stable configurations the theory naturally predicts the dislocation density with no initial dislocations or sources.

Chapter 2

A phase-field of dislocation dynamics, strain hardening and hysteresis in ductile single crystals

2.1 Introduction

This chapter is concerned with the formulation of an *exactly solvable* phase-field theory of dislocation dynamics, strain hardening and hysteresis in ductile single crystals. The present theory is an outgrowth of the phase-field model of crystallographic slip of Ortiz (34), which was restricted to a single dislocation loop moving through point obstacles of uniform strength and was based on a line-tension approximation. The present theory accounts for an arbitrary number and arrangement of dislocation lines over a slip plane; the long-range elastic interactions between dislocation lines; the core structure of the dislocations described by means of a Peierls potential; the interaction between the dislocations and an applied resolved shear stress field; and the irreversible interactions with short-range obstacles and lattice friction, resulting in hardening, path dependency and hysteresis.

A chief advantage of the present theory is that it is analytically tractable, in the sense that the complexity of the calculations may be reduced, with the aid of closed-form analytical solutions, to the determination of the value of the phase field at point-obstacle sites. In particular, *no numerical grid is required in calculations.* On the sole basis of the value of the phase field at the obstacle sites, the theory reconstructs, analytically and in closed form, the location of—possibly large numbers of—discrete dislocation lines, often in complex arrangements and undergoing intricate topological transitions, and endows each dislocation line with a well defined core. Furthermore, the theory

characterizes the equilibrium configurations of the dislocation ensemble directly, with the result that no short transients associated with artificial kinetics need to be resolved in calculations. By virtue of these attributes, the theory would appear to be advantageous in comparison to other recent phase-field models of dislocation dynamics (17; 20), which require the use of large computational grids and time integration over large numbers of time steps.

For definiteness, we restrict our attention to systems consisting of a dislocation ensemble moving within a single-slip plane through a random array of discrete forest dislocations under the action of an applied shear stress. In the present theory, the dislocation ensemble populating the slip plane is represented by means of a scalar phase field. Specifically, the value of the phase field at a point of the slip plane simply records the extent of slip in *quanta* of Burgers vector. The phase field is, therefore, integer valued, and its value at a point may alternatively be regarded as recording the number of dislocations, with proper accounting for their sign, which have crossed the point. Thus, the individual dislocation lines may be identified with the lines over which the phase field jumps by one. The phase-field approach furnishes a simple yet efficient means of representing arbitrary dislocation geometries, possibly involving very large numbers of individual dislocations, as well as enabling the tracking of intricate topological transitions, including loop nucleation, pinching and the formation of Orowan loops.

The central objective of the theory is to characterize the evolution of the phase field. The theory is couched within a general variational framework for dissipative systems developed by Ortiz *et al.* (23; 24; 25; 26; 27), and accounts for energetic and kinetic effects. The energy terms contemplated by the theory include the core energy of the dislocations, represented by a piecewise quadratic Peierls potential (7); the long-range elastic interactions between primary dislocations and between primary and forest dislocations; and the energy of interaction with the applied resolved shear stress. The particular piecewise quadratic form of the Peierls potential adopted here lends itself to an effective analytical treatment based on the Fourier transform (7). The main effect of the Peierls potential is to endow the dislocations with a well defined core energy and to coarse-grain the slip plane by suppressing wavelengths shorter than the lattice parameter.

At zero temperature and in the absence of irreversible processes, the equilibrium configurations of the dislocation ensemble follow directly from energy minimization. The resulting variational problem is strongly *nonlinear* owing to the all-important constraint that the phase field be an

integer-valued function. Furthermore, the minimization problem is *nonconvex* owing to the multiwell structure of the Peierls potential. In addition, the variational problem is *nonlocal*, owing to the presence of long-range elastic interactions. These attributes render the energy minimization problem mathematically nontrivial. Despite these difficulties, the choice of a piecewise quadratic Peierls potential lends the problem analytical tractability and a good deal of progress towards the solution can be made analytically.

In the present theory, hysteresis arises from the assumed irreversible short-range interactions between primary and forest dislocations and from lattice friction. The strength of some of these interactions has recently been investigated using atomistic and continuum models (35; 36; 37). Thus, we assume that the crossing of a forest-dislocation site by a primary dislocation always costs energy, regardless of the direction of the crossing. In the context of a phase-field representation, this is tantamount to assuming that any variation in the phase field at sites occupied by obstacles requires the supply of a certain amount of work, regardless of the sign of the variation. Physically, this work may be identified with the energy required to dissolve the dislocation–obstacle reaction product. Evidently, this form of interaction is irreversible and dissipative, and thus cannot be described by means of an energy function. It is possible, however, to develop an incremental variational framework which characterizes the evolution of the system by means of a sequence of minimization problems (23; 24; 25; 26; 27). The function to be minimized over a given step includes the incremental work of dissipation incurred as a result of obstacle crossings, and depends on the state of the system at the beginning of the step, which results in path-dependent and hysteretic behavior.

The theory predicts a range of behaviors which are in qualitative agreement with observation, including hardening and dislocation multiplication in single slip under monotonic loading; the Bauschinger effect under reverse loading; and the fading memory effect, whereby reverse yielding gradually eliminates the influence of previous loading. Simultaneously with the deformation and hardening characteristics of the system, the theory naturally predicts the evolution of the dislocation density. In particular, no independent equation of evolution for the dislocation density needs to be supplied.

2.2 Dislocation energies

In this section we derive explicit expressions for the energy of a dislocation ensemble contained within a slip plane in an elastic crystal. The dislocation ensemble is described by means of a phase field defined over the slip plane. In addition to the elasticity of the crystal, the slip plane is endowed with a piecewise quadratic Peierls interplanar potential. The elastic interaction energy formulated in this section is a special case of a general class of energies for continuously distributed dislocation loops in isotropic elastic crystals derived by Ortiz and Xu (38). Extensions to anisotropic crystals have also been given by Xu (39).

We consider a crystal undergoing deformations characterized by a displacement field u_i. Following Kröner (40), we begin by decomposing the displacement gradient in the additive form:

$$u_{i,j} = \beta^e_{ij} + \beta^p_{ij} \tag{2.1}$$

where $u_{i,j}$ is the displacement gradient, or distortion field, and, here and subsequently, commas are used to denote partial differentiation. For simplicity, we shall specifically focus on crystallographic slip occurring on a single slip plane S. Under these conditions, the plastic distortion β^p_{ij} is supported on S and has the form

$$\beta^p_{ij} = \delta_i \, m_j \, \delta_S \tag{2.2}$$

where δ_i is the displacement jump across S, $\boldsymbol{m}$ is the unit normal to S, and δ_S is the Dirac distribution supported on S. The elastic distortion β^e_{ij} is assumed to be continuous. Neither the elastic nor the plastic distortion is required to be compatible, i.e., to be a gradient.

We shall additionally assume that the energy of the dislocation ensemble may be written as the sum of three terms: a core energy expressible in terms of a Peierls interplanar potential; the elastic interaction energy of the dislocations; and the energy of interaction with the applied stress field. These assumptions lead to the consideration of an energy functional of the form:

$$E = \int_S \phi(\boldsymbol{\delta}) dS + \int \frac{1}{2} c_{ijkl} \beta^e_{ij} \beta^e_{kl} d^3x - \int_S t_i \delta_i dS \equiv E^{\text{core}} + E^{\text{int}} + E^{\text{ext}} \tag{2.3}$$

Here, ϕ denotes the Peierls interplanar potential and the first term in (2.3) represents the misfit or core energy of the dislocations. In the second term, which represents the elastic interaction energy,

c_{ijkl} are the elastic moduli of the crystal. Finally, the third term represents the interaction energy between the dislocations and a self-equilibrated applied stress field resulting in a distribution of tractions t_i over the slip plane. The aim now is to derive a phase-field representation of each of the terms in (2.3).

2.2.1 Elastic interaction energy

Suppose that the slip distribution δ_i over S, or equivalently, β^p_{ij}, is prescribed. The corresponding elastic interaction energy may then be computed as follows. Insertion of (2.1) into (2.3) and minimization with respect to the displacement field yields the equilibrium equations

$$(c_{ijkl}u_{k,l}),_j -(c_{ijkl}\beta^p_{kl}),_j = 0 \tag{2.4}$$

The corresponding displacement field is

$$u_k = -G_{ki} \star (c_{ijmn}\beta^p_{mn}),_j \tag{2.5}$$

where G_{ki} is the Green's function and $(\star)$ denotes the convolution operator. The distortion field then follows as

$$u_{k,l} = -G_{ki,l} \star (c_{ijmn}\beta^p_{mn}),_j \tag{2.6}$$

and the elastic distortion as

$$\beta^e_{kl} = -G_{ki,l} \star (c_{ijmn}\beta^p_{mn}),_j -\beta^p_{kl} \tag{2.7}$$

Finally, the elastic interaction energy E^{int} is obtained by inserting (2.7) into the second term of (2.3).

A convenient explicit expression for E^{int} may be obtained by recourse to the Fourier transform. Using the convolution theorem, the Fourier transform of the elastic distortion follows from (2.7) as

$$\hat{\beta}^e_{kl} = \hat{G}_{ki}k_jk_lc_{ijmn}\hat{\beta}^p_{mn} - \hat{\beta}^p_{kl} \tag{2.8}$$

where a superposed $(\hat{})$ denotes the Fourier transform of a function, k_i is the wavenumber vector,

and the Fourier transform of the Green's function is determined by the relation:

$$\hat{G}_{ik}^{-1} = c_{ijkl} k_j k_l \tag{2.9}$$

Finally, the interaction energy follows from an application of Parseval's identity, with the result:

$$E^{\text{int}} = \frac{1}{(2\pi)^3} \int \frac{1}{2} \hat{A}_{mnuv}(\boldsymbol{k}) \hat{\beta}^{p}_{mn}(\boldsymbol{k}) \hat{\beta}^{p*}_{uv}(\boldsymbol{k}) d^3k \tag{2.10}$$

Here the symbol $(*)$ denotes complex conjugation and we write

$$\begin{aligned} \hat{A}_{mnuv}(\boldsymbol{k}) &= c_{klrs} c_{ijmn} c_{pquv} (\hat{G}_{ki} k_j k_l - c^{-1}_{klij})(\hat{G}_{rp} k_q k_s - c^{-1}_{rspq}) & (2.11) \\ &= c_{mnuv} - c_{kluv} c_{ijmn} \hat{G}_{ki} k_j k_l & (2.12) \end{aligned}$$

Mura (41) has shown that E^{int} can also be expressed in terms of Nye's (42) dislocation density tensor. Indeed, it is readily verified from (2.8) and (2.9) that, if the plastic distortion β^p_{ij} is compatible, i.e., if it is a gradient, then the elastic distortions, and hence the elastic interaction energy, vanish identically.

In order to facilitate analysis we shall resort to several simplifying assumptions. Thus, for the special case of an isotropic crystal the Green's function reduces to

$$\hat{G}_{ij} = \frac{1}{2\mu} \left(\frac{2\delta_{ij}}{k^2} - \frac{1}{1-\nu} \frac{k_i k_j}{k^4} \right) \tag{2.13}$$

where μ is the shear modulus of the crystal, ν is its Poisson's ratio, and we write $k = |\boldsymbol{k}|$. The interaction energy (2.10) then simplifies to

$$E^{\text{int}} = \frac{1}{(2\pi)^3} \int \frac{\mu}{2} \left\{ [1 - (\boldsymbol{\eta} \cdot \boldsymbol{m})^2] |\hat{\boldsymbol{\delta}}|^2 - (\hat{\boldsymbol{\delta}} \cdot \boldsymbol{\eta})^2 + \frac{2}{1-\nu} (\hat{\boldsymbol{\delta}} \cdot \boldsymbol{\eta})^2 (\boldsymbol{\eta} \cdot \boldsymbol{m})^2 \right\} d^3k \tag{2.14}$$

where we write $\eta_i = k_i/k$. In addition, we shall adopt the constrained displacement hypothesis of Rice (43; 44) according to which displacements, and the attendant shear resistance, take place predominantly in the direction of the dominant Burgers vector, i.e.,

$$\delta_i(\boldsymbol{x}) = \delta(\boldsymbol{x})\, s_i \tag{2.15}$$

where $\boldsymbol{s} = \boldsymbol{b}/|\boldsymbol{b}|$ is a constant unit vector and δ is a scalar function. For certain crystals, this conjecture has found support in atomistic calculations (45; 46; 47; 48). By virtue of these assumptions, (2.14) simplifies to

$$E^{\text{int}} = \frac{1}{(2\pi)^3} \int \frac{\mu}{2} \left(\eta_2^2 + \frac{2}{1-\nu} \eta_1^2 \eta_3^2 \right) |\hat{\delta}|^2 d^3k \tag{2.16}$$

where we have chosen axes such that the slip plane is parallel to the (x_1, x_2)-plane and the Burgers vector points in the direction of the x_1-axis. Finally, for the particular case in which the slip distribution is confined to the plane $x_3 = 0$, the elastic interaction energy further reduces to

$$E^{\text{int}} = \frac{1}{(2\pi)^2} \int \frac{\mu}{4} \left(\frac{k_2^2}{\sqrt{k_1^2 + k_2^2}} + \frac{1}{1-\nu} \frac{k_1^2}{\sqrt{k_1^2 + k_2^2}} \right) |\hat{\delta}|^2 d^2k \tag{2.17}$$

which is the sought expression.

By way of a simple illustrative and verification example we may consider the case of an edge dislocation pileup, for which the slip distribution is of the form

$$\hat{\delta} = 2\pi b \, \delta_D(k_2) \hat{f}(k_1) \tag{2.18}$$

whence the elastic energy per unit length of dislocation follows from (2.17) as

$$\frac{E^{\text{int}}}{L} = \frac{\mu b^2}{4\pi(1-\nu)} \int_{-\infty}^{\infty} |k_1| |\hat{f}(k_1)|^2 dk_1 \tag{2.19}$$

For a single Volterra dislocation at the origin, $\hat{f}(k_1) = 1/ik_1$ and the elastic energy per unit length evaluates to

$$\frac{E^{\text{int}}}{L} = \frac{\mu b^2}{4\pi(1-\nu)} \int_{\pi/R}^{\pi/r_0} \frac{dk_1}{k_1} = \frac{\mu b^2}{4\pi(1-\nu)} \log \frac{R}{r_0} \tag{2.20}$$

where, in order to avoid logarithmic divergences, we have introduced lower and upper cutoff radii. We verify that (2.20) coincides with the well-known expression for the energy per unit length of a straight edge dislocation in an isotropic crystal (3). For a screw pileup, a similar derivation yields

$$\frac{E^{\text{int}}}{L} = \frac{\mu b^2}{4\pi} \int_{-\infty}^{\infty} |k_2| |\hat{f}(k_2)|^2 dk_2 \tag{2.21}$$

For a single screw dislocation at the origin the dislocation energy per unit length evaluates to

$$\frac{E^{\text{int}}}{L} = \frac{\mu b^2}{4\pi} \int_{\pi/R}^{\pi/r_0} \frac{dk_2}{k_2} = \frac{\mu b^2}{4\pi} \log \frac{R}{r_0} \tag{2.22}$$

which again coincides with the classical result (3).

2.2.2 Core energy

In the Peierls theory of the dislocation core, the interplanar potential $\phi(\boldsymbol{\delta})$ is identified with the energy per unit area that results when two semi-infinite crystals are taken through a relative rigid displacement δ_i. From symmetry considerations it follows that, in the absence of an applied field, the energy of the crystal attains minima when the displacement jump δ_i is an integral multiple of a Burgers vector b_i of the lattice, i.e., at

$$\delta_i = \xi\, b_i, \quad \xi \in \mathbb{Z} \tag{2.23}$$

where $\mathbb{Z}$ denotes the set of all integer numbers. These special slips determine the location of the wells of ϕ. With a view to enabling the application of Fourier transform methods, we shall assume that ϕ is piecewise quadratic (7). In this model, the interplanar potential is taken to be of the form

$$\phi(\boldsymbol{\delta}) = \min_{\xi \in \mathbb{Z}} \frac{1}{2} C_{jl} (\delta_j - \xi b_j)(\delta_l - \xi b_l) \tag{2.24}$$

The moduli C_{jl} may be determined by equating (2.24) with the energy per interatomic plane of a crystal undergoing a simple shear deformation of the form:

$$\beta_{ij} = \frac{1}{d} \delta_i m_j \tag{2.25}$$

where d is the interplanar distance. The result is

$$C_{ik} = \frac{1}{d} c_{ijkl} m_j m_l \tag{2.26}$$

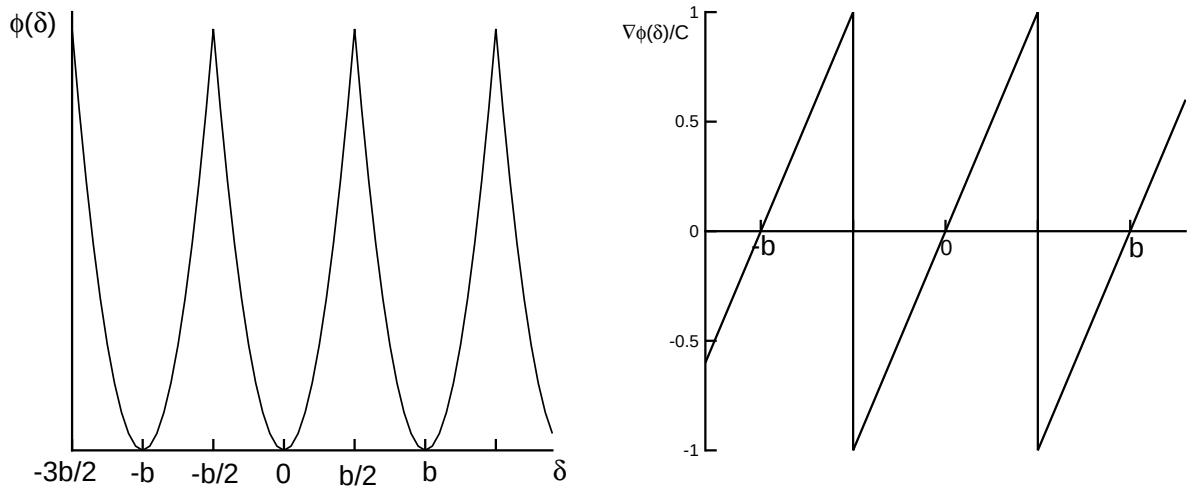

(a) Interplanar potential

(b) Resolved shear stress

Figure 2.1: Piecewise quadratic interplanar potential and its derivative.

By way of example we may consider the case of crystallographic slip on a {111}-plane of an fcc crystal. Then a simple calculation gives $d = a/\sqrt{3}$, with a the cubic lattice parameter, and

$$C_{ik} = \frac{1}{\sqrt{3}a}(c_{11} + c_{44} - c_{12})\delta_{ik} \tag{2.27}$$

In this expression c_{11}, c_{44} and c_{12} are the three independent cubic elastic moduli.

If the slip is additionally constrained to take place in the direction of the Burgers vector, as in Eq. (2.15), then the piecewise quadratic interplanar potential (2.24) reduces to the form

$$\phi(\delta) = \min_{\xi \in \mathbb{Z}} \frac{C}{2}|\delta - \xi b|^2 \tag{2.28}$$

where $\delta = \boldsymbol{\delta} \cdot \boldsymbol{s}$ and

$$C = C_{ik} s_i s_k \tag{2.29}$$

The function $\phi(\delta)$ and its derivative, which gives the resolved shear stress as a function of slip, are shown in Fig. 2.1.

2.2.3 Computation of the energy from the phase field

At zero temperature, the stable configurations of the dislocation ensemble may be identified with the relative minima of the energy (2.3). We begin by attempting a characterization of the absolute mimimizers of (2.3), and defer the more ambitious program of understanding the relative energy minimizers as well. Inserting (2.17) and (2.28) into (2.3) leads to the energy:

$$E[\zeta] = \inf_{\xi \in X} E[\zeta|\xi] \tag{2.30}$$

where

$$\zeta = \delta/b \tag{2.31}$$

is a normalized slip function, and

$$E[\zeta|\xi] = \int \frac{\mu b^2}{2d}|\zeta - \xi|^2 d^2x + \frac{1}{(2\pi)^2}\int \frac{\mu b^2}{4} K|\hat{\zeta}|^2 d^2k - \int bs\zeta d^2x \tag{2.32}$$

In this expression,

$$s = t_i m_i \tag{2.33}$$

is the resolved shear stress field, and we write

$$K = \frac{k_2^2}{\sqrt{k_1^2 + k_2^2}} + \frac{1}{1-\nu}\frac{k_1^2}{\sqrt{k_1^2 + k_2^2}} \tag{2.34}$$

The normalized slip distribution ζ of interest now follows from the problem:

$$\inf_{\zeta \in Y} E[\zeta] \tag{2.35}$$

In definition (2.30), the function ξ may be regarded as an integer-valued *phase field* defined on the slip plane S, with the property that $\xi(\boldsymbol{x})$ equals the number of dislocations which have passed over the point $\boldsymbol{x} \in S$. Thus, the quantized phase field ξ describes an ensemble of perfect, or Volterra, dislocations on S. In writing (2.30) and (2.35), $X \times Y$ denotes the space of slip distributions and integer-valued phase fields of finite energy, i.e., the linear space of functions $\zeta : \mathbb{R}^2 \to \mathbb{R}$ and $\xi : \mathbb{R}^2 \to \mathbb{Z}$ such that $E[\zeta|\xi] < \infty$, which is the physically relevant space of solutions.

Next we seek to express the energy of the dislocation ensemble directly in terms of ξ. To this end, we begin by inserting definition (2.30) into the variational problem (2.35), with the result:

$$\inf_{\zeta \in Y} \inf_{\xi \in X} E[\zeta|\xi] \tag{2.36}$$

At this point, we may invert the order of minimization in (2.36), which results in the reduced minimum problem:

$$\inf_{\xi \in X} E[\xi] \tag{2.37}$$

where

$$E[\xi] = \inf_{\zeta \in Y} \left\{ \int \frac{\mu b^2}{2d} |\zeta - \xi|^2 d^2x + \frac{1}{(2\pi)^2} \int \frac{\mu b^2}{4} K |\hat{\zeta}|^2 d^2k - \int bs\zeta d^2x \right\} \tag{2.38}$$

This minimization leads to a linear problem in ζ which may be solved analytically by an application of the Fourier transform. To this end, we apply Parseval's identity to obtain

$$E[\xi] = \inf_{\zeta \in Y} \left\{ \frac{1}{(2\pi)^2} \int \left(\frac{\mu b^2}{2d} |\hat{\zeta} - \hat{\xi}|^2 + \frac{\mu b^2}{4} K |\hat{\zeta}|^2 - b\hat{s}^* \hat{\zeta} \right) d^2k \right\} \tag{2.39}$$

Minimization with respect to ζ gives

$$\hat{\zeta} = \hat{\zeta}_0 + \frac{\hat{\xi}}{1 + Kd/2} \tag{2.40}$$

where

$$\hat{\zeta}_0 = \frac{d}{\mu b} \frac{\hat{s}}{1 + Kd/2} \tag{2.41}$$

is the slip distribution for $\xi = 0$, i.e., the slip distribution due to the elasticity of the interatomic plane. Insertion of (2.40) into (2.38) gives the sought energy:

$$E[\xi] = E_0 + \frac{1}{(2\pi)^2} \int \left(\frac{\mu b^2}{4} \frac{K}{1 + Kd/2} |\hat{\xi}|^2 - \frac{b\hat{s}\hat{\xi}}{1 + Kd/2} \right) d^2k \tag{2.42}$$

where

$$E_0 = -\frac{1}{(2\pi)^2} \int \frac{d}{2\mu} \frac{\hat{s}^2}{1 + Kd/2} d^2k \tag{2.43}$$

is independent of ξ and represents the elastic energy of the interatomic in the absence of dislocations,

i.e., at $\xi = 0$. Thus, for instance, if $s = \tau = \text{constant}$, (2.43) corresponds to an elastic energy density per unit area of $(d/2\mu)\tau^2$, which indeed coincides with the elastic energy density of the interatomic plane. Therefore, the excess energy

$$E^{\text{dis}}[\xi] = E[\xi] - E_0 \tag{2.44}$$

may be identified with the energy proper of the dislocation ensemble. By virtue of (2.42), this energy is now expressed entirely in terms of the phase field ξ. If is evident from the form of (2.42) that, in the absence of an applied field, the dislocation energy vanishes for uniform slip, as required by symmetry. Indeed, in this case $\hat{\xi} = n\delta_D(\boldsymbol{k})$, where $n \in \mathbb{Z}$ and $\delta_D(\boldsymbol{k})$ denotes the Dirac delta at $\boldsymbol{k} = \boldsymbol{0}$, and, consequently, $K\hat{\xi}$ vanishes identically in the sense of distributions.

As already noted, the phase field ξ in (2.42) takes integer values and, therefore, represents a distribution of Volterra or perfect dislocations. It is evident from the form of (2.42) that the Peierls potential has the effect of regularizing linear elasticity so as to render the energy of Volterra dislocations finite. The lattice parameter is retained in the energy functional (2.42) through the interplanar distance d. The effect of the core regularization resides in the factor

$$\hat{\varphi}_d(\boldsymbol{k}) = \frac{1}{1 + Kd/2} \tag{2.45}$$

appearing in both terms of the energy (2.42). This factor tends to suppress wavelengths on the scale of the lattice parameter or shorter. The same factor relates the integer-valued phase field ξ to the core-regularized slip distribution ζ, Eq. (2.40). In this relation, the function $\varphi_d(\boldsymbol{x})$ acts as a mollifier: the integral of $\varphi_d(\boldsymbol{x})$ over the entire plane is one, or, equivalently, $\hat{\varphi}_d(\boldsymbol{0}) = 1$; and $\varphi_d(\boldsymbol{x})$ defines a Dirac-delta sequence, i.e.,

$$\lim_{d \to 0} \varphi_d(\boldsymbol{x}) = \delta_D(\boldsymbol{x}) \tag{2.46}$$

in the sense of distributions. In real space, Eq. (2.40) takes the convolution form:

$$\zeta = \zeta_0 + \varphi_d \star \xi \tag{2.47}$$

which shows that the effect of the piecewise quadratic Peierls interplanar potential is to smooth out the phase field ξ. A consequence of this smoothing is that the perfect dislocations described

by ξ acquire a core of width commensurate with d.

It should be carefully noted that, despite the quadratic appearance of the energy functional (2.42), the attendant variational problem is strongly *nonlinear* owing to the all-important constraint that ξ be an integer-valued function. Furthermore, the minimization problem is *nonconvex* owing to the lack of convexity of the set X. This nonlinear and nonconvex structure of the variational problem is inherited from the—similarly nonlinear and nonconvex—structure of the Peierls potential (2.28). In addition, the variational problem is *nonlocal*, owing to the presence of long-range elastic interactions. These attributes render the problem (2.37) mathematically nontrivial and confer its solutions a rich structure. Despite these difficulties, the choice of a piecewise quadratic Peierls potential lends the problem analytical tractability, as demonstrated subsequently.

2.2.4 Illustrative examples

As an illustration of the type of core structure predicted by the piecewise quadratic model, we may consider the case of a general straight dislocation. For simplicity, we restrict our attention to the isotropic case. It is convenient to introduce auxiliary orthonormal axes (x_1', x_2') with x_1' normal to the dislocation line. In this coordinate frame one has

$$\hat{\xi} = \frac{2\pi\delta_D(k_2')}{ik_1'} \tag{2.48}$$

corresponding to uniform slip over the half-plane $x_1' < 0$. Here, δ_D denotes the Dirac-delta distribution, and i is the unit imaginary number. A straightforward calculation gives the slip distribution as

$$\hat{\zeta} = \frac{2\pi\delta_D(k_2')}{ik_1'(1+ck')} \tag{2.49}$$

where

$$c = \left(\sin^2\theta + \frac{\cos^2\theta}{1-\nu}\right)\frac{d}{2} \tag{2.50}$$

is a characteristic core width, and θ is the angle subtended by the normal to the dislocation line and the Burgers vector. Thus, the case $\theta = 0$ corresponds to an edge dislocation, whereas the case $\theta = \pi/2$ corresponds to a screw dislocation. A plot of the core profile is shown in Fig. 2.2. In

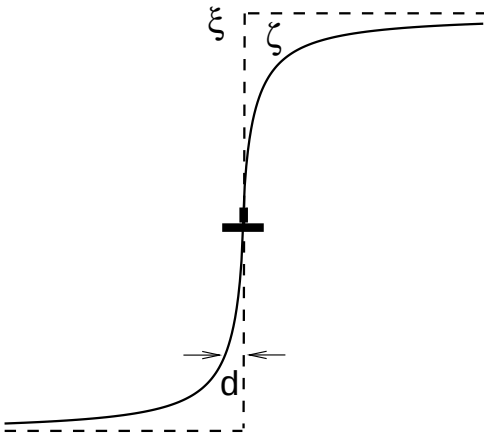

Figure 2.2: Core structure of an infinite straight dislocation predicted by the piecewise quadratic model.

addition, the energy per unit dislocation length follows in the form

$$\frac{E}{L} = \frac{\mu b^2}{4\pi}\left(\sin^2\theta + \frac{\cos^2\theta}{1-\nu}\right)\log\frac{R}{c} \tag{2.51}$$

where R is an upper cutoff radius. It is clear from this expression that c plays the role of a core cutoff radius. The width of the core depends on the orientation of the dislocation line relative to the Burgers vector, and it attains its minimum (maximum) value for edge (screw) dislocations.

This example illustrates how the introduction of a Peierls interplanar potential renders the dislocation core structure, including the core width, well defined. In particular, the high wave number divergence in the dislocation energy is eliminated. The specific core structure (2.49) is, of course, a result of the assumed piecewise quadratic form of the Peierls interplanar potential. It bears emphasis that here the interplanar potential is regarded simply as a convenient device for regularizing the equations of elasticity, and no attempt is made to model real dislocation core structures. However, it seems reasonable to expect that, for sufficiently well-spaced dislocations, the only macroscopically relevant core parameter is the core energy per unit length, and that the details of the core structure play a limited role as regards the overall energetics of the dislocation ensemble.

The Peierls potential introduces a lengthscale d into the formulation of the order of the crystal lattice parameter. The behavior of dislocation loops may therefore be expected to differ sharply according as to whether their size is much larger or, contrariwise, much smaller, than d. These regimes are exhibited in the simple example of a circular dislocation loop of radius R. In this case, ξ is the characteristic function of the circle of radius R, e.g., centered at the origin, and its Fourier transform is

$$\hat{\xi} = \int_0^R \int_0^{2\pi} \mathrm{e}^{-ikr\cos(\theta-\phi)} r dr d\theta = 2\pi \frac{R}{k} J_1(kR) \tag{2.52}$$

where J_1 is the Bessel function of the first kind, and we have written $(x_1, x_2) = (r\cos\theta, r\sin\theta)$ and $(k_1, k_2) = (k\cos\phi, k\sin\phi)$. Insertion of (2.52) into (2.42) gives

$$E = \frac{\mu b^2}{2d\pi^{3/2}} \pi R^2 G^{3,2}_{2,4}\left(\frac{4R^2}{d^2} \,\middle|\, \begin{matrix} 1/2 & 1/2 & & \\ 0 & 1/2 & 1 & -1 \end{matrix} \right) \tag{2.53}$$

where $G^{3,2}_{2,4}$ is the Meijer's G function (49), and we have set $\nu = 0$ for simplicity. From the asymptotic behavior of the Meijer function it follows that

$$E \sim \frac{\mu b^2}{d} \pi R^2, \qquad R \to 0 \tag{2.54}$$

and

$$E \sim \frac{\mu b^2}{2} R \log \frac{4R}{d}, \qquad R \to \infty \tag{2.55}$$

As expected, for fixed d the energy of the loop tends to zero as $R \to 0$. Conversely, for fixed R, the energy diverges as $d \to 0$, which corresponds to the limiting case of a perfect Volterra loop in a linear elastic crystal. Once again, this divergence illustrates the breakdown of linear elasticity in the presence of perfect dislocations and the crucial role played by the core regularization in eliminating that breakdown. The form (2.55) for the energy of large loops is consistent with expressions derived from linear elasticity (3). However, it should be noted that the core width $c = d/4$ implied by (2.55) is predicted by the present theory, which stands in contrast to the theory of linear-elastic dislocations wherein the core cutoff radius is an *adhoc* and extraneous parameter.

The issue of metastability and the existence of relative energy minimizers may be illustrated simply by the stable configurations of a dislocation dipole under the action of a resolved shear

stress τ. In order to preclude uniform slip distributions, ξ may be required to decay to zero at infinity. Suppose that slip occurs on the interval $-r/2 < x_1 < r/2$, where r is dipole width. Then, the corresponding phase field is

$$\hat{\xi} = \frac{2}{k_1} \sin \frac{k_1 r}{2} \tag{2.56}$$

For purposes of the present discussion it suffices to consider the asymptotic limit of $r \gg d$. In this regime (2.42) yields the relation

$$\frac{\partial E}{\partial r} \sim \frac{\mu b^2}{2\pi(1-\nu)} \int_0^\infty \sin k_1 r dk_1 - b\tau = \frac{\mu b^2}{2\pi(1-\nu)} \frac{1}{r} - b\tau, \quad r \to \infty \tag{2.57}$$

and

$$\frac{\partial E}{\partial c} \sim -\frac{\mu b^2}{2\pi(1-\nu)} \frac{1}{c}, \quad r \to \infty \tag{2.58}$$

From these two expressions we find

$$E \sim E_0 + \frac{\mu b^2}{2\pi(1-\nu)} \log \frac{r}{c} - b\tau r, \quad r \to \infty \tag{2.59}$$

for some constant E_0 independent of r and c. Equilibrium now demands:

$$\frac{\partial E}{\partial r} = 0 \Rightarrow \frac{\mu b^2}{2\pi(1-\nu)} \frac{1}{r} = b\tau \tag{2.60}$$

The dipole energy at equilibrium is, therefore,

$$E \sim E_0 + \frac{\mu b^2}{2\pi(1-\nu)} \left(\log \frac{r}{c} - 1 \right), \quad r \to \infty \tag{2.61}$$

where r is the solution of (2.60). The preceding analysis shows that, in the regime under consideration, there exist stable dipoles of arbitrary width r, with Eq. (2.60) supplying the resolved shear stress which equilibrates the dipole. It is evident from (2.61) that, for sufficiently large r, the dipole energy is positive and, therefore, greater than the dislocation energy corresponding to a phase field $\xi = 0$, which is zero. Hence, the dipole configuration is metastable and constitutes a relative minimum of the dislocation energy.

2.3 Energy-minimizing phase fields

The variational problem (2.37) which characterizes the stable equilibrium configurations of the slip plane may be regarded as a constrained minimization problem, in which the unknown field ξ is constrained to take integer values everywhere on the slip plane. This constraint is nonlinear and nonconvex, which renders the problem (2.37) mathematically nontrivial. In addition, the long-range elastic interactions between dislocations render the energy nonlocal. These difficulties notwithstanding, in this section we outline a strategy for characterizing a distinguished set of minimizers of the energy (2.42).

2.3.1 Constrained minimizers and energy-norm projection

A compelling characterization of the solutions of the constrained minimization problem (2.37) may be derived as follows. Let η be the unconstrained energy minimizer. Thus, η is the solution of the unconstrained minimization problem:

$$\inf_{\eta \in Y} E[\eta] \tag{2.62}$$

In particular, η is allowed to take arbitrary real values. Then, the constrained phase field is the solution of the problem (e.g., (50)):

$$\inf_{\xi \in X} \frac{1}{2} \parallel \xi - \eta \parallel^2 \tag{2.63}$$

where

$$\parallel u \parallel = \sqrt{\langle u, u \rangle} \tag{2.64}$$

is an energy norm corresponding to the inner product

$$\langle u, v \rangle = \frac{1}{(2\pi)^2} \int \frac{\mu b^2}{2} \frac{K}{1 + Kd/2} \, \hat{u}^* \, \hat{v} \, d^2k \tag{2.65}$$

The solution of (2.63) may be expressed as

$$\xi = P_X \eta \tag{2.66}$$

where P_X denotes the closest-point projection of Y onto X in the sense of norm (2.64).

The solution procedure leading to the core-regularized slip distribution ζ may now be broken

down into three steps. The first step consists of the solution of the unconstrained minimization problem (2.62), resulting in the real-valued unconstrained minimizer η. The second step consists of the solution of the constrained minimization problem (2.63), resulting in the projection of η onto its closest integer-valued phase-field ξ. The third step consists of the smoothing of ξ according to (2.40), leading to the introduction of smooth cores around all dislocation lines.

The exact evaluation of the projection (2.63) entails some difficulty. The corresponding stationarity condition consists of the requirement that the functional be stable with respect to a unit increment or decrement of ξ over an arbitrary region of the slip plane. Thus, if $R \subset \mathbb{R}^2$ is one such region and χ_R denotes its characteristic function, stationarity demands that the inequalities

$$\| \xi + \chi_R - \eta \|^2 \geq \| \xi - \eta \|^2 \tag{2.67}$$

$$\| \xi - \chi_R - \eta \|^2 \geq \| \xi - \eta \|^2 \tag{2.68}$$

be simultaneously satisfied. After some straightforward manipulations, (2.67-2.68) may be recast in the form

$$\frac{1}{2} \| \chi_R \|^2 \geq \langle \xi - \eta, \chi_R \rangle \geq -\frac{1}{2} \| \chi_R \|^2 \tag{2.69}$$

These inequalities set bounds on the possible values of the resultant of the residual tractions acting over arbitrary regions of the slip plane. In order to verify the bounds (2.69), we choose circles of radius $\epsilon \to 0$ as the test regions R. Let B_ϵ denote the circle of radius ϵ centered at the origin, and set

$$\chi_R(\boldsymbol{y}) = \chi_{B_\epsilon}(\boldsymbol{y} - \boldsymbol{x}) \tag{2.70}$$

where $\boldsymbol{x}$ ranges over all of $\mathbb{R}^2$. For this choice of test function we have

$$\langle \xi - \eta, \chi_{B_\epsilon} \rangle = \frac{1}{(2\pi)^2} \int \frac{\mu b^2}{2} \frac{K}{1 + Kd/2} (\hat{\xi}(\boldsymbol{k}) - \hat{\eta}(\boldsymbol{k})) e^{i\boldsymbol{k}\cdot\boldsymbol{x}} \hat{\chi}^*_{B_\epsilon} d^2k \tag{2.71}$$

But, by virtue of the identity

$$\frac{K}{1 + Kd/2} (\hat{\xi}(\boldsymbol{k}) - \hat{\eta}(\boldsymbol{k})) = \hat{\xi}(\boldsymbol{k}) - \hat{\zeta}(\boldsymbol{k}) \tag{2.72}$$

which follows from (2.40) and (2.65), Eq. (2.71) reduces to

$$\langle \xi - \eta, \chi_{B_\epsilon} \rangle = \frac{1}{(2\pi)^2} \int \frac{\mu b^2}{d} (\hat{\xi}(\boldsymbol{k}) - \hat{\zeta}(\boldsymbol{k})) e^{i\boldsymbol{k}\cdot\boldsymbol{x}} \hat{\chi}^*_{B_\epsilon} d^2k \tag{2.73}$$

In addition, distribuitionally as $\epsilon \to 0$ we have $\chi_{B_\epsilon} \sim \pi\epsilon^2 \delta_D$, and (2.73) simplifies to

$$\langle \xi - \eta, \chi_{B_\epsilon} \rangle = \frac{1}{(2\pi)^2} \int \frac{\mu b^2}{d} (\hat{\xi}(\boldsymbol{k}) - \hat{\zeta}(\boldsymbol{k})) e^{i\boldsymbol{k}\cdot\boldsymbol{x}} \pi\epsilon^2 d^2k \tag{2.74}$$

or evaluation of the inverse Fourier transform

$$\langle \xi - \eta, \chi_{B_\epsilon} \rangle = \frac{\mu b^2}{d} \pi\epsilon^2 (\xi(\boldsymbol{k}) - \zeta(\boldsymbol{k})) \tag{2.75}$$

On the other hand, we have from (2.54) that

$$\| \xi_{B_\epsilon} \|^2 \sim \frac{\mu b^2}{d} \pi\epsilon^2 \tag{2.76}$$

Inserting (2.75) and (2.76) into (2.69) finally gives the stationary condition

$$\frac{1}{2} \geq \xi(\boldsymbol{x}) - \zeta(\boldsymbol{x}) \geq -\frac{1}{2} \tag{2.77}$$

whose unique solution is

$$\xi(\boldsymbol{x}) = P_{\mathbb{Z}} \zeta(\boldsymbol{x}) \tag{2.78}$$

where $P_{\mathbb{Z}}$ denotes the closest-point projection of $\mathbb{R}$ onto $\mathbb{Z}$. Thus, Eq.(2.78) states that, pointwise almost everywhere in $\mathbb{R}^2$, $\xi(\boldsymbol{x})$ is the closest integer to $\zeta(\boldsymbol{x})$.

The stationary condition (2.77) may be expressed in terms of the fields ξ and η by taking the inverse Fourier transform of the identity (2.72) and using definition (2.45), with the result

$$\frac{1}{2} \geq ((\delta_D - \varphi_d) \star (\xi - \eta))(\boldsymbol{x}) \geq -\frac{1}{2} \tag{2.79}$$

This condition is now nonlocal and, consequently, cumbersome to enforce. However, in case in which η varies smoothly on the scale of d, the individual dislocations are well separated on that scale and their cores do not overlap appreciably. Consider then the result $\xi' = P_{\mathbb{Z}}\eta$ of applying an integer projection pointwise directly to the field η. The difference $\xi' - \eta$ then lies in the interval

$[-1/2, 1/2]$ by construction. Because the cores are well separated, they may be expected to be ostensibly symmetric and, in particular, $\varphi_d \star (\xi' - \eta) \sim 0$ at he dislocation lines. Under these conditions, we may expect that

$$\frac{1}{2} \geq \xi'(\boldsymbol{x}) - \eta(\boldsymbol{x})\varphi_d \star (\xi - \eta)(\boldsymbol{x}) \geq -\frac{1}{2} \tag{2.80}$$

which suggests that the stationary condition (2.80) is approximately satisfied with:

$$\xi(\boldsymbol{x}) = P_{\mathbb{Z}}\eta \tag{2.81}$$

i.e., by taking ξ to be the closest integer to η pointwise. On the strength of this heuristic argument, in the numerical results presented in Section 2.5 we shall identify the level contours of the field η with the dislocation lines.

2.3.2 Unconstrained equilibrium equations

Next we turn to the unconstrained minimization problem (2.62). The corresponding Euler-Lagrange equation is

$$\frac{\mu b^2}{2} K\hat{\eta} = b\hat{s} \tag{2.82}$$

It is clear from this equation that all functions of the form $\hat{\eta} \propto \delta_D$, corresponding to uniform slip distributions over the entire slip plane, are solutions of the homogeneous equation. Therefore, it follows from the Fredholm alternative theorem that a necessary condition for (2.82) to have solutions is that $\hat{s}(\boldsymbol{0}) = 0$, i.e.,

$$\int s(\boldsymbol{x}) d^2x = 0 \tag{2.83}$$

This condition expresses the requirement that the resultant of the resolved shear-stress field be zero. If this condition is met, then $\hat{\eta}$ follows from (2.82) as

$$\hat{\eta} = \frac{2}{Kb}\frac{\hat{s}}{\mu} + 2\pi C\delta_D \tag{2.84}$$

where C is an arbitrary constant. An application of the inverse Fourier transform to this expression gives

$$\eta = G \star s + C \tag{2.85}$$

where the fundamental solution

$$G(\boldsymbol{x}) = \frac{1}{(2\pi)^2} \int \frac{2}{\mu b} \frac{1}{K} \mathrm{e}^{i\boldsymbol{k}\cdot\boldsymbol{x}} d^2k = \frac{1}{\mu\pi b} \frac{\sqrt{x_1^2 + x_2^2}}{x_1^2 + x_2^2/(1-\nu)} \tag{2.86}$$

represents an unconstrained slip distribution which decays to zero at infinity and is in equilibrium with a resolved shear stress in the form of a Dirac delta applied at the origin.

2.3.3 The general solution

We proceed to collect all the solution steps outlined in the foregoing and to provide an explicit expression for the slip distribution ζ as a function of the applied field s. Thus, the solution ζ follows in three steps, namely: $s \to \eta \to \xi \to \zeta$. The first step yields the unconstrained phase field η, the second the integer-valued phase field ξ, and the third step returns the core-regularized slip distribution ζ. Gathering the relations (2.85), (2.66) and (2.40) corresponding to each of the three steps just enunciated gives, explicitly,

$$\zeta = \varphi_d \star P_X(G \star s) + C \tag{2.87}$$

where the projection P_X is given by (2.81) and, as noted earlier, we require s to have zero mean, whereupon the solution is determined up to an arbitrary integer $C \in \mathbb{Z}$.

At this point, it is illuminating to revisit the question of uniqueness and metastability, especially in view of the existence of relative energy minimizers such as presented in Section 2.2.4. In this respect, it should be noted that the solution procedure presented in the foregoing returns a *unique solution*, modulo uniform slips. Indeed, the unconstrained equilibrium equations are linear and, within the constraints imposed by the Fredholm alternative, determine a *unique* unconstrained slip distribution η. The local truncation (2.81) in turn yields a *unique* integer-valued phase field ξ. Finally, smoothing as in (2.47) results in a *unique* core-regularized phase field ζ. It is therefore clear that the solution procedure outlined above selects a 'preferred' slip distribution among a

vast array of competitors. Thus, for instance, in regions of the slip plane where the dislocation density is small, i.e., where the distance between neighboring dislocations is large compared to the core size d, metastable slip distributions may be obtained by inserting small loops in equilibrium with the local resolved shear stress within the intervening area between dislocations. Examples of metastable solutions of this type have been discussed in Section 2.2.4. It is intriguing that, in those examples, e.g., in the case of a plane slipping under the action of a uniform resolved shear stress, the unique preferred solution $\zeta = 0$ delivers the minimum attainable energy, i.e., it is an absolute energy minimizer. An open mathematical question of some interest is whether the preferred solution (2.87) does indeed always deliver an absolute energy minimizer.

2.3.4 Averages and macroscopic variables

Many of the macroscopic quantities of interest pertaining to the behavior of a slip plane may be recovered by taking the appropriate averages. In order to render the operation of taking averages over the slip plane well defined, we may simply assume that the phase field is periodic with unit cell Ω, i.e.,

$$\zeta(\boldsymbol{x}) = \zeta(\boldsymbol{x} + l^1\boldsymbol{a}_1 + l^2\boldsymbol{a}_2), \quad (l^1, l^2) \in \mathbb{Z}^2 \tag{2.88}$$

for some basis vectors $\{\boldsymbol{a}_1, \boldsymbol{a}_2\}$. Under these conditions, an application of Orowan's relation gives the macroscopic slip strain as

$$\gamma = \frac{\gamma_0}{|\Omega|}\int_\Omega \zeta d^2x = \gamma_0\langle\zeta\rangle \tag{2.89}$$

or, in view of (2.40), alternatively as

$$\gamma = \frac{\gamma_0}{|\Omega|}\int_\Omega \xi d^2x = \gamma_0\langle\xi\rangle \tag{2.90}$$

where

$$\gamma_0 = \frac{b}{l} \tag{2.91}$$

is a reference slip strain. Here l is the slip-plane spacing, which is assumed known, and γ_0 is the slip strain which is attained when one loop sweeps over the entire slip plane. The dislocation line

density per unit volume is related to the phase field as

$$\rho = \frac{1}{l}\langle|\nabla\xi|\rangle \tag{2.92}$$

Indeed, the integral of $|\nabla\xi|$ over a region of the slip plane simply measures the total length of all dislocation lines contained in that region. Finally, the global equilibrium condition (2.83) may equivalently be expressed in the form:

$$\langle s\rangle = 0 \tag{2.93}$$

which requires that the mean resolved shear stress be zero.

2.4 Irreversible processes and kinetics

The preceding developments have focused on the energetics of a dislocation ensemble in an elastic crystal endowed with a piecewise quadratic Peierls interplanar potential. In addition to this energetics, the dislocation ensemble may undergo inelastic interactions with the lattice, resulting in lattice friction; and short-range inelastic interactions with an assortment of obstacles, such as second-phase particles, forest dislocations, and others. We assume that these interactions are *irreversible* and, therefore, kinetic in nature. The essential assumption is that the crossing of an obstacle by a dislocation 'costs' a certain energy, regardless of the direction of crossing. The energy toll depends on the strength of the interaction and is dissipated, e. g., as heat, and irreversibly lost to the system.

2.4.1 Variational formulation

The irreversible dislocation-obstacle interactions may be built into the variational framework developed previously by recourse to time discretization (24; 23; 25; 26; 27). Thus, henceforth we consider a sequence of discrete times t_0, t_1, ..., t_n, t_{n+1}, ..., presume the slip distribution ζ_0 at time t_0 to be known, and seek to compute the slip distributions ζ^1, ..., ζ^n, ζ^{n+1}, ..., at all subsequent times. The central problem is to determine the slip distribution ζ^{n+1} at time t_{n+1} given the solution ζ^n at time t_n and the applied field s_{n+1} at time t_{n+1}. To this end, following (24; 23; 25; 26; 27) we

introduce the incremental work function:

$$W[\zeta^{n+1}|\zeta^n] = E[\zeta^{n+1}] - E[\zeta^n] + \int f(\boldsymbol{x})|\zeta^{n+1}(\boldsymbol{x}) - \zeta^n(\boldsymbol{x})|d^2x \tag{2.94}$$

where the elastic energy $E[\zeta]$ is given by (2.30), and the second term represents the incremental work of dissipation. In this term, the field $f(\boldsymbol{x}) \geq 0$ represents the energy cost per unit area associated with the passage of one dislocation over the point $\boldsymbol{x}$, i. e., with a transition of the form $\zeta(\boldsymbol{x}) \to \zeta(\boldsymbol{x}) \pm 1$. Thus, the field $f(\boldsymbol{x})$ represents the distribution of obstacles over the slip plane and is assumed known. By the work and energy identity, it follows that W equals the total work supplied to the system during the interval $[t_n, t_{n+1}]$. Eq. (2.94) simply states that part of this work is invested in raising the energy of the crystal, whereas the remainder of the external work supplied is invested in overcoming the obstacle resistance. The updated slip distribution now follows from the minimum principle:

$$\inf_{\zeta^{n+1} \in Y} W[\zeta^{n+1}|\zeta^n] \tag{2.95}$$

It should be carefully noted that the work function (2.94) depends on the initial conditions ζ^n for the time step, which allows for irreversibility and hysteresis.

2.4.2 Min-max formulation

In order to enable the application of the general solution procedure outlined in the foregoing, we proceed to rephrase problem (2.95) as a min-max problem (e. g., (51), § 36)]. We begin by noting the identity:

$$|x| = \max_{\Lambda \in [-1,1]} \Lambda x, \quad \forall x \in \mathbb{R} \tag{2.96}$$

Since $f(\boldsymbol{x}) \geq 0$, it follows from this identity that

$$\int f(\boldsymbol{x})|\zeta^{n+1}(\boldsymbol{x}) - \zeta^n(\boldsymbol{x})|d^2x = \sup_{|g^{n+1}| \leq f} \int g^{n+1}(\boldsymbol{x})\big(\zeta^{n+1}(\boldsymbol{x}) - \zeta^n(\boldsymbol{x})\big)d^2x \tag{2.97}$$

which may be viewed as a statement of the principle of maximum dissipation. The field $g^{n+1}(\boldsymbol{x})$, which is required to lie within the bounds $\pm f(\boldsymbol{x})$, may be regarded as the reaction-force field exerted by the obstacles on the dislocation ensemble at time t_{n+1}. Inserting representation (2.97) into (2.95) and using standard properties of saddle points of concave-convex functions (e. g., (51),

Theorem 36.3)] leads to the problem

$$\sup_{|g^{n+1}|\leq f} \inf_{\zeta^{n+1}\in Y} \left\{ E[\zeta^{n+1}] - E[\zeta^n] + \int g^{n+1}(\boldsymbol{x})\big(\zeta^{n+1}(\boldsymbol{x}) - \zeta^n(\boldsymbol{x})\big)d^2x \right\} \tag{2.98}$$

For fixed $g^{n+1}(\boldsymbol{x})$ the central minimization problem stated in (2.98) is now of the form (2.35) analyzed earlier, and the solution is given by (2.87). The problem which then remains is to optimize the field $g^{n+1}(\boldsymbol{x})$ in order to maximize the dissipation at the obstacles.

The optimization of $g^{n+1}(\boldsymbol{x})$ may conveniently be reduced to a problem with linear constraints by the introduction of Lagrange multipliers (e. g., (51), § 28)], which leads to the Lagrangian:

$$\begin{aligned} L[g^{n+1}, \lambda^{\pm}] = \inf_{\zeta^{n+1}\in Y} &\left\{ E[\zeta^{n+1}] - E[\zeta^n] + \int g^{n+1}(\boldsymbol{x})\big(\zeta^{n+1}(\boldsymbol{x}) - \zeta^n(\boldsymbol{x})\big)d^2x \right\} \\ &+ \int \lambda^+(\boldsymbol{x})\big(g^{n+1}(\boldsymbol{x}) - f(\boldsymbol{x})\big)d^2x - \lambda^-(\boldsymbol{x})\big(g^{n+1}(\boldsymbol{x}) + f(\boldsymbol{x})\big)d^2x \end{aligned} \tag{2.99}$$

The corresponding Kuhn-Tucker optimality conditions are (e. g., (51), Theorem 28.3)]:

$$\zeta^{n+1}(\boldsymbol{x}) - \zeta^n(\boldsymbol{x}) = \lambda^+(\boldsymbol{x}) - \lambda^-(\boldsymbol{x}) \tag{2.100}$$

$$g^{n+1}(\boldsymbol{x}) - f(\boldsymbol{x}) \leq 0, \quad -g^{n+1}(\boldsymbol{x}) - f(\boldsymbol{x}) \leq 0 \tag{2.101}$$

$$\lambda^+(\boldsymbol{x}) \geq 0, \quad \lambda^-(\boldsymbol{x}) \geq 0 \tag{2.102}$$

$$\big(g^{n+1}(\boldsymbol{x}) - f(\boldsymbol{x})\big)\lambda^+(\boldsymbol{x}) = 0, \quad \big(g^{n+1}(\boldsymbol{x}) + f(\boldsymbol{x})\big)\lambda^-(\boldsymbol{x}) = 0 \tag{2.103}$$

which must be satisfied simultaneously by the solution. In (2.100), the updated slip distribution ζ^{n+1} follows from the general solution (2.87) as

$$\zeta^{n+1} = \varphi_d \star P_X\big(G \star (s_{n+1} - g^{n+1}/b)\big) + C_{n+1} \tag{2.104}$$

and the global equilibrium condition (2.83) now becomes

$$\int b\, s_{n+1}(\boldsymbol{x})d^2x = \int g^{n+1}(\boldsymbol{x})d^2x \tag{2.105}$$

which requires that the total applied force be exactly equilibrated by the resultant of the obstacle reactions.

It is interesting to note how the optimality conditions (2.100-2.103) give mathematical expression to the assumed frictional interaction between the phase and obstacle fields, including *stick-slip* behavior. Thus, the equalities (2.103) prevent $\lambda^+(\boldsymbol{x})$ and $\lambda^-(\boldsymbol{x})$ from being nonzero simultaneously. If, for instance, $\zeta^{n+1}(\boldsymbol{x}) - \zeta^n(\boldsymbol{x}) > 0$, then by virtue of (2.102) and (2.100) it necessarily follows that $\lambda^-(\boldsymbol{x}) = 0$ and $\lambda^+(\boldsymbol{x}) > 0$, and, by the first of (2.103), $g^{n+1}(\boldsymbol{x}) = f(\boldsymbol{x})$. Conversely, if $\zeta^{n+1}(\boldsymbol{x}) - \zeta^n(\boldsymbol{x}) < 0$, then (2.102) and (2.100) require that $\lambda^-(\boldsymbol{x}) > 0$ and $\lambda^+(\boldsymbol{x}) = 0$, and, by the second of (2.103), $g^{n+1}(\boldsymbol{x}) = -f(\boldsymbol{x})$. These two cases correspond to *slip* conditions at $\boldsymbol{x}$, or yielding. If the conditions (2.101) are satisfied as strict inequalities, then it follows from (2.101) that, necessarily, $\lambda^+(\boldsymbol{x}) = 0$ and $\lambda^-(\boldsymbol{x}) = 0$, which, in view of (2.100), requires that $\zeta^{n+1}(\boldsymbol{x}) - \zeta^n(\boldsymbol{x}) = 0$. This case corresponds to *stick* conditions, or elastic unloading. The theory is thus capable of describing the loading-unloading irreversibility characteristic of plastic materials.

2.4.3 Special case of short-range obstacles

Next we consider the special case of an obstacle field consisting of a uniform Peierls stress and a distribution of short-range obstacles. This case merits special attention owing to the fact that the problem can conveniently be reduced to the determination of the phase field at the obstacles, which greatly facilitates calculations.

For definiteness, we shall assume the resolved shear-stress field to be of the form

$$s(\boldsymbol{x}, t) = \tau(t) + s_0(\boldsymbol{x}) \tag{2.106}$$

where $\tau(t)$ is the applied resolved shear stress at time t and $s_0(\boldsymbol{x})$ is a self-equilibrated field representing the long-range elastic stresses induced by the obstacles. For instance, in calculations of forest hardening $s_0(\boldsymbol{x})$ may describe the action on the slip plane of the long-range stress field of the forest dislocations. In this case, in the vicinity of a secondary dislocation $s_0(\boldsymbol{x})$ tends asymptotically to the field of the osculating straight dislocation, and, therefore, has the form

$$s_0 \sim b\mu \frac{A(\theta)}{r}, \qquad r \to 0 \tag{2.107}$$

for some function $A(\theta)$ which depends on the geometry of the secondary dislocation. Here (r, θ) are polar coordinates centered at the secondary dislocation. The corresponding unconstrained phase

field η_0 diverges logarithmically, i. e.,

$$\eta_0 \sim B(\theta) \log r, \qquad r \to 0 \tag{2.108}$$

for some function $B(\theta)$. The attendant phase field ξ_0 represents an infinite pileup of perfect dislocation loops encircling the secondary dislocation. The depth of this pileup is truncated and rendered finite when the core of the secondary dislocations is taken into account. Since the exact geometry of the secondary dislocations away from the primary slip plane is unknown within the present formulation, one possibility that immediately suggests itself is to model s_0 as a random field. The use of random fields to model barriers to dislocation slip, or other similar processes such as first-order phase transitions in magnetic systems, has been proposed by Hardikar *et al.* (52) and Sethna (53).

For simplicity, we shall additionally assume that the obstacle distribution and, correspondingly, the phase field, is periodic with unit cell Ω. For the obstacle system under consideration, the obstacle-strength field may be taken to be of the form:

$$f(\boldsymbol{x}) = b\tau^P + \sum_{i=1}^{N} f_i \, \psi_d(\boldsymbol{x} - \boldsymbol{x}_i), \quad \boldsymbol{x} \in \Omega \tag{2.109}$$

where $\tau^P \geq 0$ is the Peierls stress, x_i and $f_i \geq 0$, $i = 1, \ldots, N$, are the positions and strengths of the obstacles in Ω, respectively, and the function $\psi_d(\boldsymbol{x})$ represents the structure of the obstacles. As noted earlier, the detailed modeling of the structure of obstacles is beyond the scope of the present work. However, the treatment of short-range obstacles as points, corresponding to setting $\psi_d = \delta_D$ in (2.109), inevitably leads to logarithmic divergences of the phase field under the obstacles. In order to avoid these divergences the obstacles must be endowed with a finite core. Conveniently, however, for distributions of well-separated short-range obstacles the precise form of ψ_d plays a role only in the immediate vicinity of the obstacles and is otherwise largely irrelevant. We shall simply require that the overlap function $\psi_d \star \varphi_d$ define a Dirac-delta sequence as $d \to 0$, i. e., that

$$\lim_{d \to 0} (\psi_d \star \varphi_d)(\boldsymbol{x}) = \delta_D(\boldsymbol{x}) \tag{2.110}$$

in the sense of distributions. Thus, for points such that $|\boldsymbol{x} - \boldsymbol{x}_i| \gg d$ the overlap function $\psi_d \star \varphi_d$ may be treated as a Dirac-delta. In addition, in order to avoid divergent integrals we shall require that

the product $\hat{\psi}_d(\boldsymbol{k})\hat{\varphi}_d(\boldsymbol{k})$ decay as $1/k^2$ as $k \to \infty$. For forest obstacles, a simple choice consistent with these requirements is

$$\psi_d(\boldsymbol{x}) = \varphi_d(\boldsymbol{x}) \tag{2.111}$$

which simply states that the core structure of the forest obstacles is identical to the core structure of the primary dislocations.

The problem to be solved now follows by inserting (2.109) into the Lagrangian (2.99). In order to facilitate the solution of this problem we make the *ansatz* that the obstacle reaction field is of the form:

$$g^{n+1}(\boldsymbol{x}) = g_0^{n+1} + \sum_{i=1}^{N} g_i^{n+1}\, \psi_d(\boldsymbol{x} - \boldsymbol{x}_i), \quad \boldsymbol{x} \in \Omega \tag{2.112}$$

where g_i^{n+1}, $i = 0, 1, \ldots, N$, are constants. This *ansatz* may be verified *a posteriori* by checking that all optimality conditions (2.100 - 2.103) are satisfied. Inserting (2.112) into (2.99) and making use of identities (2.40), (2.90) and (2.110) yields the reduced Lagrangian:

$$\begin{aligned} L[\boldsymbol{g}^{n+1}, \boldsymbol{\lambda}^{\pm}] = \inf_{\xi^{n+1} \in X} \left\{ E[\xi^{n+1}] - E[\xi^n] + |\Omega|\, g_0^{n+1}(\gamma_{n+1} - \gamma_n) + \sum_{i=1}^{N} g_i^{n+1}\big(\xi_i^{n+1} - \xi_i^n\big) \right\} \\ + |\Omega| \left\{ \lambda_0^+ (g_0^{n+1} - b\,\tau^P) - \lambda_0^- (g_0^{n+1} + b\,\tau^P) \right\} + \sum_{i=1}^{N} \lambda_i^+ (g_i^{n+1} - f_i) - \sum_{i=1}^{N} \lambda_i^- (g_i^{n+1} + f_i) \end{aligned} \tag{2.113}$$

where the energy functional $E[\xi]$ is given by (2.42). The Kuhn-Tucker optimality conditions (2.100-2.103) now reduce to:

$$\gamma^{n+1} - \gamma^n = \lambda_0^+ - \lambda_0^- \tag{2.114}$$

$$g_0^{n+1} - b\tau^P \leq 0, \quad -g_0^{n+1} - b\tau^P \leq 0 \tag{2.115}$$

$$\lambda_0^+ \geq 0, \quad \lambda_0^- \geq 0 \tag{2.116}$$

$$(g_0^{n+1} - b\tau^P)\lambda_0^+ = 0, \quad (g_0^{n+1} + b\tau^P)\lambda_0^- = 0 \tag{2.117}$$

and

$$\xi_i^{n+1} - \xi_i^n = \lambda_i^+ - \lambda_i^- \tag{2.118}$$

$$g_i^{n+1} - f_i \leq 0, \quad -g_i^{n+1} - f_i \leq 0 \tag{2.119}$$

$$\lambda_i^+ \geq 0, \quad \lambda_i^- \geq 0 \tag{2.120}$$

$$(g_i^{n+1} - f_i)\lambda_i^+ = 0, \quad (g_i^{n+1} + f_i)\lambda_i^- = 0 \tag{2.121}$$

with $i = 1, \ldots, N$.

If $\gamma_{n+1} \neq \gamma_n$, i. e., in the presence of macroscopic slip, Eqs. (2.114 - 2.117) simply require that

$$g_0^{n+1} = b\,\tau^P sgn(\gamma_{n+1} - \gamma_n) \tag{2.122}$$

where $sgn(x) = x/|x|$ is the *signum* function. In addition, if $|g_0^{n+1}| < b\,\tau^P$, then it necessarily follows from (2.114-2.117) that $\gamma_{n+1} = \gamma_n$, corresponding to elastic unloading. Thus, the Peierls stress has the effect of introducing an initial threshold, or yield point, for plastic activity.

In evaluating the optimality conditions (2.118 - 2.121), the phase field at the obstacles is computed as

$$\xi_i^{n+1} = P_{\mathbb{Z}}\eta_i^{n+1} \tag{2.123}$$

which is a special case of the pointwise projection (2.81). In addition, the unconstrained phase field follows by inserting (2.112) into (2.85) and taking periodicity into account, with the result

$$\eta^{n+1}(\boldsymbol{x}) = -\sum_{i=1}^{N} g_i^{n+1} \left\{ \int \left[\sum_{(l^1,l^2)\in\mathbb{Z}^2} G(\boldsymbol{x} - \boldsymbol{x}' + l^1\boldsymbol{a}_1 + l^2\boldsymbol{a}_2) \right] (\varphi_d \star \psi_d)(\boldsymbol{x}' - \boldsymbol{x}_i) d^2x' \right\} + C_{n+1} \tag{2.124}$$

Specializing this expression at obstacle sites we obtain the linear system of equations

$$\eta_i^{n+1} = -\sum_{j=1}^{N} G_{ij} g_j^{n+1} + C_{n+1}, \quad i = 1, \ldots, N \tag{2.125}$$

which directly relates the unconstrained phase field at the obstacles and the obstacle reactions. In

addition, the global equilibrium condition (2.105) further reduces to

$$b\, s_{n+1} = g_0^{n+1} + \frac{1}{|\Omega|} \sum_{i=1}^{N} g_i^{n+1} \tag{2.126}$$

where we have made use of the identity $\langle s_0 \rangle = 0$. Eq. (2.126) simply states that the applied resolved shear stress must be exactly equilibrated by lattice friction and the resultant of all obstacle reactions.

In view of (2.110), the influence coefficients coupling pairs of distinct obstacles in (2.125) may be computed as

$$G_{ij} \sim \sum_{(l^1,l^2)\in\mathbb{Z}^2} G(\boldsymbol{x}_i - \boldsymbol{x}_j + l^1\boldsymbol{a}_1 + l^2\boldsymbol{a}_2), \quad i \neq j \tag{2.127}$$

In arriving at this expression we have made use of the assumption that the short-range obstacles are well separated, so that they effectively interact as point obstacles. The evaluation of the self-interaction coefficients G_{ii} in (2.127) requires some care, as the obstacles can no longer be treated as points and their assumed structure must be taking into consideration. In this case we have

$$G_{ii} \sim \int G(\boldsymbol{x})(\varphi_d \star \psi_d)(\boldsymbol{x}) d^2x + \sum_{(l^1,l^2)\in\mathbb{Z}^2-\mathbf{0}} G(l^1\boldsymbol{a}_1 + l^2\boldsymbol{a}_2) \qquad \text{(no sum in } i\text{)} \tag{2.128}$$

where the introduction of the function ψ_d describing the obstacle core is essential in order to avoid a divergent value of G_{ii}. If, by way of example, we choose the obstacle structure (2.111), then a straightforward calculation gives

$$\int G(\boldsymbol{x})(\varphi_d \star \varphi_d)(\boldsymbol{x}) d^2x = \frac{(2-\nu)\sqrt{1-\nu}}{2\pi^2 b} \frac{1}{\mu\, d} \tag{2.129}$$

In general, this constant is well defined and scales as $1/bd$ provided that, as previously assumed, the product $\hat{\psi}_d(\boldsymbol{k})\hat{\varphi}_d(\boldsymbol{k})$ decays as $1/k^2$ as $k \to \infty$. It bears emphasis that the sole influence of the choice of obstacle structure function ψ_d on the entire model resides in the constant (2.129). Thus, difference choices of ψ_d result in different values of the constant, but do not otherwise affect the remainder of the model.

2.4.4 Algorithmic implementation

The preceding relations provide a complete basis for updating the phase field incrementally. The precise algorithm employed in the calculations reported subsequently proceeds as follows:

1. *Assembly and factorization.* The calculations are started by computing the matrix G_{ij} using formulae (2.127), (2.128) and (2.129). This matrix is symmetric and positive-definite and has dimension $N \times N$. The matrix G_{ij} is then factorized. It should be noted that, for a constant distribution of obstacles, the matrix G_{ij} remains constant throughout the entire deformation process and its factorization may be performed once and for all at the start of the calculations.

2. *Initialization.* At time t_0, the constant C_0 in (2.125) is set to zero. In addition, the unconstrained phase field η_0 induced by the residual tractions s_0 is set up by superposition of fields of the form (2.108), suitably truncated at the origin so as to account for the obstacle core. The sign of the superposed fields is alternated randomly in such a way that the mean value of s_0 is zero, as required.

3. *Incremental update.* Assume that the state of the slip plane is completely known at time t_n, and that a new value C_{n+1} of the constant in (2.125) is prescribed at time t_{n+1}. Thus, the constant C is chosen as a convenient control or loading parameter. The state of the slip plane is updated by means of the following operations:

   (a) *Stick predictor.* Set the predictor unconstrained phase field $\tilde{\eta}_i^{n+1} = \eta_i^n$, and compute the predictor reactions:

   $$\tilde{g}_j^{n+1} = \sum_{i=1}^{N} G_{ji}^{-1}(C_{n+1} - \tilde{\eta}_i^{n+1}) \tag{2.130}$$

   (b) *Reaction projection.* Project $\tilde{g}_j^{n+1}$ onto the closest point of the admissible set: $|g_i| \leq f_i$, $i = 1, \ldots, N$, according to

   $$g_i^{n+1} = \begin{cases} f_i, \text{ if } \tilde{g}_i^{n+1} > f_i \\ \tilde{g}_i^{n+1}, \text{ if } |\tilde{g}_i^{n+1}| \leq f_i \\ -f_i, \text{ if } \tilde{g}_i^{n+1} < -f_i \end{cases} \tag{2.131}$$

4. *Phase-field evaluation.* Once the obstacle reactions g_i^{n+1} are known, the unconstrained phase field $\eta_{n+1}(\boldsymbol{x})$ may be computed from (2.124). At the obstacles, the unconstrained phase field follows directly as

$$\eta_i^{n+1} = \sum_{j=1}^{N} G_{ij} g_j^{n+1} + C_{n+1} \tag{2.132}$$

For $\boldsymbol{x}$ sufficiently distant from all obstacles, we may treat the obstacles as points, whereupon (2.124) simplifies to

$$\eta_{n+1}(\boldsymbol{x}) = -\sum_{i=1}^{N} \left[\sum_{(l^1,l^2)\in\mathbb{Z}^2} G(\boldsymbol{x} - \boldsymbol{x}_i + l^1\boldsymbol{a}_1 + l^2\boldsymbol{a}_2) \right] g_i^{n+1} + C_{n+1} \tag{2.133}$$

Finally, the local projection (2.81) returns the phase field $\xi_{n+1}(\boldsymbol{x})$, and (2.47) gives the core-regularized phase field $\zeta_{n+1}(\boldsymbol{x})$.

5. *Macroscopic variables.* Finally, the macroscopic resolved shear stress τ_{n+1} and slip strain γ_{n+1} may be computed from (2.126) and (2.90), respectively.

2.5 Application to the forest hardening mechanism

In this section, we apply the general framework developed in the foregoing to the forest hardening mechanism. To this end, we consider a slip plane traversed at random locations by fixed secondary or forest dislocations and acted upon by an applied resolved shear stress. The objective is to characterize the dislocation patterns which arise in response to the applied loading, and to determine the effective behavior of the system measured, e.g., in terms of the macroscopic slip strain and dislocation line density. In situations where the forest hardening mechanism is dominant, the kinetics of the primary dislocation ensemble is primarily governed by the interaction between the dislocations and the applied resolved shear stress; the long-range elastic interactions between the primary dislocations; the line-tension effect resulting from the core structure of the dislocations; the interaction between the primary dislocations and the long-range elastic stress field of the forest dislocations; and the short-range interactions between primary and forest dislocations such as may result in jogs, the formation of junctions, and other reaction products. Thus, the forest hardening mechanism provides a convenient framework for illustrating the range of behaviors predicted by

the theory.

2.5.1 Monotonic loading

We begin by considering the base case of a single slip system containing a fixed concentration of point obstacles of uniform strength and deforming under the action of a monotonically increasing shear stress. We assume a periodicity, and the unit cell Ω is taken to be a square of dimension $100b$. We randomly select 100 points within the periodic cell as the obstacle sites. To these obstacles we assign a uniform strengths $f = 10\mu b^2$. For simplicity, we take the Peierls stress $\tau^P = 0$, and set Poisson's ratio $\nu = 0.3$.

Fig. 2.3 shows the computed stress-strain curve and dislocation density as functions of the macroscopic slip strain. Fig. 2.4 shows the corresponding evolution of the phase field ξ and the dislocation pattern. In this latter plot, the dislocation lines are identified with the lines across which the phase field ξ jumps by one, or equivalently, with the level contours of $\eta + 1/2$ at integer heights. The phase field itself counts the number of dislocation which have passed over a given point of the slip plane, with proper accounting of the sign of traversal. Two well-differentiated regimes, with a transition point at $\gamma/\gamma_0 \sim 10$, are clearly discernible in Fig. 2.3: a first regime of 'microslip' dominated by dislocation bow-out; and a second regime characterized by generalized yielding. The saturation value of the resolved shear stress in this latter regime follows from global equilibrium as

$$b\tau_0 = b\tau^P + \frac{1}{|\Omega|}\sum_{i=1}^{N} f_i \tag{2.134}$$

i.e., the saturation stress is set by the mean obstacle strength. During the microslip regime, the value of the phase-field remains close to zero at the obstacles, which are essentially impenetrable to the dislocations. The dislocation loops move reversibly by bowing through the open spaces between obstacles, and by subsequently pinching behind the obstacles, leading to the formation of Orowan loops. As increasing numbers of dislocations bypass the obstacles by the bow-out mechanism, the number of Orowan loops surrounding the obstacles correspondingly increases, Fig. 2.4.

The details of this process are illustrated in Fig. 2.5, which zooms on a particular pair of obstacles and shows the evolution of the dislocation/obstacle interactions with increasing stress. In this figure, individual dislocations move from left to right and are color coded for ease of tracking.

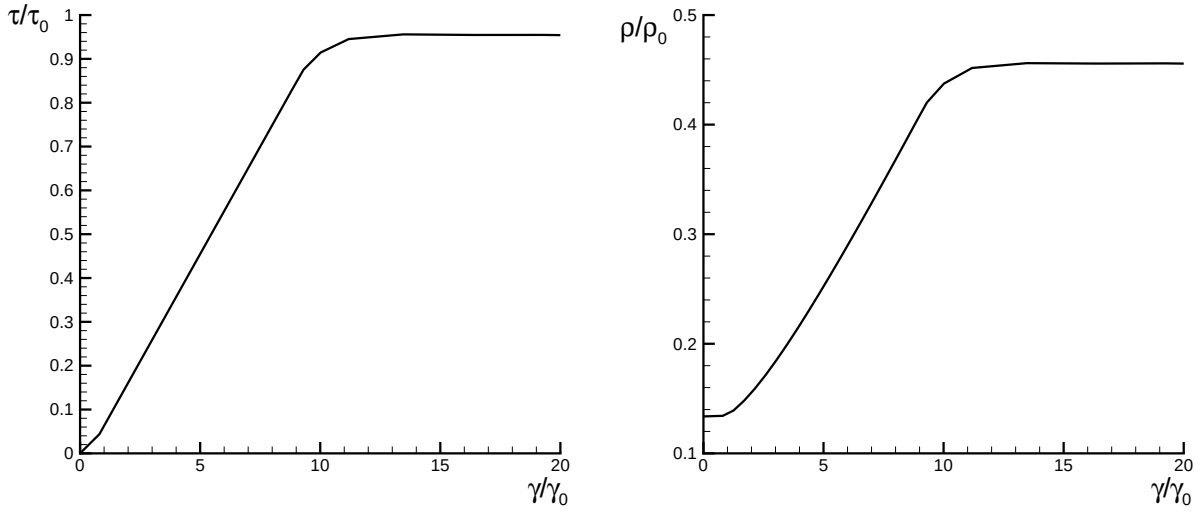

(a) Stress *vs.* strain

(b) Dislocation density *vs.* strain

Figure 2.3: Monotonic loading. (a) Applied shear stress *vs.* macroscopic slip strain. (b) Evolution of dislocation density with macroscopic slip strain.

Fig. 2.5 a shows the initial configuration. In Fig. 2.5 b, the dislocation has bypassed the obstacles and left Orowan loops in its trail. In subsequent frames, new dislocations arrive from the left, bow through the obstacles, and eventually bypass them, leaving behind additional Orowan loops. The ease with which the phase-field representation describes these geometrical and topological transitions is quite remarkable.

At larger applied stresses, the obstacles gradually yield and are overcome by the dislocations. Figs. 2.4 d-e correspond to the transitional phase between the micro-slip and the generalized yielding regimes. At sufficiently large applied stresses close to the saturation stress τ_0, all obstacles yield and are crossed by the dislocations. Under these conditions, the phase-field ξ increases uniformly without change of shape over the entire slip plane. In this regime, the level contours of ξ remain ostensibly unchanged, even as their height rises steadily, and the dislocation pattern becomes frozen in place, Fig. 2.4 e and 2.4 f. The hardening rate correspondingly drops and the stress-strain curve saturates asymptotically, Fig. 2.3 a. The presence of a saturation stage is consistent with observations of fcc single crystals undergoing single slip, e.g., during the easy glide or stage I or hardening.

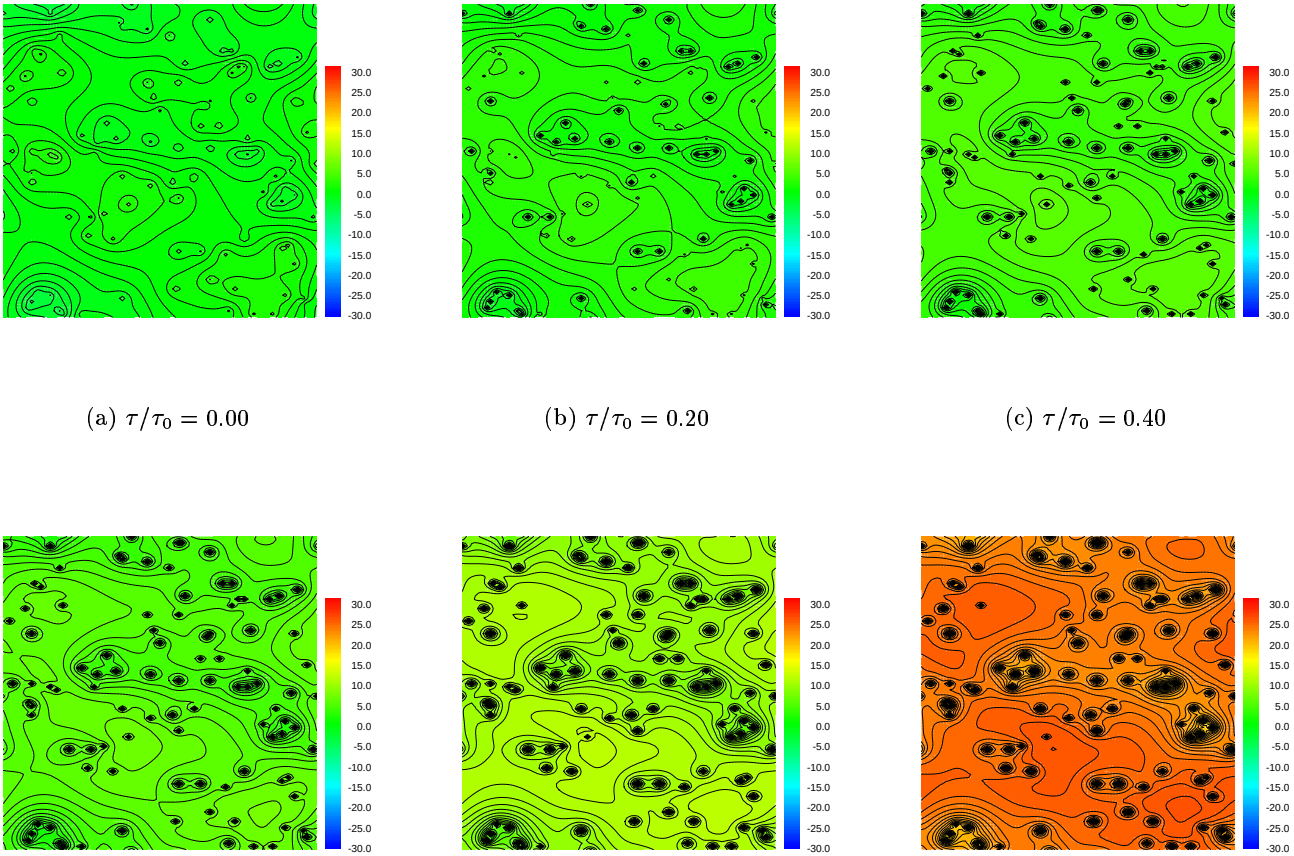

(a) $\tau/\tau_0 = 0.00$ (b) $\tau/\tau_0 = 0.20$ (c) $\tau/\tau_0 = 0.40$

(d) $\tau/\tau_0 = 0.60$ (e) $\tau/\tau_0 = 0.80$ (f) $\tau/\tau_0 = 0.99$

Figure 2.4: Evolution of the dislocation pattern in response to monotonic loading. Figs. (a)–(f) correspond to applied shear stresses $\tau/\tau_0 = 0.00$, 0.20, 0.40, 0.60, 0.80 and 0.99, respectively.

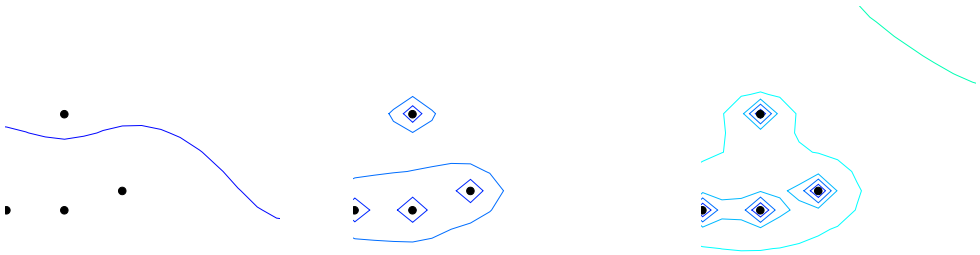

(a) $\tau/\tau_0 = 0.00$ (b) $\tau/\tau_0 = 0.20$ (c) $\tau/\tau_0 = 0.40$

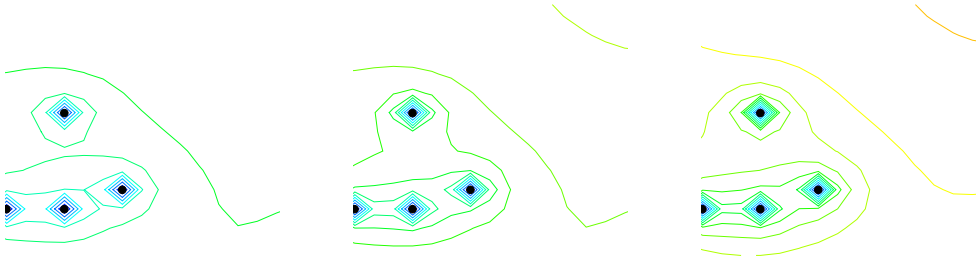

(d) $\tau/\tau_0 = 0.60$ (e) $\tau/\tau_0 = 0.80$ (f) $\tau/\tau_0 = 0.99$

Figure 2.5: Detailed view of a pair of obstacles as is bypassed by succeeding dislocations. Figs. (a)–(f) correspond to applied shear stresses $\tau/\tau_0 = 0.00$, 0.20, 0.40, 0.60, 0.80 and 0.99, respectively. Individual dislocations are color coded for ease of tracking.

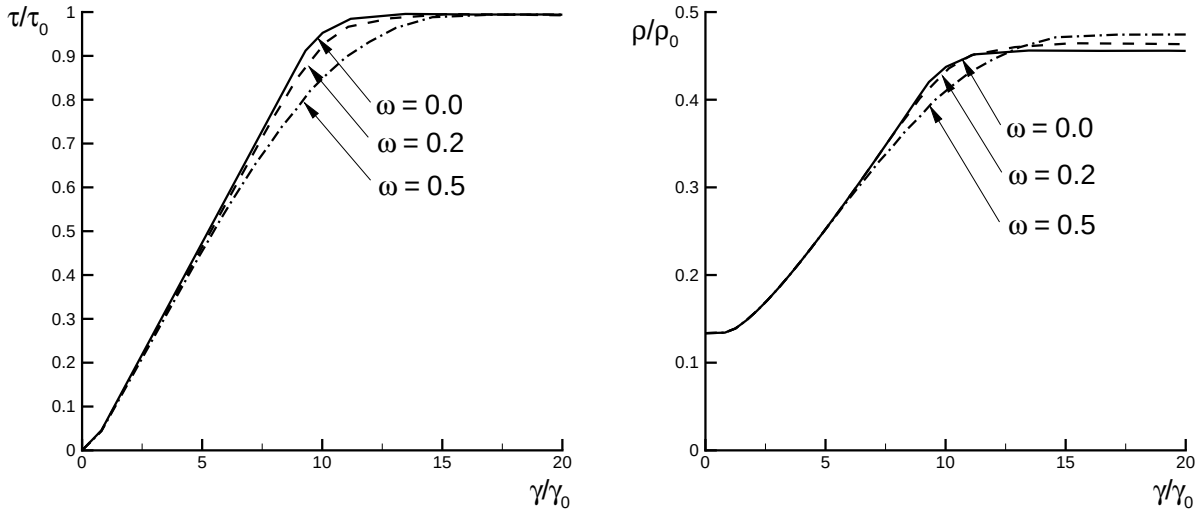

(a) Stress *vs.* strain

(b) Dislocation density *vs.* strain

Figure 2.6: Monotonic loading, effect of variable obstacle strength. (a) Applied shear stress *vs.* macroscopic slip strain. (b) Evolution of dislocation density with macroscopic slip strain.

The evolution of the dislocation line density (2.92) with slip strain is shown in Fig. 2.3 b. The computed dislocation densities are normalized by the reference density

$$\rho_0 = \frac{1}{bl} \tag{2.135}$$

which is the limiting or saturation density corresponding to an arrangement of parallel straight dislocations at intervals of b. As may be seen from the figure, the slip plane contains a nonzero dislocation density at zero slip strain. This initial density is induced by the long-range elastic-stress field s_0 of the secondary dislocations. The process of slip is accompanied by a steady increase in the dislocation line density (2.92). Dislocation multiplication and the proliferation of dislocation loops with increasing slip strain are clearly evident in Figs. 2.4 a-f. In the micro-slip regime, the increase in macroscopic slip is accompanied by a steady supply of dislocations bowing between the obstacles. This results in an initial parabolic growth rate, $\rho \sim \gamma^2$, Fig. 2.3 b. By contrast, as already noted when τ approaches the saturation stress τ_0 the dislocation pattern becomes frozen, e.g., Figs. 2.4 e and f, and the dislocation density remains ostensibly constant. This parabolic growth regime and

the subsequent saturation phase are indeed consistent with observation (54; 55). The ability of the theory to predict the evolution of the dislocation density, in addition to predicting hardening rates, is noteworthy.

Fig. 2.6 shows the effect of a variable obstacle strength on the computed stress-strain curve and dislocation density evolution during monotonic loading. In order to investigate this effect we consider obstacle strengths of the form $f = 10\mu b^2(1+\omega)$, with the random variable ω distributed uniformly within the intervals $[-0.2, 0.2]$ and $[-0.5, 0.5]$. When the obstacle strengths exhibit variability, the weakest obstacles tend to yield first and are overcome by dislocations, which are pinned at the stronger obstacles. Consequently, the transition between the microslip and generalized yielding regimes becomes more gradual. It is interesting to note that, since the average obstacle strength is the same in all cases, the saturation stress is not affected by the obstacle strength variability. This example illustrates the ability of the theory to account for the combined effect of obstacles of different species.

2.5.2 Cyclic loading

Next we investigate the behavior predicted by the theory under load reversal and cyclic loading. As in the preceding example, we assume a periodicity and take the unit cell Ω to be a square of dimension $100b$. We randomly select 100 points within the periodic cell as the obstacle sites and assign to these obstacles a uniform strengths $f = 10\mu b^2$. The Poisson's ratio ν is set to 0.3, and, for simplicity, we take the Peierls stress $\tau^P = 0$. We consider the cases of partial unloading, where the system is reloaded after a small amount of reverse yielding; and a fully reversed loading cycle. In both cases, the unloading and reloading events bring to the fore the irreversible and dissipative nature of the system, and necessitate full use of the incremental theory developed in Section 2.4.

Figs. 2.7 a and b show the predicted stress-strain curve and the evolution of the dislocation density in the cases of fully-reversed loading. The corresponding evolution of the dislocation ensemble is shown in Fig. 2.8 for the case of fully reversed loading. The various matching sections of these curves are labeled for ease of reference. The interval O–a of the curves in Fig. 2.7 simply reproduces the monotonic response described in the preceding section. Upon load reversal at point a, the system initially unloads elastically, Fig. 2.7 a, segment a–c. In this stage, the applied shear stress continues to push the dislocations against the obstacles in the loading direction. However, as

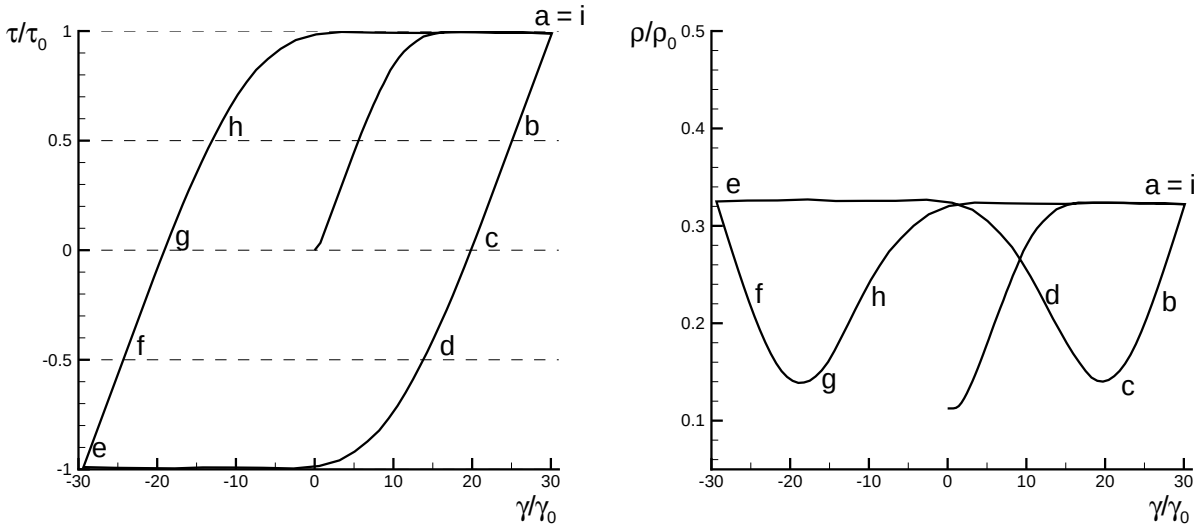

(a) Stress

(b) Dislocation density

Figure 2.7: Cyclic behavior. Labels a–i indicate the loading sequence. (a) Applied resolved shear stress *vs.* average slip (b) Evolution of dislocation density *vs.* average slip.

the applied load is decreased the force exerted by the dislocations on the obstacles correspondingly decreases and, consequently, remains below the obstacle strength. Under these conditions, the dislocations remain pinned at the obstacles and simply recoil elastically. This process gives the linear unloading branch a–c in the stress-strain curve, Fig. 2.7 a.

It should be carefully noted that, owing to the frictional sliding of the dislocations over the obstacles that occurs during the loading state, the interaction forces between the dislocations and the obstacles do not vanish when the applied shear stress is reduced to zero. Instead, the system is left in a state of permanent or residual deformation in which the dislocation/obstacle force system is self-equilibrated. The corresponding dislocation pattern for the fully reversed case is shown in Fig. 2.8 c. This remanent field is in analogy to the self-equilibrated residual stress fields which remain in elastic-plastic solids upon unloading. The combination of a reversed applied stress and the residual force field causes the system to yield prematurely in the reserve direction, Fig. 2.7 a, point d, and thus the theory predicts the Bauschinger effect.

Once reverse yielding commences, the obstacles continue to oppose the motion of the dislocations, which now takes place in the reverse loading direction. In particular, the frictional forces at

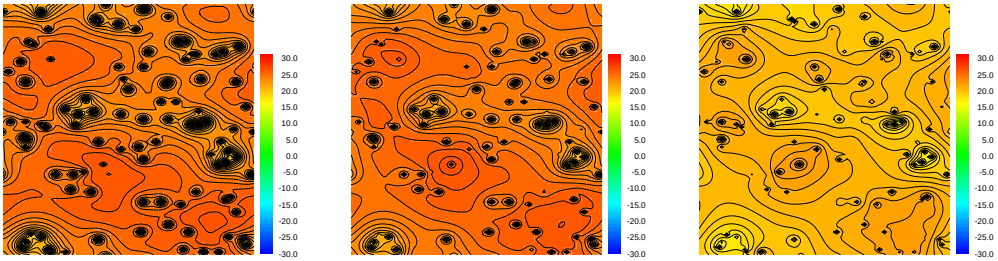

(a) $\tau/\tau_0 = 0.99$ (b) $\tau/\tau_0 = 0.50$ (c) $\tau/\tau_0 = 0.00$

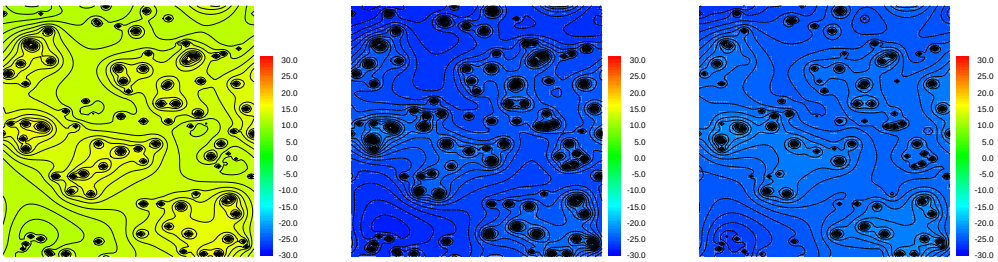

(d) $\tau/\tau_0 = -0.50$ (e) $\tau/\tau_0 = -0.99$ (f) $\tau/\tau_0 = -0.50$

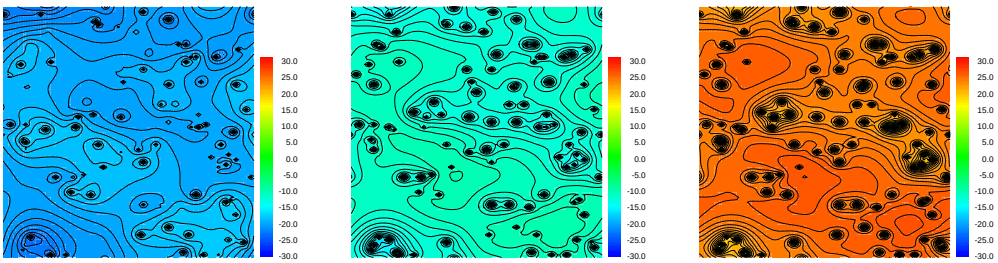

(g) $\tau/\tau_0 = 0.00$ (h) $\tau/\tau_0 = -0.50$ (i) $\tau/\tau_0 = 0.99$

Figure 2.8: Evolution of the dislocation pattern in response to cyclic loading. Figs. (a)–(i) correspond to $\tau/\tau_0 = 0.99$, 0.50, 0.00, -0.50, -0.99, -0.50, 0.00, 0.50, 0.99, respectively.

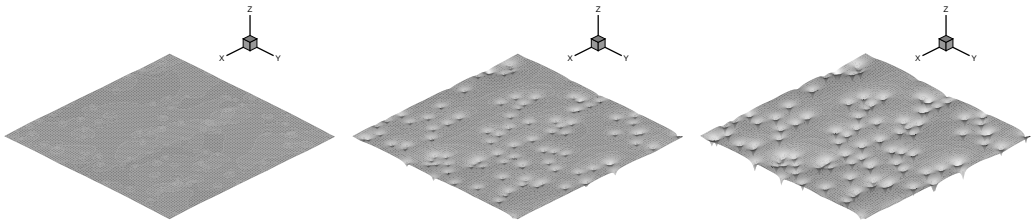

(a) $\tau/\tau_0 = 0.00$ (b) $\tau/\tau_0 = 0.30$ (c) $\tau/\tau_0 = 0.60$

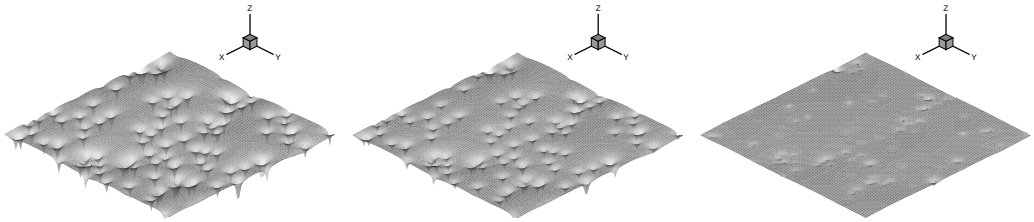

(d) $\tau/\tau_0 = 0.99$ (e) $\tau/\tau_0 = 0.60$ (f) $\tau/\tau_0 = 0.00$

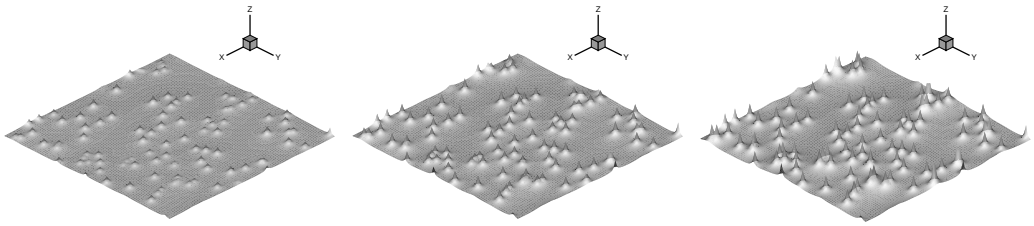

(g) $\tau/\tau_0 = -0.30$ (h) $\tau/\tau_0 = -0.60$ (i) $\tau/\tau_0 = -0.99$

Figure 2.9: Three-dimensional view of the evolution of the phase field during a fully reversed loading cycle, showing the switching of the cusps at the obstacles upon unloading and reloading. Figs. (a)–(i) correspond to $\tau/\tau_0 = 0.00$, 0.30, 0.60, 0.99, 0.60, 0.00, -0.30, -0.60, -0.99, respectively.

the obstacles switch sign relative to the loading phase. This process of switching is clearly apparent in Fig. 2.9, which shows the evolution of the phase-field during the loading cycle. Thus, during the loading phase the obstacles pull down on the phase-field, Fig. 2.9 b-d, causing it to cusp downward at the obstacles, whereas during the reverse loading phase the obstacles pull up on the phase-field, Fig. 2.9 g-i, causing it to cusp upward.

The stress-strain curve shown in Fig. 2.10 reveals that the system exhibits 'fading memory'. Thus, when the system is reloaded, the stress-strain curve gradually transitions towards the virgin loading curve, and, with sufficient reloading, the system eventually 'forgets' the unloading cycle. The extent of this loss of memory depends on the extent of reverse yielding. Consider, for instance, the case in which unloading is purely elastic and no reverse yielding occurs. This corresponds to reloading, from point b in Fig. 2.10. Because no reverse sliding over obstacles has occurred at this point, the dislocation/obstacle configuration remains undisturbed. Consequently, upon reloading all the obstacles yield simultaneously and the system exhibits an abrupt yield point coinciding exactly with the point of unloading, point a in Fig. 2.10. Thus, in this case no loss of memory occurs and the system exhibits *return-point memory* in the sense of Sethna *et al.* (53). This type of behavior should now be compared with that corresponding to a limited amount of reverse loading. In this case, the dislocations slip over the obstacles in the reverse loading direction, and some of the details of the dislocation/obstacle configuration established at the unloading point d are lost in the process. When the system is reloaded, point e in Fig. 2.10, the obstacles yield anew gradually and not all at once, as in the case of a purely elastic unloading, and the system exhibits a gradual transition towards the virgin loading curve, Fig. 2.10, segment e-f. In the case of fully reversed unloading, Fig. 2.7, the amount of reverse yielding, segment d-e, is large enough that the unloading point is effectively wiped out from the memory of the system, with the result that the reloading curve e-i is ostensibly identical to the unloading curve a-e. These trends are in good agreement with the experimental cyclic stress-strain data for structural steels reported by Ortiz and Popov (56), which was obtained from tests specially designed to exhibit the fading memory effect just described.

The evolution of the dislocation density during a loading cycle is of considerable interest as well, Fig. 2.7 b . Thus, upon unloading the dislocation density decreases as a result of the elastic relaxation of the dislocation lines. The dislocation density bottoms out—but does not vanish

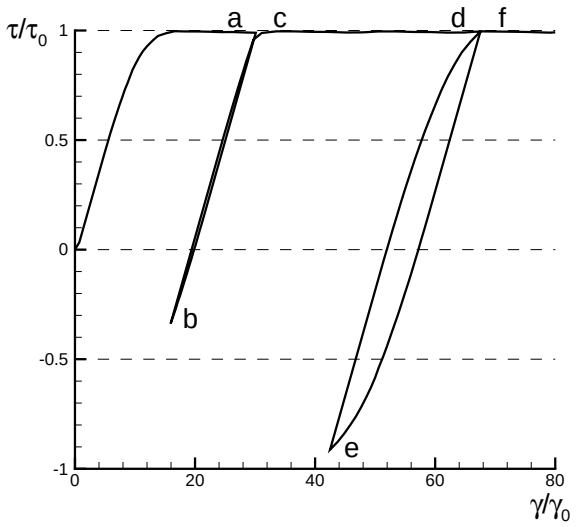

Figure 2.10: Cyclic reloading behavior for various extents of reverse yielding, exhibiting fading memory effect. Labels a–i indicate the loading sequence.

entirely—upon the removal of the applied stress, Fig. 2.7 b, point c, as some dislocations remain locked in within the system in the residual state, Fig. 2.8c. The dislocation density increases again during reverse loading, Fig. 2.7 b, segment c-d, and the cycle is repeated during reloading, Fig. 2.7b, segment c-d, segment e-i, giving rise to a dislocation density *vs.* slip strain curve in the form of a 'butterfly'. This type of behavior is indeed observed experimentally (57). It also arises in models of the stored energy of cold work (58), and is in analogy to the hysteretic loops exhibited by magnetic systems (59; 53; 60).

Finally, we exercise the model over the range of periodic cell sizes $10^2 b - 10^5 b$, while at the same time keeping the number of obstacles constant at 100. The corresponding obstacles density $c = N/|\Omega|$ consequently varies from $10^{-2}/b^2$ to $10^{-8}/b^2$. Of primary interest here is to ascertain how the macroscopic behavior of the slip plane depends on the obstacle density. Our calculations show that the stress-strain curve, when expressed in terms of the normalized variables τ/τ_0 and γ/γ_0 is ostensibly independent of c. It should be carefully noted that, for obstacles of uniform strength, $\tau_0 = fc$, and thus the saturation strength scales in direct proportion to the obstacle density. The variation of the dislocation density evolution with c is shown in Fig. 2.11. It is interesting to note from this figure that the saturation value of the dislocation density scales as $1/\sqrt{c}$, but that

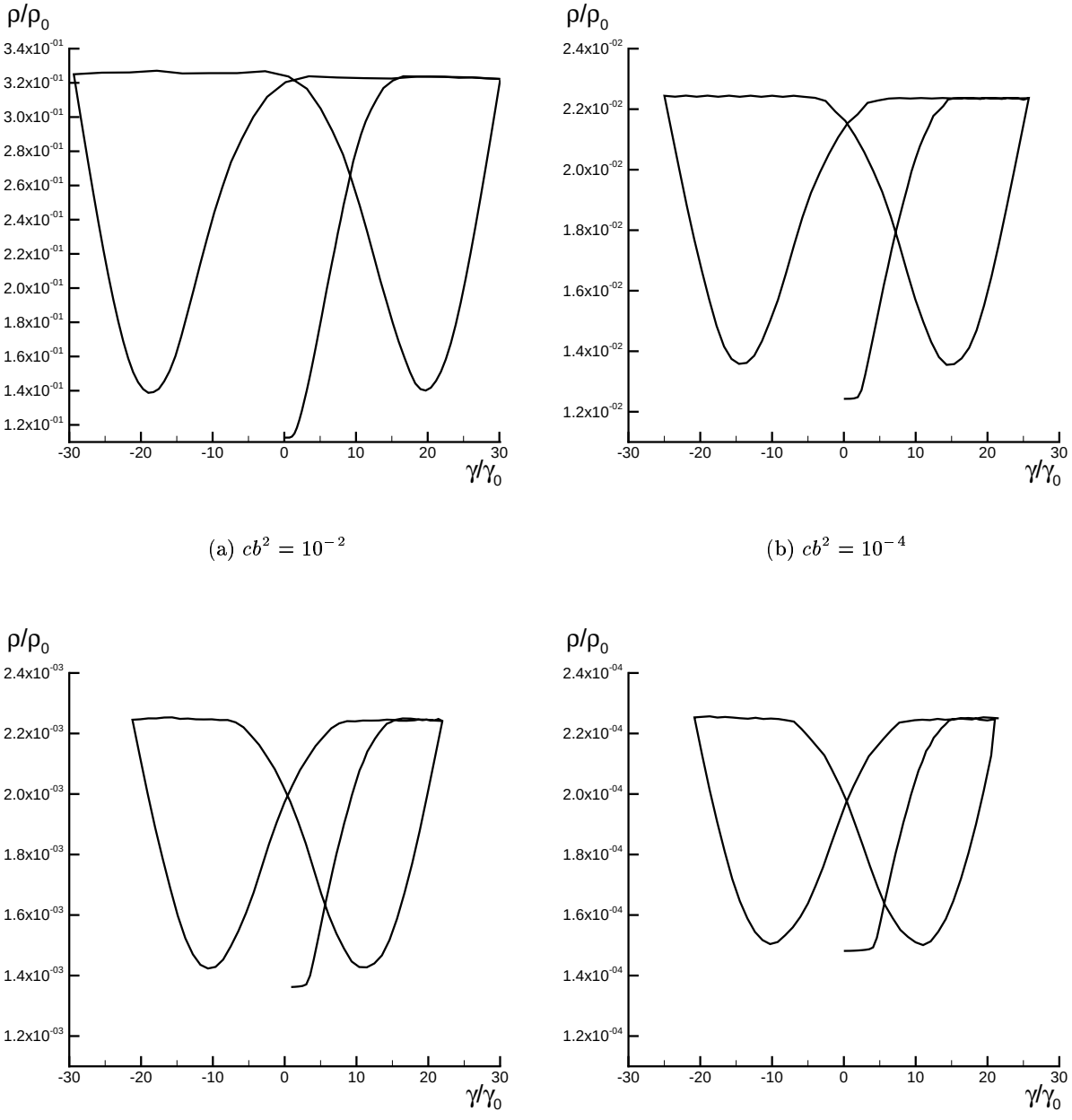

(a) $cb^2 = 10^{-2}$

(b) $cb^2 = 10^{-4}$

(c) $cb^2 = 10^{-6}$

(d) $cb^2 = 10^{-8}$

Figure 2.11: Evolution of the dislocation density with macroscopic slip strain during cyclic loading for different values of the obstacle density c.

otherwise the evolution of the dislocation density with macroscopic slip strain remains ostensibly identical in all cases.

This example also serves to underscore the ability of the theory to effectively deal with large domains of analysis. Thus, owing to the absence of a computational grid the complexity of the calculations scales with the number of obstacles and is otherwise independent of the cell size, which enables the consideration of large cells sizes in the relevant range of observation.

2.5.3 Dislocation line-energy anisotropy

We conclude this section with a brief parametric study of the effect of dislocation line-energy anisotropy on the hardening characteristics of the system. In particular, we consider systems which are identical in every respect except for the value of Poisson's ratio. By virtue of Eq. (2.51), different choices of Poisson's ratio result in different ratios between the energy per unit length of edge and screw segments. We recall that, for $\nu > 0$, the minimum (maximum) energy per unit length is attained for pure screw (edge) segments. All remaining parameters are as in the preceding examples. In particular, the unit cell dimension is $100b$, the number of obstacles is 100, the obstacle strength is $f = 10\mu b^2$, Poisson's ratio ν is 0.3, and the Peierls stress τ^P is set to 0.

Fig. 2.12 shows the predicted stress-strain curves and dislocation density evolution for $\nu = 0.0$, 0.3 and 0.5. Since the saturation stress τ_0 solely depends on obstacle strength and concentration, all three stress-strain curves saturate at the same level. By contrast, as ν is increased the dislocation line-energy of both edge and screw segments increases and the system correspondingly stiffens, with the result that lower values of the slip strain are attained, Fig. 2.12 a. The rate of dislocation multiplication also decreases with increasing ν, Fig. 2.12 b. Perhaps more interestingly, Fig. 2.13 shows the effect of the anisotropy on the dislocation geometry. Thus, as Poisson's ratio is increased screw segments become energetically favorable relative to edge segments, and the dislocation pattern exhibits a preponderance of elongated screw segments, Fig. 2.13 c.

2.6 Summary and concluding remarks

We have developed an analytically tractable phase-field theory of dislocation dynamics, strain hardening and hysteresis in ductile single crystals at low temperatures. The phase-field representation

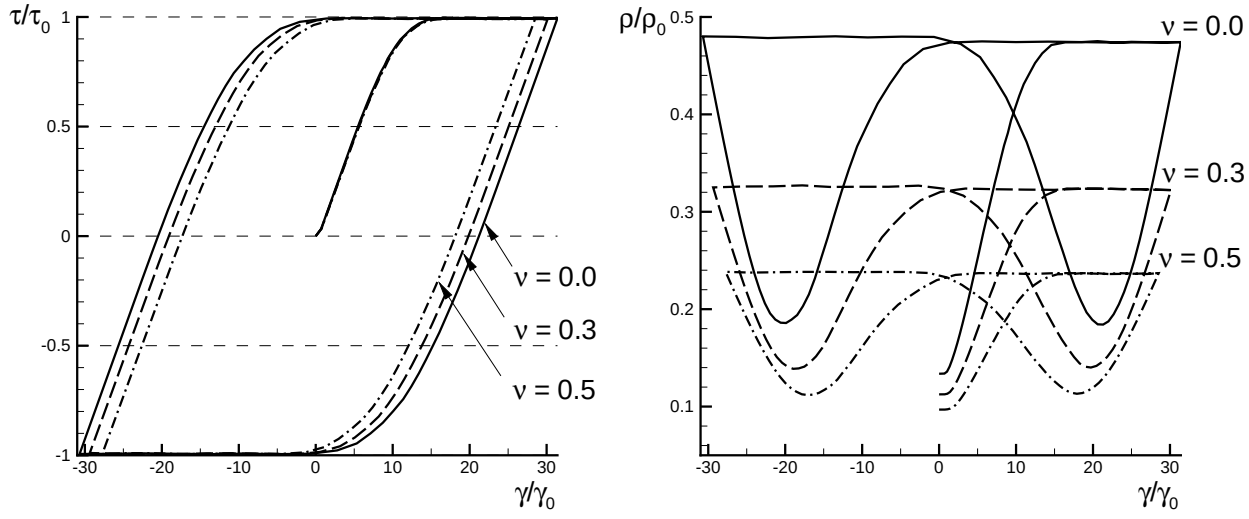

(a) Stress

(b) Dislocation Density

Figure 2.12: Effect of dislocation line-energy anisotropy on the hardening characteristics of the system. (a) Applied shear stress *vs.* macroscopic slip strain. (b) Evolution of dislocation density with macroscopic slip strain.

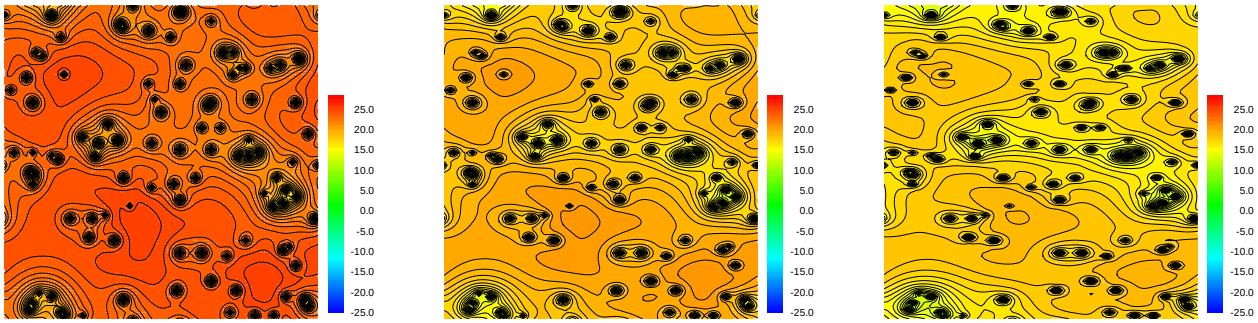

(a) $\nu = 0.0$

(b) $\nu = 0.3$

(c) $\nu = 0.5$

Figure 2.13: Effect of dislocation line-energy anisotropy on the evolution of the dislocation pattern. Figs. (a)–(c) correspond to $\tau/\tau_0 = 0.99$, and $\gamma/\gamma_0 = 23$, 20 and 18, respectively.

furnishes a simple and effective means of tracking the motion of large numbers of dislocations within discrete slip planes through random arrays of point obstacles under the action of an applied shear stress. The theory rests on a variational framework for dissipative systems and accounts for energetic and kinetic effects (23; 24; 25; 26; 27). The energetics accounted for in the theory include the core energy of the dislocations, represented by a piecewise quadratic Peierls potential (7); the long-range elastic interactions between primary dislocations and between primary and forest dislocations; and the energy of interaction with the applied resolved shear stress. The kinetics of the system stem from the assumed irreversible interactions between dislocations and obstacles, and from lattice friction, and result in hardening, path dependency, and hysteresis in the macroscopic behavior.

The theory predicts a range of behaviors which are in qualitative agreement with observation. Thus, in the base case of single slip under monotonic loading, the theory predicts saturation at a stress which depends on obstacle strength and density. It also predicts dislocation multiplication at an initial parabolic rate, during a 'microslip' regime, followed by saturation at a maximum dislocation density. The ease with which the phase-field representation allows for complex geometrical and topological transitions, as the dislocation ensemble percolates through the obstacles, is quite remarkable. The cyclic behavior predicted by the theory is particularly noteworthy. As required, the theory predicts the essential phenomena of loading/unloading irreversibility and hysteresis. But the theory also captures more subtle aspects of the cyclic behavior of crystals, such as the Bauschinger effect, consisting of the premature yielding of a slip system under reverse loading; the fading memory effect, whereby reverse yielding gradually eliminates the influence of previous loading; and the evolution of the dislocation density, leading to characteristic 'butterfly' curves also observed in magnetic systems (53; 59; 60).

There are other aspects of the theory which help to make contact with actual materials. For instance, it is possible within the theory to account for obstacles of different species, and to accord to them varying densities and strengths. This furnishes an avenue for building into the theory results from recent work concerned with dislocation-dislocation interactions (8; 35; 36; 37).

Chapter 3

Statistical mechanics of dissipative systems

3.1 Introduction

We propose a generalization of classical statistical mechanics which describes the behavior of dissipative systems placed in contact with a heat bath. In contrast to conventional statistical mechanics, which assigns probabilities to the *states* of the system, the generalized theory assigns probabilities to the *trajectories* of the system. The conditional probability of pairs of states at two different times is given by a path integral.

We are interested in systems that are dissipative *ab initio*, e.g., as a result of internal friction, viscosity, or some other dissipative mechanism. In particular, the systems are irreversible, path dependent, and exhibit hysteresis. The advantage of this theory is that it allows for hysteresis and path dependency in systems in contact with a heat bath. This model also allows to understand how a heat bath influences the behavior of a dissipative system; what are the statistical properties of its trajectories; and how the effective behavior depends on temperature.

The interaction between dislocations and obstacles in the glide plane is dissipative in nature, resulting in path dependency and hysteresis. The central objective of this chapter is to characterize the evolution of the phase field at finite temperatures. The dislocation ensemble is solved using a Path Integral Metropolis Monte Carlo algorithm and predicts a range of behaviors that are in agreement with experimental observation. A variety of different models (53; 61) and Monte Carlo algorithms (62; 63) are used to study the hysteretic behavior of magnetic systems. In those models the hysteresis is modeled using an energy barrier, in our model this energy barrier is given by the

strength of the obstacles that populate the slip system.

Also we develop a mean field approximation of the phase-field which qualitatively reproduces the results of the full model. Given the simplicity of the calculations with the mean field approximation, we analyze the effect of the temperature in a wide range of obstacle densities and strain rates.

In sections 3.2 and 3.3 we develop the theory which describes the behavior of dissipative systems in contact with a heat bath. One of the advantages of the theory is that some simple systems are analytically-tractable. In section 3.4 we present four analytically-tractable examples which illustrate the effect of temperature on the mean trajectories, hysteresis and drift of the system. As an example we analyze the evolution of a viscous system, the transition probability obtained is equivalent to the transition probability computed using Langevin equation for Brownian motion, in the thermodynamic equilibrium limit (64; 65). In section 3.5 we use a Metropolis Monte Carlo algorithm to simulate the evolution of the phase field of dislocations at finite temperature. In section 3.6 we compute the mean field approximation of the system.

3.2 Variational principles of dissipative systems

For definiteness, we consider systems whose state is defined by an N-dimensional array $\boldsymbol{q}$ of generalized coordinates. The energetic of the system is described by an energy function $E(\boldsymbol{q}, t)$. The explicit time dependence of E may arise, e.g., as a result of the application to the system of a time-dependent external field. In addition, the system is assumed to possess *viscosity*, and, thus, the equilibrium equations are of the form:

$$\boldsymbol{f} \equiv \frac{\partial E}{\partial \boldsymbol{q}}(\boldsymbol{q}, t) + \boldsymbol{f}^{\text{vis}}(\dot{\boldsymbol{q}}) = 0 \tag{3.1}$$

where $\boldsymbol{f}^{\text{vis}}$ are the viscous forces. These equilibrium equations define a set of ordinary differential equations which, given appropriate conditions at, e.g., $t = 0$, can be solved for the trajectory $\boldsymbol{q}(t)$, $t \geq 0$.

If the system is conservative, i.e., if $\boldsymbol{f}^{\text{vis}} = \boldsymbol{0}$, the instantaneous state $\boldsymbol{q}(t)$ of the system at time t follows directly from energy minimization, i.e., from the problem:

$$E\big(\boldsymbol{q}(t), t\big) = \min_{\boldsymbol{q}' \in \mathbb{R}^N} E(\boldsymbol{q}', t) \tag{3.2}$$

In order to extend this variational framework to dissipative systems, we resort to time discretization, leading to a *sequence* of minimization problems of the form (3.2) (23; 24; 26). Thus, we consider a *time-discretized* incremental process consisting of a sequence of states $\mathbf{q}_{n-1}$ at times $t_0 = 0, \ldots,$ t_{n-1}, $t_n = t_{n-1} + \triangle t, \ldots$. We additionally assume that the viscous forces $\boldsymbol{f}^{\text{vis}}$ derive from a kinetic potential $\phi(\dot{\boldsymbol{q}})$ through the relation:

$$\boldsymbol{f}^{\text{vis}} = \frac{\partial \phi}{\partial \dot{\mathbf{q}}}(\dot{\boldsymbol{q}}) \tag{3.3}$$

and introduce the incremental work function:

$$\begin{aligned} W(\boldsymbol{q}_n, \boldsymbol{q}_{n-1}) &= E(\boldsymbol{q}_n) - E(\mathbf{q}_{n-1}) \\ &+ \min_{\{paths\}} \int_{t_{n-1}}^{t_n} \phi\big(\dot{\mathbf{q}}(t)\big)\, dt \end{aligned} \tag{3.4}$$

where the minimum is taken over all paths $\boldsymbol{q}(t)$ such that $\boldsymbol{q}(t_{n-1}) = \boldsymbol{q}_{n-1}$ and $\boldsymbol{q}(t_n) = \boldsymbol{q}_n$. The fundamental property of the incremental work function $W(\mathbf{q}_n, \boldsymbol{q}_{n-1})$ is that it acts as a potential for the forces $\boldsymbol{f}_n$ at time t_n, i.e.,

$$\boldsymbol{f}_n = \frac{\partial W}{\partial \boldsymbol{q}_n}(\boldsymbol{q}_n, \mathbf{q}_{n-1}) \tag{3.5}$$

In order to verify this property, we may consider a small perturbation $\boldsymbol{q}_n \to \boldsymbol{q}_n + \delta \boldsymbol{q}_n$, leading to a corresponding perturbation of the path $\boldsymbol{q}(t) \to \boldsymbol{q}(t) + \delta \boldsymbol{q}(t)$, with $\delta \boldsymbol{q}(t_{n-1}) = \delta \boldsymbol{q}_{n-1} = \mathbf{0}$. Then, it follows that

$$\begin{aligned} \delta W(\boldsymbol{q}_n, \boldsymbol{q}_{n-1}) &= \frac{\partial E}{\partial \boldsymbol{q}}(\boldsymbol{q}_n) \cdot \delta \boldsymbol{q}_n + \boldsymbol{f}_n^{\text{vis}} \cdot \delta \boldsymbol{q}_n \\ &+ \int_{t_{n-1}}^{t_n} \boldsymbol{f}^{\text{vis}}\big(\dot{\boldsymbol{q}}(t)\big) \cdot \delta \dot{\boldsymbol{q}}(t)\, dt \end{aligned} \tag{3.6}$$

But the integral on the right-hand side of this equation is to be evaluated along the minimizing path, and hence it vanishes identically. This gives the identity

$$\delta W(\boldsymbol{q}_n, \boldsymbol{q}_{n-1}) = \left\{ \frac{\partial E}{\partial \boldsymbol{q}}(\boldsymbol{q}_n) + \boldsymbol{f}_n^{\text{vis}} \right\} \cdot \delta \mathbf{q}_n \tag{3.7}$$

Since the variation $\delta \boldsymbol{q}_n$ is arbitrary, it follows that

$$\frac{\partial W}{\partial \boldsymbol{q}_n}(\boldsymbol{q}_n, \boldsymbol{q}_{n-1}) = \frac{\partial E}{\partial \boldsymbol{q}}(\boldsymbol{q}_n) + \boldsymbol{f}_n^{\text{vis}} = \boldsymbol{f}_n \tag{3.8}$$

as stated. From this property it follows that the equilibrium equation $\boldsymbol{f}_n = \mathbf{0}$ is the Euler-Lagrange equation corresponding to the minimum principle:

$$\min_{\boldsymbol{q}_n} W(\boldsymbol{q}_n, \boldsymbol{q}_{n-1}) \tag{3.9}$$

This behavior is indistinguishable from that of a conservative system with 'energy' $W(\boldsymbol{q}_n, \boldsymbol{q}_{n-1})$. However, it should be carefully noted that W is determined by both the *energetics* and the *kinetics* of the system. Consequently, W depends on the initial conditions $\boldsymbol{q}_{n-1}$ for the time step and, therefore, varies from step to step, which in turn allows for path dependency and hysteresis, as required. A simple situation arises when the kinetic potential $\phi(\dot{\boldsymbol{q}})$ is convex and coercive, i.e., it grows as $|\dot{\boldsymbol{q}}|^p$, for some $p \in (1, \infty)$, for large $|\dot{\boldsymbol{q}}|$. Then, the minimizing path is unique and consists of a straight segment joining $\boldsymbol{q}_{n-1}$ and $\boldsymbol{q}_n$. Under these conditions, the corresponding incremental work function is

$$W(\boldsymbol{q}_n, \boldsymbol{q}_{n-1}) = E(\boldsymbol{q}_n) - E(\boldsymbol{q}_{n-1}) + \triangle t\, \phi\left(\frac{\triangle \boldsymbol{q}}{\triangle t}\right) \tag{3.10}$$

where we write $\triangle \boldsymbol{q} = \boldsymbol{q}_n - \boldsymbol{q}_{n-1}$.

Now, imagine placing the system just described in contact with a heat bath at absolute temperature T. The objective is to predict the ensuing behavior of the system. For conservative systems, such behavior is predicted by standard Gibbsian statistical mechanics, to wit: the probability of finding a state $\boldsymbol{q}$ at time t obeys Boltzmann's distribution, i.e., is proportional to $\exp\{-\beta E(\boldsymbol{q}, t)\}$, where $\beta = 1/k_B T$ and k_B is Boltzmann's constant. In particular, the states of the system at two different times are uncorrelated. We proceed to show that the analogy between the minimum principles (3.2) and (3.9) provides a basis for generalizing Gibbs's prescription to dissipative systems. However, in contrast to conventional statistical mechanics, which assigns probabilities to the *states* of the system, the extended theory assigns probabilities to the *trajectories* of the system.

3.3 Statistical mechanics of dissipative systems

We begin by assuming that the incremental processes are Markovian, i.e., $\boldsymbol{q}_n$ is correlated to $\boldsymbol{q}_{n-1}$ but not to earlier states. Let $p(\boldsymbol{q}_n, \boldsymbol{q}_{n-1})$ be the joint probability of $\boldsymbol{q}_n$ and $\boldsymbol{q}_{n-1}$, and let

$$p(\boldsymbol{q}_{n-1}) = \int p(\boldsymbol{q}_n, \boldsymbol{q}_{n-1})\, d^N q_n \tag{3.11a}$$

$$p(\boldsymbol{q}_n) = \int p(\boldsymbol{q}_n, \boldsymbol{q}_{n-1})\, d^N q_{n-1} \tag{3.11b}$$

be the corresponding probabilities of $\boldsymbol{q}_n$ and $\mathbf{q}_{n-1}$. Then the conditional probability of $\boldsymbol{q}_n$ given $\boldsymbol{q}_{n-1}$ is

$$p(\boldsymbol{q}_n|\boldsymbol{q}_{n-1}) = \frac{p(\boldsymbol{q}_n, \boldsymbol{q}_{n-1})}{p(\mathbf{q}_{n-1})} \tag{3.12}$$

This probability may also be interpreted as the transition probability from state $\boldsymbol{q}_{n-1}$ to the new state $\mathbf{q}_n$. *We postulate that the transition probability* $p(\boldsymbol{q}_n|\boldsymbol{q}_{n-1})$ *is Gibbsian*, i.e.,

$$p(\boldsymbol{q}_n|\boldsymbol{q}_{n-1}) = \frac{1}{Z(\boldsymbol{q}_{n-1})} e^{-\beta W(\mathbf{q}_n, \boldsymbol{q}_{n-1})} \tag{3.13}$$

where

$$Z(\boldsymbol{q}_{n-1}) = \int e^{-\beta W(\boldsymbol{q}_n, \boldsymbol{q}_{n-1})}\, d^N q_n \tag{3.14}$$

is an incremental partition function. It therefore follows that

$$p(\boldsymbol{q}_n) = \int \frac{1}{Z(\boldsymbol{q}_{n-1})} e^{-\beta W(\mathbf{q}_n, \boldsymbol{q}_{n-1})} p(\boldsymbol{q}_{n-1})\, d^N q_{n-1} \tag{3.15}$$

Iterating this relation we obtain

$$p(\boldsymbol{q}_n) = \int \cdots \int \left\{ \prod_{i=0}^{n-1} \frac{e^{-\beta W(\boldsymbol{q}_{i+1}, \boldsymbol{q}_i)}}{Z(\boldsymbol{q}_i)} \right\} p(\boldsymbol{q}_0)\, d^N q_{n-1} \ldots d^N q_0 \tag{3.16}$$

In the limit of $\triangle t \to 0$ and $n \to \infty$ at fixed $t = n\triangle t$, (3.16) defines a path integral of the form (see, e.g., (66)):

$$p(\boldsymbol{q}_t|\boldsymbol{q}_0) = \int \cdots \int e^{-\beta \mathcal{W}[\boldsymbol{q}]} \mathcal{D}q \tag{3.17}$$

for some system-dependent work functional $\mathcal{W}[\boldsymbol{q}]$. This path integral gives the conditional probability $p(\boldsymbol{q}_t|\boldsymbol{q}_0)$ of finding the system in state $\boldsymbol{q}_t$ at time $t \geq 0$ given that the system is in state $\boldsymbol{q}_0$ at time $t = 0$. The integrand of (3.17) may be interpreted as relating to the probability of individual trajectories $q(\tau)$. More precisely, given two trajectories $\boldsymbol{q}_1(\tau)$ and $\boldsymbol{q}_2(\tau)$, their relative probabilities are

$$\frac{p[\boldsymbol{q}_1]}{p[\boldsymbol{q}_2]} = \frac{e^{-\beta W[\boldsymbol{q}_1]}}{e^{-\beta W[\boldsymbol{q}_2]}} \tag{3.18}$$

It is noteworthy that, in contrast to the conservative case, the presence of kinetics renders states of the system at different types *correlated*. However, this correlation may be expected to decay with elapsed time, conferring the system a *fading memory* property.

3.4 Illustrative examples

Here we present simple analytically tractable examples which provide a first illustration of the theory. In addition to their value as illustrative examples, these simple models should also be useful as a basis for constructing *mean-field* approximations to more complex systems.

3.4.1 Example I: Conservative system

Consider the conservative unidimensional system of an harmonic oscillator with an external force $f(t)$. The incremental work function is

$$W(q_{n+1}, q_n) = \frac{\kappa}{2}(q_{n+1}^2 - q_n^2) - f_{n+1}q_{n+1} + f_n q_n \tag{3.19}$$

where $q \in \mathbb{R}$ and κ is the spring constant. The transition probability from a state q_n to a new state q_{n+1} is

$$p(q_{n+1} \mid q_n) = \frac{1}{Z(q_n)} e^{-\beta \Delta W(q_{n+1}, q_n)} \tag{3.20}$$

where

$$Z(q_n) = \int_{-\infty}^{\infty} e^{-\beta \Delta W(q_{n+1}, q_n)} dq_{n+1} \tag{3.21}$$

Replacing the expression for the incremental work (3.19) in equation (3.21) we obtain the incremental partition function of the system for a given state q_n

$$Z(q_n) = \sqrt{\frac{2\pi}{\beta\kappa}} e^{\beta(\frac{\kappa}{2}q_n^2 - f_n q_n + \frac{f_{n+1}^2}{2\kappa})} \tag{3.22}$$

We can obtain now the probability of having a state q_{n+1} as:

$$p(q_{n+1}) = \int ... \int \left\{ \prod_{i=0}^{n} \frac{e^{-\beta \Delta W(q_{i+1}, q_i)}}{Z(q_i)} \right\} p(q_0) dq_0 ... dq_n \tag{3.23}$$

$$= \frac{1}{e^{\beta \frac{f_{n+1}^2}{2\kappa}} \sqrt{\frac{2\pi}{\beta\kappa}}} e^{-\beta(\frac{\kappa}{2}q_{n+1}^2 + f_{n+1}q_{n+1})} \tag{3.24}$$

where we have used the fact that $\int p(q_0) dq_0 = 1$.

Equation (3.24) is the Boltzmann distribution $p(q_{n+1}) = \frac{1}{Z} e^{-\beta E(q_{n+1})}$, where Z is the partition function. The system is conservative so the probability $p(q_{n+1})$, as expected depends on the energy of the state q_{n+1} and not in the history of the system.

3.4.2 Example 2: Viscous system

A viscous system is characterized by a kinetic potential of the form:

$$\phi(\dot{q}) = \frac{\eta}{2} \dot{q}^2 \tag{3.25}$$

where $q \in \mathbb{R}$, η is the viscosity. The corresponding incremental work function for this system is

$$W(q_n, q_{n-1}) = \frac{\eta}{2\triangle t} (q_n - q_{n-1})^2 \tag{3.26}$$

As before we can compute the incremental partition function of the system for a given state q_n:

$$Z(q_n) = \frac{2\pi \triangle t}{\beta \eta} \tag{3.27}$$

Inserting the result in (3.16) yields

$$p(q_n) = \int \dots \int \left(\frac{2\pi \triangle t}{\beta \eta} \right)^{-n/2} \exp \left\{ -\frac{\beta \eta}{2 \triangle t} \sum_{i=0}^{n-1} \eta (q_{i+1} - q_i)^2 \right\} p(q_0)\, dq_{n-1} \dots dq_0 \tag{3.28}$$

Taking the limit as $\Delta t \to 0$ and $n \to \infty$ in equation (3.28) such that $n\Delta t = t$ we obtain

$$p(q_n) = \int ... \int e^{-\beta \int_0^t \mathcal{F}(\tau,q,\dot{q})d\tau} \; \mathcal{D}q \tag{3.29}$$

where $\mathcal{D}q = \left(\frac{2\pi\Delta t}{\beta\eta}\right)^{-\frac{n}{2}} dq_1 ... dq_n$ and

$$\mathcal{F}(\tau, q, \dot{q}) = \frac{\eta}{2}\dot{q}^2 \tag{3.30}$$

The integral in the exponent of equation (3.29) has an extreme if the Euler-Lagrange equation holds:

$$\frac{\partial \mathcal{F}(\tau, q, \dot{q})}{\partial q} - \frac{d}{d\tau}\frac{\partial \mathcal{F}(\tau, q, \dot{q})}{\partial \dot{q}} = 0 \tag{3.31}$$

The solution of equation (3.31) will be denoted by q_c and its most general expression is

$$q_c(t) = A \cdot t + B \tag{3.32}$$

where A and B are determined by the conditions $q(t = 0) = q_0$ and $q(t) = q_t$. Now we try to evaluate the Wiener integral, equation (3.29). Following (66) we write

$$q(\tau) = q_c(\tau) + y(\tau) \qquad y(0) = y(t) = 0 \tag{3.33}$$

Substitution of (3.33) in (3.30) gives after integrating in time:

$$\int_0^t \mathcal{F}(\tau, q, \dot{q})d\tau = A^2 t + \int_0^t \frac{\eta}{2}\dot{y}^2 d\tau \tag{3.34}$$

Now we can express the probability of having the state q_t at time t as

$$p(q_t) = e^{-\beta A^2 t} \int ... \int e^{-\beta \int_0^t \left(\frac{\eta}{2}\dot{y}^2\right)d\tau} \; \mathcal{D}y \tag{3.35}$$

Inserting the solution of the Wiener integral in equation (3.35) (66; 67):

$$p(q_t) = \sqrt{\frac{\beta\eta}{2\pi t}} e^{-\beta \frac{\eta}{2}\frac{q_t - q_0}{t}} \tag{3.36}$$

Equation (3.36) coincides with the transition probability function for the one-dimensional Brownian motion (64; 65). With a diffusion coefficient given by

$$D = \frac{kT}{2\eta} \tag{3.37}$$

in agreement with Einstein's formula. Einstein relation is obtained by confronting the result of the equation for the time-dependent fluctuation with the result at thermal equilibrium. The approach to Brownian motion describing the dynamics of a particle moving under the influence of very rapidly varying forces (Wiener process) was proposed by Langevin. Those rapidly varying forces are called white noise and model the mechanics of systems in contact wit a heat bath.

In this example the variational theory is in fact equivalent to solve the Langevin equation given that at each time step the system reaches equilibrium.

3.4.3 Example 3: Linear spring-dashpot system

The linear spring-dashpot system is characterized by an energy function and kinetic potential of the form:

$$E(q,t) = \frac{\kappa}{2}q^2 - f(t)q \tag{3.38a}$$

$$\phi(\dot{q}) = \frac{\eta}{2}\dot{q}^2 \tag{3.38b}$$

where $q \in \mathbb{R}$, κ is the spring constant, η is the dashpot viscosity, and $f(t)$ is a time-dependent applied force. For this system, the equilibrium equation (3.1) reduces to

$$\kappa q - f + \eta\dot{q} = 0 \tag{3.39}$$

The corresponding incremental work function for this system is

$$W(q_n, q_{n-1}) = \frac{\kappa}{2}(q_n^2 - q_{n-1}^2) - f_n q_n + f_{n-1}q_{n-1} + \frac{\eta}{2\triangle t}(q_n - q_{n-1})^2 \tag{3.40}$$

and the evaluation of the partition function entails a simple Gaussian integral. Inserting the result in (3.16) yields

$$p(q_n) = \int \dots \int \left(\frac{2\pi}{\beta(\kappa + \eta/\triangle t)} \right)^{-n/2} \exp\left\{ -\beta \sum_{i=0}^{n-1} \frac{\big(\triangle t(f_{i+1} - \kappa q_{i+1}) - \eta(q_{i+1} - q_i)\big)^2}{2\triangle t(\eta + \kappa \triangle t)} \right\} p(q_0)\, dq_{n-1} \dots dq_0 \tag{3.41}$$

In the limit of $\triangle t \to 0$ and $n \to \infty$, with $t = n\triangle t$ fixed, the sum in the exponential of this formula converges to the Riemann integral

$$\mathcal{W}[q] = \int_0^t \frac{1}{2\eta} \big(\kappa q(\tau) - f(\tau) + \eta \dot{q}(\tau)\big)^2 \, dt \tag{3.42}$$

In the same limit, (3.41) may be written as the path integral

$$\mathcal{D}q = \lim_{n\to\infty} \left(\frac{2\pi}{\beta\big(\kappa + \eta/(t/n)\big)} \right)^{-n/2} dq_{n-1} \dots dq_0 \tag{3.43}$$

which is of the anticipated form (3.17). The structure of (3.17) is revealing. Thus, it is observed that the work functional $\mathcal{W}[q]$ integrates in time the square of the equilibrium equation (3.39), reduced to units of power by means of the factor $1/\eta$. Evidently, the path which contributes the most to the path integral is the *critical path*, i.e., the path q_c which minimizes the work functional (3.42). Indeed, in the limit of zero viscosity or zero temperature, the *only* path which contributes to the path integral is the critical path, which in that limit coincides with the deterministic trajectory, i.e., with the solution of (3.39). For finite viscosity and finite temperature, however, all paths contribute to the path integral to varying degrees, the contributions becoming increasingly weaker as the trajectories depart from the critical path. The stationarity of $\mathcal{W}[q]$ yields the Euler-Lagrange equations for the critical path

$$\ddot{q} - \omega^2 q = \frac{\dot{f}}{\eta} - \omega^2 \frac{f}{\kappa} \tag{3.44}$$

where $\omega = \kappa/\eta$ and the solution q_c is subject to the boundary conditions $q_c(0) = q_0$, $q_c(t) = q_t$. It is interesting to note that this equation is of second order in time, whereas the original equilibrium equation (3.39) is of first order. This increase in order makes it possible to enforce boundary

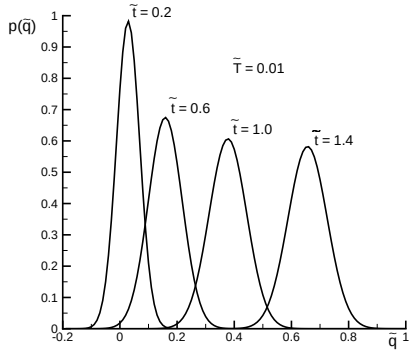

Figure 3.1: Evolution of the probability density for a spring and dashpot system subjected to time-proportional loading.

conditions at times 0 and t, in contrast to the original equation (3.39) which only allows for initial conditions. Furthermore, we note that (3.44) is obtained by *squaring* (3.39), and thus the solutions of the latter are subsumed within the former. However, by virtue of its higher order the Euler-Lagrange equation (3.44) has solutions which do not satisfy (3.39). It thus follows that the critical path does not coincide with the deterministic trajectory in general. Conveniently, the path integral (3.17) can be evaluated exactly in closed form (e.g., (66) and (67)). The result is

$$p(q_t) = \sqrt{\frac{\beta\kappa e^{\omega t}}{2\pi \sinh(\omega t)}} e^{-\beta(\mathcal{W}[q_c])} \tag{3.45}$$

where the critical path $q_c(t)$ is the solution of (3.44). Figure 3.1 shows the evolution of the probability density for a linear loading history $f(t) = At$ in terms of the normalized variables $\tilde{q} = q/(A\eta/\kappa^2)$, $\tilde{t} = t/(\eta/\kappa)$, and $\tilde{T} = T/(A^2\eta^2/k_B\kappa^3)$. The mean value $\langle q(t)\rangle$ traces the critical path $q_c(t)$, which, as noted earlier, differs from the classical path at finite viscosity and temperature. An additional effect of viscosity, which is clearly evident in these figures, is to cause the width of the probability density to broaden in time, with the attendant increase in the uncertainty of the state of the system.

3.4.4 Example 4: Dry friction

The work functional (3.42) appearing in the path integral representation (3.17) is characteristic of systems whose kinetic potential $\phi(\dot{\boldsymbol{q}})$ exhibits quadratic behavior near the origin. However, there are cases of interest which do not fall into that category. A case in point is provided by *dry friction*, which is characterized by a kinetic potential which has a vertex at the origin. Consider, by way of example, a one-dimensional system sliding against a frictional resistance $s > 0$ under the action of an applied force $f(t)$ such that $|f(t)| \leq s$. In this particular case

$$E(q,t) = -f(t)q \tag{3.46a}$$

$$\phi(\dot{q}) = s|\dot{q}| \tag{3.46b}$$

and the incremental work function (3.4) specializes to

$$W(q_n, q_{n-1}) = -f_n q_n + f_{n-1} q_{n-1} + s\,|q_n - q_{n-1}| \tag{3.47}$$

As expected from the rate-independent nature of dry friction, W is independent of $\triangle t$. The corresponding partition function (3.22), transition probability (3.13), and probability density (3.16) take the form:

$$Z(q_{n-1}) = \frac{2s}{\beta(s^2 - f_n^2)} \mathrm{e}^{\beta(f_n - f_{n-1})\, q_{n-1}} \tag{3.48}$$

$$p(q_n|q_{n-1}) = \frac{\beta(s^2 - f_{n-1}^2)}{2s} \mathrm{e}^{-\beta(s\,|q_n - q_{n-1}| - f_n(q_n - q_{n-1}))} \tag{3.49}$$

and

$$\begin{aligned} p(q_n) = & \int \cdots \int \prod_{i=0}^{n-1} \frac{\beta(s^2 - f_i^2)}{2s} \\ & \exp\left\{ -\beta \sum_{i=0}^{n-1} \left(s\,|q_{i+1} - q_i| - f_{i+1}(q_{i+1} - q_i) \right) \right\} \\ & p(q_0)\, dq_{n-1} \ldots dq_0 \end{aligned} \tag{3.50}$$

respectively. An important feature of the transition probability (3.49) is that it depends solely on the difference $q_n - q_{n-1}$. Therefore, the chain q_0, q_1, ..., q_n defines a random walk, and the

probability $p(q_t|q_0)$ corresponding to the limit of $\triangle t \to 0$ and $n \to \infty$ at constant $t = n\triangle t$ follows by an application of the central limit theorem. The result is

$$p(q_t|q_0) = \frac{1}{\sqrt{2\pi}\sigma(t)} \mathrm{e}^{-\left(q_t - \langle q \rangle(t)\right)^2 / 2\sigma^2(t)} \tag{3.51}$$

where

$$\langle q \rangle(t) = q_0 + \sum_{i=0}^{n-1} \frac{2f_i}{\beta(s^2 - f_i^2)} \tag{3.52}$$

is the mean path traced by the system, and

$$\sigma^2(t) = \sum_{i=0}^{n-1} \frac{2(s^2 + f_i^2)}{\beta^2(s - f_i)^2(s + f_i)^2} \tag{3.53}$$

measures the deviation from the mean path. It is interesting to note that, in the limit of zero temperature, $\langle q \rangle(t) = q_0$ for as long as $|f(t)| < s$, with the system sliding off to $\pm\infty$ instantaneously as soon as f reaches $\pm s$. By way of sharp contrast, at finite temperature the system undergoes sliding even when the applied force $f(t)$ remains strictly below s in magnitude at all times. In addition, the standard deviation σ from the mean path is predicted to be proportional to temperature. By way of illustration of this behavior, the trajectories of the system corresponding to applied cyclic loads of the form $f(t) = A\sin(\omega t)$ are shown in Figure 3.2 in terms of the normalized variables: $\bar{q} = q/(k_B T/s)$, $\bar{f} = f/s$, and $\bar{t} = \omega t$. The ability of the theory to allow for *hysteresis* and to predict its temperature dependence is particularly noteworthy. As expected, the response of the system is predicted to soften with increasing temperature, in keeping with numerical simulations of magnetic systems (68).

3.5 Path integral Monte Carlo (PIMC)

Metropolis Monte Carlo algorithms have been used in statistical mechanics as well as in quantum mechanic (69; 70; 71). In this section we develop a Metropolis Monte Carlo algorithm to study the evolution of the phase field model of dislocations developed in Chapter 2. The probability of having the system in a state $\boldsymbol{\xi}^{n+1}$ at time $n+1$ is given by

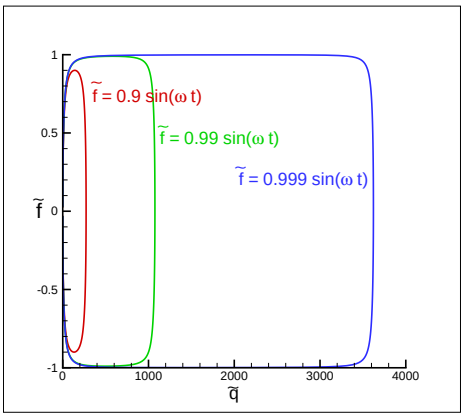

Figure 3.2: Trajectories of a system sliding under the action of an applied cyclic load $f(t) = A\sin(\omega t)$ against a frictional resistance s.

$$p(\boldsymbol{\xi}^{n+1}) \quad = \quad \int ... \int \left\{ \prod_{i=0}^{n} \frac{1}{Z(\boldsymbol{\xi}^i)} \right\} e^{-\beta \mathcal{W}(\boldsymbol{\xi}^0,...,\boldsymbol{\xi}^{n+1})} p(\boldsymbol{\xi}^0) d\boldsymbol{\xi}^0 ... d\boldsymbol{\xi}^n \tag{3.54}$$

where $\mathcal{W}(\boldsymbol{\xi}^0,...,\boldsymbol{\xi}^{n+1}) = \sum_{i=0}^{n} W(\boldsymbol{\xi}^i, \boldsymbol{\xi}^{i+1})$ and $\boldsymbol{\xi}^i$ is the value of the phase field in the slip plane at time $t = t_i$

It is appropriate to apply a Metropolis algorithm with the probability distribution $e^{-\beta \mathcal{W}(\xi_0,...,\xi_{n+1})}$. The procedure is described here. First we choose an initial path $\Xi^{(0)}$ which is a sequence of randomly chosen states $\boldsymbol{\xi}^0$, $\boldsymbol{\xi}^1$, ..., $\boldsymbol{\xi}^{n+1}$. A new path Ξ' is generated varying only one selected random state $\boldsymbol{\xi}^k$. Now we can compute the energy variation on the energy between the two paths

$$\Delta E = E(\Xi) - E(\Xi') \tag{3.55}$$

If the energy is lowered, we take $\Xi^{(1)} = \Xi'$. Otherwise we let $\Xi^{(1)} = \Xi$ with probability $e^{-\beta \Delta E}$. Next $\Xi^{(2)}$ is obtained in the same manner from $\Xi^{(1)}$. The system evolves toward the paths that make the most important contribution to the path integral.

We proceed to illustrate temperature effects in the phase-field model of dislocations described in Chapter 2. We consider a single slip system containing a fixed concentration of point obstacles of uniform strength and deforming under the action of a cyclic loading shear stress. Here the

incremental work function is given by

$$W[\xi^{n+1}|\xi^n] = E[\xi^{n+1}] - E[\xi^n] + \int f(\boldsymbol{x})|\xi^{n+1}(\boldsymbol{x}) - \xi^n(\boldsymbol{x})|d^2x \tag{3.56}$$

and

$$E[\xi] = \frac{1}{(2\pi)^2}\int\left(\frac{\mu b^2}{4}\frac{K}{1+Kd/2}|\hat{\xi}|^2 - \frac{b\hat{s}\hat{\xi}}{1+Kd/2}\right)d^2k \tag{3.57}$$

All calculations are carried out on a 100×100-point grid with periodic boundary conditions. The energy (3.57) is computed in Fourier transformed space. For simplicity, we assume all obstacles to have a uniform strength $f = 10\mu b$ and the concentration is $cb^2 = 0.01$. Given that the system at time t^{n+1} depends only on the system at time t^n the evolution is modeled as follows. Using a Metropolis Monte Carlo algorithm at time t^n the system evolves until it reaches thermal equilibrium, the procedure is repeated for the following time step.

3.5.1 Results

Figure 3.3 shows the computed stress-strain curve and dislocation density evolution during cyclic loading at different temperatures. For a given temperature there are two differentiated regimes (Figure 3.3 a). The first regime of 'microslip' is dominated by dislocation bow-out; and the second is characterized by generalized yielding. The onset of yielding is temperature dependent and the material is softer at higher temperatures in agreement with experimental observation and results obtained by other computational methods in single crystals (29; 30; 31). It should be carefully noted that, owing to the frictional sliding of the dislocations over the obstacles that occurs during the loading state, the interaction forces between the dislocations and the obstacles do not vanish when the applied shear stress is reduced to zero. Instead, the system is left in a state of permanent or residual deformation in which the dislocation/obstacle force system is self-equilibrated.

The process of slip is accompanied by a steady increase in the dislocation line density, Figure 3.3 b. The temperature effect here is that even for zero applied shear stress the dislocation density is not null (except initially for the case of zero temperature).

The evolution of the dislocation density during a loading cycle is of considerable interest as well, Figure 3.3 b. Thus, upon unloading the dislocation density decreases as a result of the elastic relaxation of the dislocation lines. The dislocation density bottoms out—but does not vanish

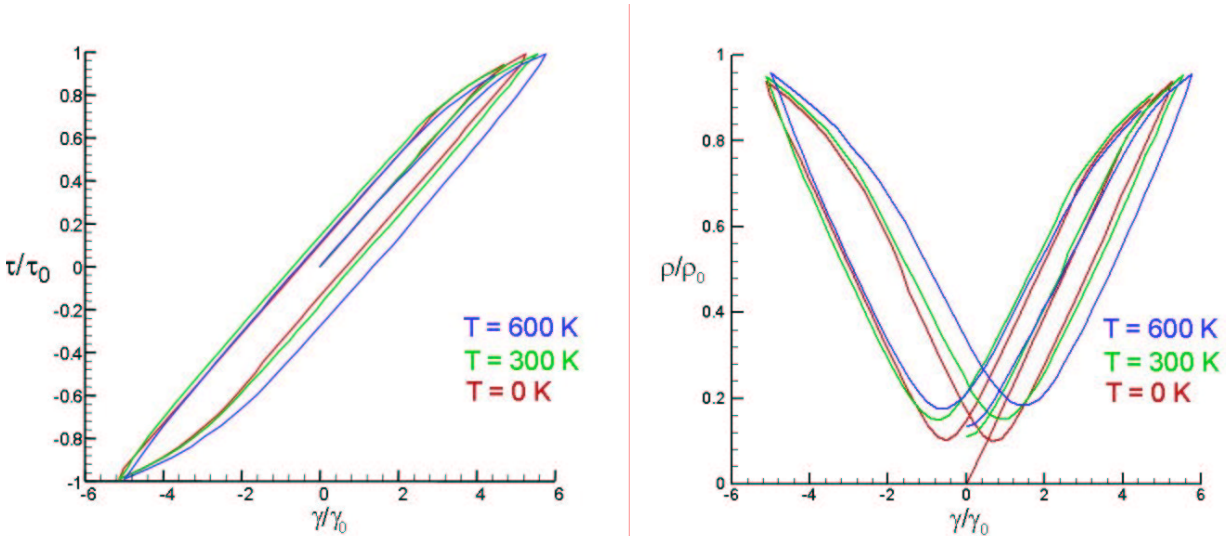

(a) Applied shear stress vs. slip strain

(b) Dislocation density vs. slip strain

Figure 3.3: Effect of temperature during cyclic loading.

entirely—upon the removal of the applied stress. The dislocation density increases again during reverse loading, giving rise to a dislocation density *vs.* slip strain curve in the form of a 'butterfly'. This type of behavior is indeed observed experimentally (57). It also arises in models of the stored energy of cold work (58), and is in analogy to the hysteretic loops exhibited by magnetic systems (72; 68) and in random-field Ising model at zero temperature (53).

Figure 3.4 shows the effect of the temperature on the dislocation geometry for an applied shear stress $\tau/\tau_0 = 0.99$. As the temperature is increased, more obstacles can be overcome. Thus, dislocation density and slip increase for increasing temperature at the same applied shear stress.

3.6 Mean field approximation of the phase-field dislocation theory

The mean field approximation provides a convenient framework to illustrate the influence of temperature, obstacle density and strain rate during cyclic loading in the phase field model of dislocations.

In section 3.6.1 we express the energy in terms of the value of the phase field only at the obstacles, for a periodic arrangement of obstacles. In section 3.6.3 we compare the mean field approximation with the full model and experimental results.

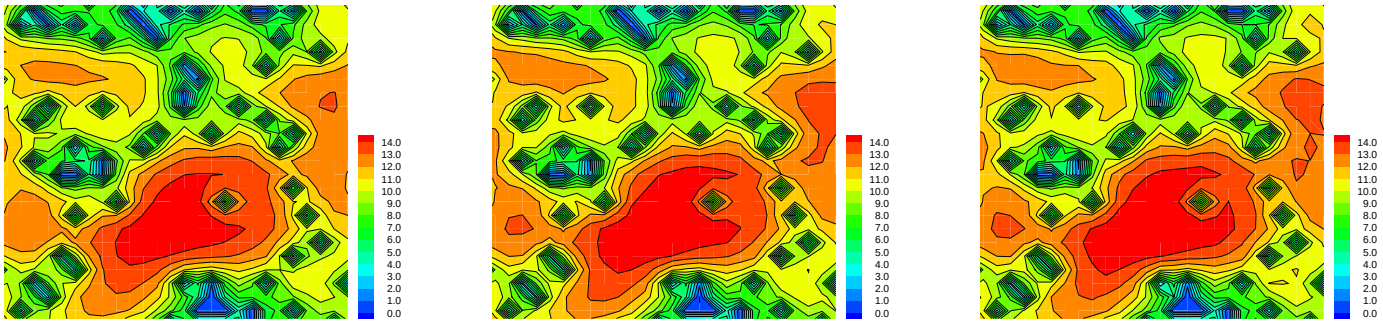

(a) $T = 0K$ (b) $T = 300K$ (c) $T = 600$

Figure 3.4: Effect of temperature on dislocation patterns.

3.6.1 Dislocation energies

We start by reducing the system to a periodic lattice $\mathcal{L}$ of N sites. The energy of the phase field dislocation model is then

$$E = \sum_{i \in \mathcal{L}} \sum_{j \in \mathcal{L}} \frac{1}{2} H_{ij} \xi_i \xi_j - s \sum_{i \in \mathcal{L}} \xi_i \tag{3.58}$$

where $H_{ij} = H_{ji}$ represents the dislocation interaction, s is the applied stress and $\xi_i = \xi(\boldsymbol{x}_i)$. We decompose the quadratic part of the Hamiltonian as

$$E = \sum_{i \in \mathcal{L}-\mathcal{O}} \sum_{j \in \mathcal{L}-\mathcal{O}} \frac{1}{2} A_{ij} \xi_i \xi_j + \sum_{i \in \mathcal{L}-\mathcal{O}} \sum_{j \in \mathcal{O}} \frac{1}{2} B_{ij} \xi_i \xi_j + \sum_{i \in \mathcal{O}} \sum_{j \in \mathcal{O}} \frac{1}{2} C_{ij} \xi_i \xi_j - s \sum_{i \in \mathcal{L}} \xi_i \tag{3.59}$$

where $\mathcal{O}$ is the subset of $\mathcal{L}$ occupied by obstacles. To compute the partition function we split the integral with respect to the degrees of freedom in $\mathcal{L} - \mathcal{O}$ and in $\mathcal{O}$

$$Z = \int e^{-\beta E} \prod_{i \in \mathcal{L}-\mathcal{O}} d\xi_i \prod_{j \in \mathcal{O}} d\xi_j \tag{3.60}$$

The first integral gives

$$e^{-\beta E} \prod_{i \in \mathcal{L}-\mathcal{O}} d\xi_i = \frac{1}{\sqrt{det(\beta \boldsymbol{A}/2\pi)}} exp \left\{ -\beta \left(\sum_{i \in \mathcal{O}} \sum_{j \in \mathcal{O}} \frac{1}{2} G_{ij}^{-1} \xi_i \xi_j - \sum_{i \in \mathcal{O}} \tau_i \xi_i + h_0 \right) \right\} \tag{3.61}$$

where

$$G_{ij}^{-1} = C_{ij} - \frac{1}{8} \sum_{k \in \mathcal{L}-\mathcal{O}} \sum_{l \in \mathcal{L}-\mathcal{O}} A_{kl}^{-1} B_{ki} B_{lj} \tag{3.62}$$

$$\tau_i = s_i - \frac{1}{4} \sum_{k \in \mathcal{L}-\mathcal{O}} \sum_{l \in \mathcal{L}-\mathcal{O}} s_l A_{kl}^{-1} B_{ki} \tag{3.63}$$

$$h_0 = -\frac{1}{4} \sum_{k \in \mathcal{L}-\mathcal{O}} \sum_{l \in \mathcal{L}-\mathcal{O}} s_l A_{kl}^{-1} s_k \tag{3.64}$$

The degrees of freedom in $\mathcal{L} - \mathcal{O}$ can be integrated exactly and the partition function can be written as

$$Z = \frac{1}{\sqrt{det(\beta \boldsymbol{A}/2\pi)}} \int e^{-\beta E'} \prod_{j \in \mathcal{O}} d\xi_j \tag{3.65}$$

with

$$E' = \sum_{i \in \mathcal{O}} \sum_{j \in \mathcal{O}} \frac{1}{2} G_{ij}^{-1} \xi_i \xi_j - \sum_{i \in \mathcal{O}} \tau_i \xi_i + h_0 \tag{3.66}$$

In order to obtain explicit expressions for the coefficients in the reduced energy (3.66) we solve the following equivalent problem. Assuming that ξ is constrained to take the value ξ_j at the obstacle site x_j, then the problem is

$$\inf \frac{1}{(2\pi)^2} \int \frac{\mu b^2}{4} \frac{K}{1 + Kd/2} |\hat{\xi}|^2 d^2k - b \int s\xi d^2x \tag{3.67a}$$

$$\text{subject to: } \frac{1}{(2\pi)^2} \int \mathrm{e}^{i\boldsymbol{k}\cdot\boldsymbol{x}_j} \hat{\xi} d^2k = \xi_j \tag{3.67b}$$

With the introduction of Lagrange multipliers the problem becomes

$$\sup_{\lambda_1,\ldots,\lambda_n} \inf_{\xi} \left\{ \frac{1}{(2\pi)^2} \int \frac{\mu b^2}{4} \frac{K}{1+Kd/2} |\hat{\xi}|^2 d^2k - b \int \hat{s}^* \hat{\xi} - \sum_{j=1}^{n} \lambda_j \left(\frac{1}{(2\pi)^2} \int \mathrm{e}^{i\boldsymbol{k}\cdot\boldsymbol{x}_j} \hat{\xi} d^2k - \xi_j \right) \right\} \quad (3.68)$$

The solution for $\hat{\xi}$ is

$$\hat{\xi} = \frac{2}{\mu b^2} \left(\frac{1+Kd/2}{K} \right) \sum_{j=1}^{n} \lambda_j \mathrm{e}^{-i\boldsymbol{k}\cdot\boldsymbol{x}_j} + \frac{2}{\mu b} \frac{\hat{s}}{K} \quad (3.69)$$

Introducing the solution into the constraint we obtain

$$\sum_{j=1}^{n} G_{ij} \lambda_j + s'_i = \xi_i \quad (3.70)$$

where

$$G_{ij} = \int \frac{2}{\mu b^2} \left(\frac{1+Kd/2}{K} \right) \mathrm{e}^{i\boldsymbol{k}\cdot(\boldsymbol{x}_i - \boldsymbol{x}_j)} \frac{d^2k}{(2\pi)^2} = G(\boldsymbol{x}_i - \boldsymbol{x}_j) \quad (3.71)$$

and

$$s'_i = \int \frac{2}{\mu b} \frac{\hat{s}}{K} \mathrm{e}^{i\boldsymbol{k}\cdot\boldsymbol{x}_i} \frac{d^2k}{(2\pi)^2} \quad (3.72)$$

The corresponding reduced energy is

$$E'(\xi_1, \ldots, \xi_n) = \sum_{i=1}^{n} \sum_{j=1}^{n} \frac{1}{2} G^{-1}_{ij} \xi_i \xi_j - \sum_{i=1}^{n} \tau_i \xi_i + h_0 \quad (3.73)$$

where

$$\tau_i = \sum_{j=1}^{n} G^{-1}_{ij} s'_i \quad (3.74)$$

and

$$h_0 = \frac{1}{2} \sum_{i=1}^{n} \sum_{j=1}^{n} G^{-1}_{ij} s'_i s'_j - \int \frac{|\hat{s}|^2}{\mu K (1+Kd/2)} \frac{d^2k}{(2\pi)^2} \quad (3.75)$$

In order to compute the coefficients G^{-1}_{ij} and τ_i in the energy we assume that the obstacles are arranged periodically in a grid at a distance r as shown in Figure 3.5. In this grid we define the reciprocal vectors $\boldsymbol{v}$ such that $v \in [-\pi/r, \pi/r]$. Equation (3.70) can be rewritten as

$$\xi(\boldsymbol{l}) = s'(\boldsymbol{l}) + \sum_{\boldsymbol{l}'} G(\boldsymbol{l} - \boldsymbol{l}') \lambda(\boldsymbol{l}') \quad (3.76)$$

where $\boldsymbol{l}$ and $\boldsymbol{l}'$ represent the coordinates of the obstacle sites. We define the discrete Fourier transform as follows:

$$\hat{\xi}(\boldsymbol{v}) = r^2 \sum_{\boldsymbol{l}} \xi(\boldsymbol{l}) e^{-i\boldsymbol{v}\boldsymbol{l}} \tag{3.77}$$

$$\hat{G}(\boldsymbol{v}) = r^2 \sum_{\boldsymbol{l}} G(\boldsymbol{l}) e^{-i\boldsymbol{v}\boldsymbol{l}} \tag{3.78}$$

$$\hat{\lambda}(\boldsymbol{v}) = r^2 \sum_{\boldsymbol{l}} \lambda(\boldsymbol{l}) e^{-i\boldsymbol{v}\boldsymbol{l}} \tag{3.79}$$

$$\hat{s'}(\boldsymbol{v}) = r^2 \sum_{\boldsymbol{l}} s'(\boldsymbol{l}) e^{-i\boldsymbol{v}\boldsymbol{l}} \tag{3.80}$$

From Equation (3.76) and the convolution theorem, we obtain

$$\hat{\xi}(\boldsymbol{v}) = \hat{s}(\boldsymbol{v}) + \frac{\hat{G}(\boldsymbol{v})\hat{\lambda}(\boldsymbol{v})}{r^2} \tag{3.81}$$

Equation (3.70) can be expressed as

$$\lambda_j = G_{ij}^{-1} \left(\xi_i - s_i\right) \tag{3.82}$$

Proceeding as before we obtain

$$\hat{\lambda}(\boldsymbol{v}) r^2 = \widehat{G^{-1}}(\boldsymbol{v}) \left(\hat{\xi}(\boldsymbol{v}) - \hat{s}(\boldsymbol{v})\right) \tag{3.83}$$

Combining Equations (3.84) and (3.83) we obtain

$$\frac{r^4}{\hat{G}(\boldsymbol{v})} = \widehat{G^{-1}}(\boldsymbol{v}) \tag{3.84}$$

Now we have an explicit expression for G_{ij}^{-1} from equations (3.71) and (3.84)

$$G_{ij}^{-1} = \frac{\mu b^2 r^4}{2} \int \frac{K}{1 + Kd/2} e^{i\boldsymbol{v}(\boldsymbol{l}_i - \boldsymbol{l}_j)} \frac{d^2 v}{(2\pi)^2} \tag{3.85}$$

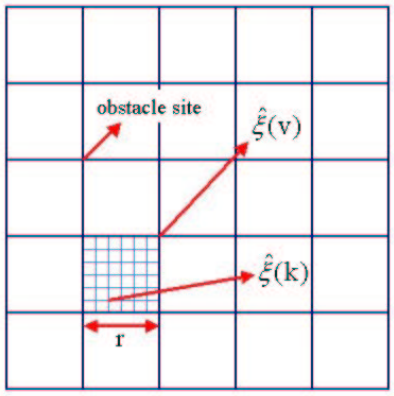

Figure 3.5: Grid of obstacles.

Following the same steps we can compute τ_j and h_0

$$\tau_j = br^2 \int \frac{\hat{s}}{1 + Kd/2} e^{i\boldsymbol{v}\boldsymbol{l}_j} \frac{d^2v}{(2\pi)^2} \tag{3.86}$$

$$h_0 = \int_{\mathcal{B}} \frac{|\hat{s}|^2}{\mu K(1 + Kd/2)} \frac{d^2v}{(2\pi)^2} - \int_{\mathcal{L}} \frac{|\hat{s}|^2}{\mu K(1 + Kd/2)} \frac{d^2k}{(2\pi)^2} \tag{3.87}$$

Therefore, the mechanics of the system is described by the value of the phase-field at the point obstacles as it was done for zero temperature in Chapter 2.

3.6.2 A variational derivation of the mean field

In this section we derive the mean field approximation of the phase field model of dislocations by introducing thermodynamic perturbation theory and a variational principle. With this model we obtain the optimum free energy that can be constructed with a mean field model in which the values of the phase field at each obstacle point are assumed uncorrelated.

The incremental work function can be written using Equations (3.56) and (3.57) as

$$W[\boldsymbol{\xi}^{n+1}|\boldsymbol{\xi}^n] = E[\boldsymbol{\xi}^{n+1}] - E[\boldsymbol{\xi}^n] + f\sum_i |\xi_i^{n+1} - \xi_i^n| \tag{3.88}$$

where the sum in i is over the obstacles. Now we break up the work function into two parts:

$$W = W_1 + W_0 \tag{3.89}$$

where

$$W_0 = \tau^n \sum_i \xi_i^n - \hat{\tau}^{n+1} \sum_i \xi_i^{n+1} + f\sum_i |\xi_i^{n+1} - \xi_i^n| + h_0^{n+1} - h_0^n \tag{3.90}$$

where $\hat{\tau}$ is an effective external applied stress. The system described by W_0 is a model with independent values of the phase field at each lattice site and each value fluctuates under the influence of a mean field. This model presents the same simple problem solved in Section 3.4 and we can obtain the free energy of the system governed by the incremental work function W_0

$$F_0 = -\frac{1}{\beta N_{obs}} \log Z_0 \tag{3.91}$$

$$= -(\hat{\tau}^{n+1} - \tau^n)\langle \xi_i^n \rangle_0 - \frac{1}{\beta} \log \frac{2f}{\beta(f^2 - (\hat{\tau}^{n+1})^2)} + h_0^{n+1} - h_0^n \tag{3.92}$$

In order to obtain the best approximation of the full free energy of the system we use Bogoliunov inequality (73; 74) in equation (3.89):

$$F \leq F_0 + \langle W_1 \rangle_0 \tag{3.93}$$

where

$$\langle W_1 \rangle_0 = \frac{G}{2}(\langle (\xi^{n+1})^2 \rangle_0 - \langle \xi^{n+1} \rangle_0^2) - \frac{G}{2}(\langle (\xi^n)^2 \rangle_0 - \langle \xi^n \rangle_0^2) - (\tau^{n+1} - \hat{\tau}^{n+1})\langle \xi^{n+1} \rangle_0 \tag{3.94}$$

represents the thermal average of W_1 with respect to W_0. In the last equation,

$$G = \frac{1}{N_{obs}} \sum_i G_{ii} \tag{3.95}$$

$$\langle \xi^{n+1} \rangle_0 = \frac{\partial F_0}{\partial \hat{\tau}^{n+1}} \tag{3.96}$$

$$= \langle \xi^n \rangle_0 + \frac{2\hat{\tau}^{n+1}}{\beta(f^2 - (\hat{\tau}^{n+1})^2)} \tag{3.97}$$

$$\langle (\xi^{n+1})^2 \rangle_0 = -\frac{1}{\beta} \frac{\partial^2 F_0}{\partial (\hat{\tau}^{n+1})^2} + \langle \xi^{n+1} \rangle_0^2 \tag{3.98}$$

and we use the fact that

$$\sum_{ij} G_{ij} = 0 \tag{3.99}$$

The strategy for using equation (3.93) is as follows. We define a trial work function W_0 with an effective external applied stress $\hat{\tau}$. Varying the value of $\hat{\tau}$ in such a way to minimize

$$F_{var} \equiv F_0(\hat{\tau}) + \langle W_1(\hat{\tau}) \rangle_0 \tag{3.100}$$

for each time step, we shall obtain the best approximation of the full free energy with W_0. To find the minimum, we differentiate with respect to $\hat{\tau}^{n+1}$ and set the result equal to zero

$$\frac{\partial F_{var}}{\partial \hat{\tau}^{n+1}} = 0 \tag{3.101}$$

The values of $\hat{\tau}^{n+1}$ that satisfy (3.101) are the solution of

$$\frac{G}{\beta^2} \left(\frac{1}{(f - (\hat{\tau}^{n+1}))^3} - \frac{1}{(f + (\hat{\tau}^{n+1}))^3} \right) - (\tau^{n+1} - \hat{\tau}^{n+1}) \frac{\partial \langle \xi^{n+1} \rangle_0}{\partial \hat{\tau}^{n+1}} = 0 \tag{3.102}$$

We were not able to find an analytical expression for $\hat{\tau}$, Figure 3.6 shows the behavior of the effective stress for a sinusoidal external applied stress $\tau = \tau_0 \sin(\omega t)$ and an obstacle concentration $cb^2 = 10^{-4}$ at temperature $T = 300K$.

3.6.3 Results

By differentiating the free energy with respect to the applied stress s, we obtain the total slip in the glide plane:

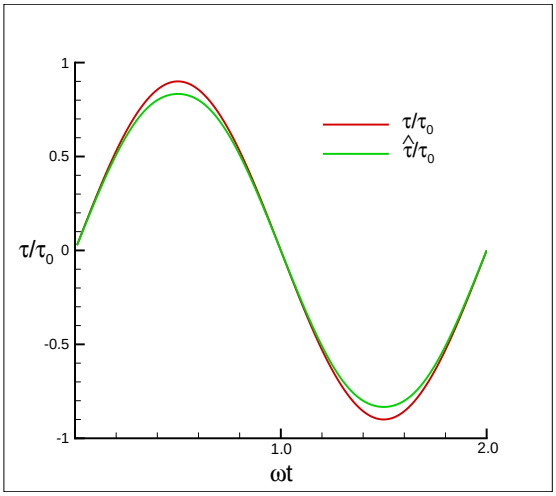

Figure 3.6: Applied stress and effective stress.

$$\gamma^{n+1} = -\frac{\partial F}{\partial s^{n+1}} \tag{3.103}$$

$$= -\frac{\partial \langle W_1 \rangle_0}{\partial \tau^{n+1}} \frac{\partial \tau^{n+1}}{\partial s^{n+1}} - \frac{\partial h_0^{n+1}}{\partial s^{n+1}} \tag{3.104}$$

The last term depends linearly in the applied stress s and represents the elastic response of the crystal. The first term is the mean value of the phase field in the obstacles and contributes to the hysteretic part of the deformation. Figure 3.7 shows the effect of obstacle concentration on the hardening of the system for cyclic loading. In terms of the normalized variables τ/τ_0 the curves seem independent of the obstacle concentration c, but $\tau_0 = fc$, thus as observed in Chapter 2 the saturation stress scales in direct proportion to the obstacle density . Studies of plastic deformation of dilute alloys of f.c.c. structure (Cu-Ni) show that for a range of concentrations $c \geq 2\,at.\,\%$ the flow stress is proportional to c in agreement with the present model (1).

The curves of the flow stress plotted against temperature shown in Figure 3.8 show the characteristics of a steep rise in flow stress at low temperatures, the negative slope is reduced as the temperature increases. This type of behavior is observed in experiments in polycrystalline materials and also in single crystals (1; 75).

Figure 3.8 a shows the computed flow stress vs. temperature for different obstacle concentra-

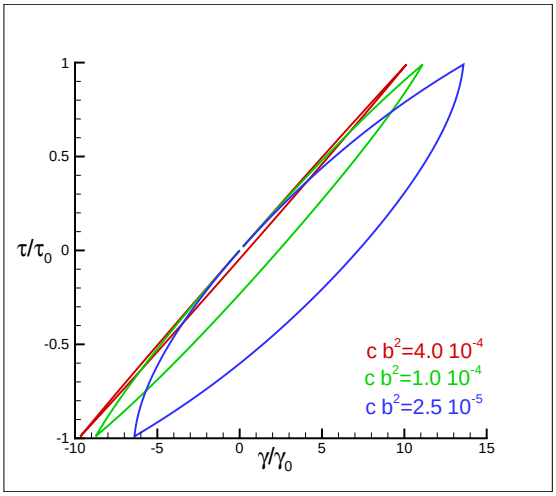

Figure 3.7: Effect of obstacle concentration on the hardening of the system.

tions. The behavior of the flow stress is in agreement with experimental observation for Cu-Ni alloys (Figure 3.8 b). Suzuki developed a theory for an arrangement of dislocations and solute atoms under an external stress (1) . Suzuki's theory is applicable under the following hypothesis: (1) the processes are quasistatic and do not involve dynamical aspects; (2) the frictional forces are neither extremely large nor small. If the frictional forces are very small the hypothesis (1) does not hold any more. Under these considerations the yield stress is given by the following equation:

$$\tau_c = \tau_p + \tau_p \left(1 - \frac{T}{T_c}\right) \tag{3.105}$$

Here τ_p depends on the concentration of obstacles and $T_c \sim 200\,K$ is a critical temperature. For $T \geq T_c$, $\tau_c = \tau_p$ which forms the plateau regions observed in Figures 3.8 a and 3.8 b. Furthermore, $\tau_c = 2\tau_p = \tau_0$ at $T = 0$ and the concentration dependence on τ_c is the same as τ_0.

In the following we analyze the effect of the strain rate in the system. There is no timescale involved in the incremental work function (3.88), but in order to satisfy the hypothesis of our model the system should be allowed to relax at each time step, we call this relaxation time t_r. The parameter that drives the strain rate is the increment in the applied stress for each time step. Therefore, the strain rate is measured in units of t_r and that defines the normalized strain rate $\dot{\gamma}/\dot{\gamma}_0$.

Figure 3.9 shows experimental stress-strain curves for $Al - 5.5at.\%Mg$ alloy at different tem-

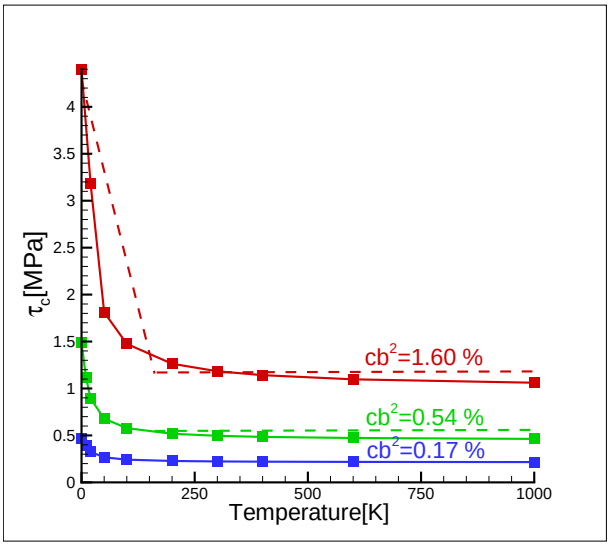

(a) Mean field approximation.

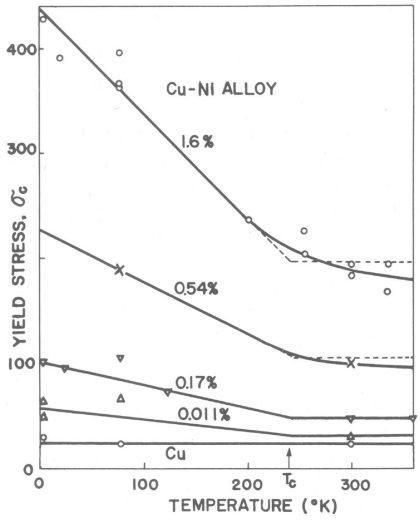

(b) Experimental results for Cu-Ni alloy(1) .

Figure 3.8: Flow stress plotted against temperature.

peratures and strain rates. Figure 3.10 shows the same curves obtained with the mean field approximation. The mean field approximation is in qualitatively good agreement with experimental results.

For applied stresses $|\tau| > \tau_0$ the slip, ξ becomes unbounded. The saturation stress, τ_0 is set by the mean obstacle strength. At zero temperature the normalized slip ξ is computed by direct minimization of (3.88). In this case the solution reduces to $\langle \xi_{n+1} \rangle = \langle \xi_n \rangle$ for $|\tau| < \tau_0$ and it is rate independent.

The relation between strain rate and stress, and its dependence on the temperature can be described by an empirical law of the form (5; 76)

$$\dot{\gamma} = \dot{\gamma}_0 \left(\frac{\tau}{\tau_0} \right)^m e^{-U_0/kT} \tag{3.106}$$

where U_0 is the activation energy and m is the stress exponent. This model is suitable to crystals in which the hardening is primarily due to the interaction of dislocations with point defects (solution hardening).

Figure 3.11 shows the flow stress as a function of temperature and strain rate for the data in

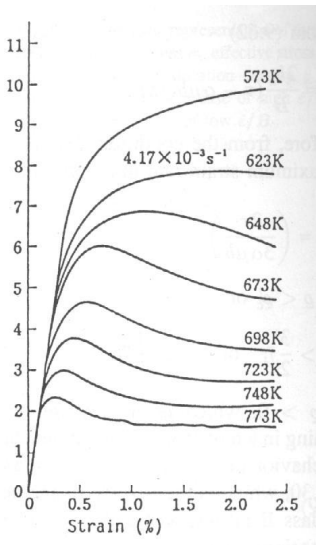

(a) Tensile strain rate of $4.17 \cdot 10^{-3}\, s^{-1}$.

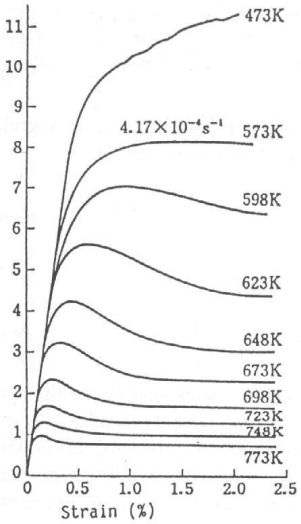

(b) Tensile strain rate of $4.17 \cdot 10^{-4}\, s^{-1}$.

Figure 3.9: Effect of strain rate on stress strain curves in Al-Mg alloy (1).

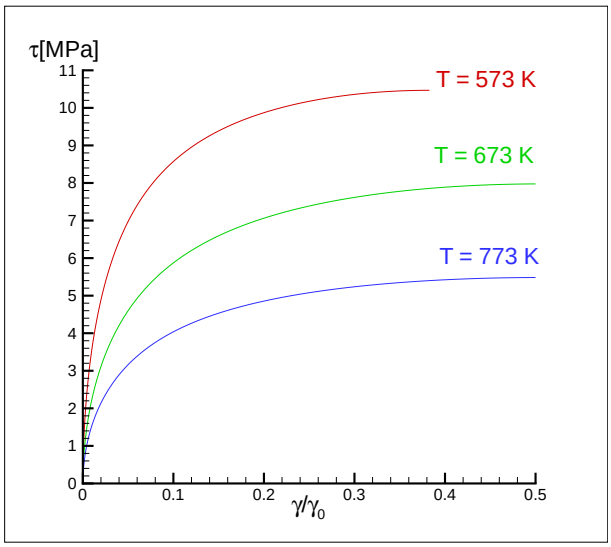

(a) Mean field approximation of stress-strain curves for $\dot{\gamma}/\dot{\gamma}_0 = 10^{-3}\, s^{-1}$.

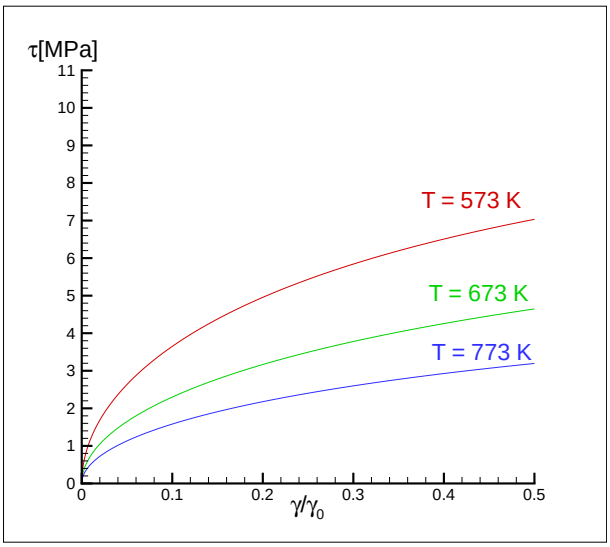

(b) Mean field approximation of stress-strain curves for $\dot{\gamma}/\dot{\gamma}_0 = 10^{-4}\, s^{-1}$.

Figure 3.10: Effect of strain rate on stress strain curves.

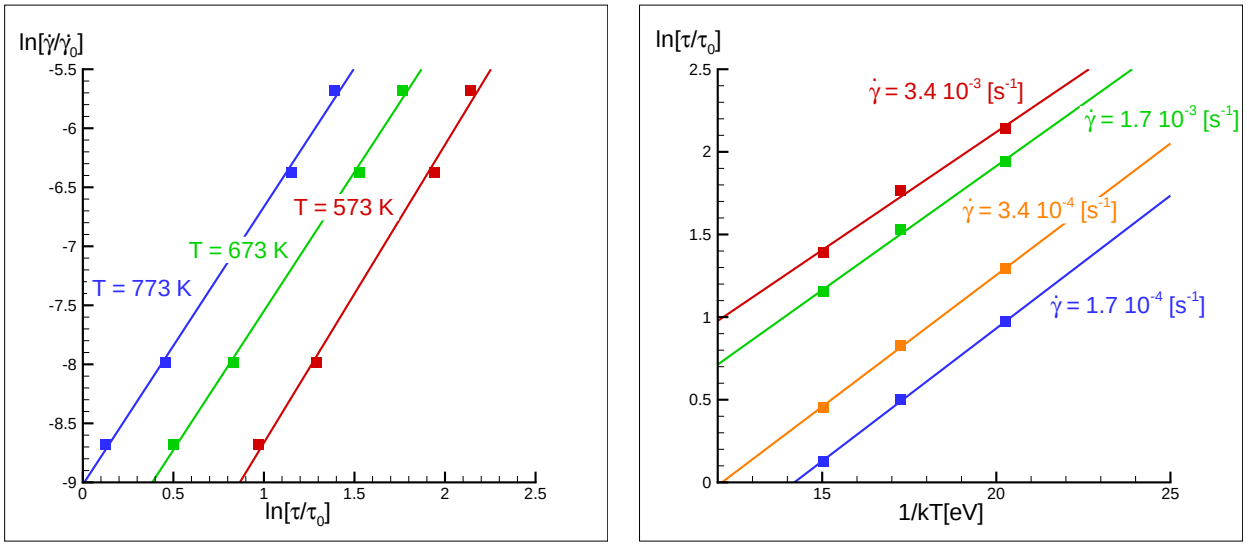

(a) Flow stress *vs. strain rate.*

(b) Temperature *vs. flow stress.*

Figure 3.11: Strain rate and temperature effects in the flow stress.

Figure 3.10. The slope in Figure 3.11 a is the stress exponent, we find $m = 2.5$ which corresponds to values of stress exponents for steady-state creep in alloys (1).

From the slope in Figure 3.11 b we find and activation energy $U_0 = 0.3eV$. It is of interest to compare this value to the theories given by Fleischer and Friedel, and Suzuki (1). The activation energy U_0 can be given in terms of the obstacle resistance as follows:

$$U_0 = f \tag{3.107}$$

for Friedel model,

$$U_0 = \frac{2}{3} f \tag{3.108}$$

for Suzuki model, and

$$U_0 \sim 3f \tag{3.109}$$

for the present model. The periodicity in the spatial arrangement of point obstacles in the mean-field approximation yields the largest U_0.

3.7 Summary and concluding remarks

We have developed a generalization of classical statistical mechanics which describes the behavior of dissipative systems. The ability of the model to allow for hysteresis and to predict its temperature dependence is noteworthy. The behavior obtained with the mean field approximation is in qualitative agreement with the full model and experimental observation. Also in the mean field approximation the plastic part of the slip depends only on the value of the phase field at the obstacle sites and on the temperature, allowing for hysteresis and softening with increasing temperature. Meanwhile the elastic part of the deformation is linear in the applied stress and independent of the temperature.

The glide resistance in the slip plane is not uniform, but has peaks associated with the point obstacles. At absolute zero these barriers cannot be overcome unless the applied stress exceeds the obstacle resistance. But at any temperature above zero, a finite probability exists that the dislocation can penetrate the obstacle. This is indeed predicted with this theory, given that the flow stress depends not only in the obstacle strength and concentration but also in the temperature.

The stress-strain curves show different behavior for different strain rates and temperatures. The system becomes harder with increasing strain rate and decreasing temperature in agreement with experimental observations. Given that at each time step the system reaches equilibrium, strain rate effects in our model are explained as follows. Due to the dissipative character of the system the work supplied to evolve from an equilibrium state with macroscopic slip γ_n to γ_{n+1} increases with the strain rate, therefore the system becomes harder and the flow stress is larger. The strain rate insensitivity at zero temperature can be explained by assuming that the flow stress is controlled by multiplication and mobility due to thermal activation.

Chapter 4

Dislocation structures and crystal boundaries

4.1 Introduction

Direct observation of dislocations and electron microscopy studies have shown that the distribution of dislocations is not random (2; 32; 33). Dislocations rearrange into low energy configurations forming patterns that have the form of dislocation sub-grains. Analytical models (77) and several computer simulation were developed for studying the dislocation patterning phenomena (19; 78; 79; 80). Due to the long-range dislocation-dislocation interaction the investigation of this problem is very difficult, Gulluoglu *et al.* (78) showed that in numerical simulations the interaction cutoff radius strongly influences the formation of dislocation cells. They studied low temperature, stage I deformation, and used no interaction cutoff distance. They found the formation of dislocation walls by relaxation of a system of edge dislocations with a fixed dislocation density.

Dislocation patterns play an important role in the mechanical response of materials. Recently, Bulatov and Cai (81) and Nabarro (82) studied stable dislocation patterns and their influence in the mechanical behavior of materials. Bulatov and Cai showed that dislocations can increase their mobility by zipping together to form junctions. Using atomistic simulations they found that the critical stress to move a network in a $[1, 1, 0]$ plane of bcc molybdenum is 50% smaller than the required to move an isolated dislocation.

In this chapter, we study the formation of dislocation networks in twist boundaries, with different crystal structures and orientations. We use a Metropolis Monte Carlo algorithm in order to find the stable configurations of a stress free grain boundary. It bears emphasis that our results are

independent of the initial configuration chosen (density and location of dislocations). Equilibrium concentration of dislocations are obtained directly as a result of the misfit imposed in the plane of the grain boundary.

4.2 Dislocation models of grain boundaries

The hardening of crystals during plastic deformation is due to the increase in dislocation density, most of the work done in the material is dissipated as heat but a portion is retained in the material as stored energy (cold work). The stored energy can be released if the dislocations rearrange into configurations of lower energy. These configurations are called low-angle boundaries and are represented by arrays of one, two or three sets of dislocations.

Polycrystalline materials are composed of a number of single crystals bounded together. A grain boundary is the interface where two single crystals of different orientation join. In general grain boundaries can be curved but in equilibrium they are planar to minimize the area and therefore the boundary energy.

A considerable amount of energy is released when low-angle boundaries are formed. These processes can occur only when there is sufficient thermal activation to allow long range diffusion of point defects (dislocation climbing). The process is called recovery and occurs when the material is heated at moderate temperatures, i.e., $T \geq 0.3T_m$. (2; 83).

The simplest boundary is the tilt boundary (Figure 4.1), ω defines the rotation between the two crystals and is contained in the boundary. If ω is perpendicular to the boundary, it is called twist boundary (Figure 4.2).

Consider a simple cubic crystal with the boundary in a symmetrical position with respect to the $(1,0,0)$ planes of the two crystals and the rotation axis parallel to $[0,0,1]$, this is a tilt boundary formed by an array of parallel edge dislocations. With a tilt angle θ the separation D between dislocations can be obtained as follows (83; 3). All $(1,0,0)$ planes intersecting the boundary end as an incomplete plane, the number of incomplete planes is

$$n = \frac{2h}{b} \sin \frac{\theta}{2} \tag{4.1}$$

where h is the interplanar distance. Hence, the mean separation between edge dislocations in the

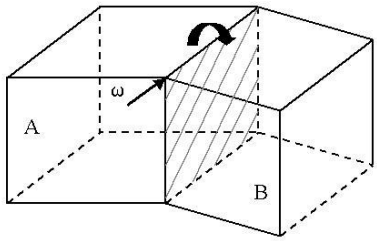

Figure 4.1: A tilt boundary defined by the rotation vector ω.

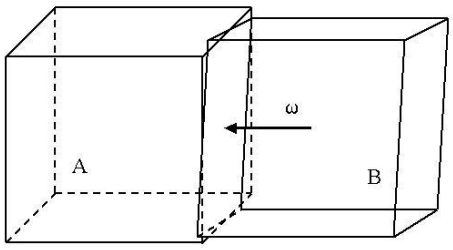

Figure 4.2: A twist boundary, ω is perpendicular to the grain boundary.

boundary is

$$D = \frac{h}{n} \approx \frac{b}{\theta} \tag{4.2}$$

On the other hand, a twist boundary is formed from a grid of pure screw dislocations. The sets of equally spaced dislocations lie in the boundary and the spacing between dislocations in each set is

$$D = \frac{b}{\theta} \tag{4.3}$$

Frank (1950) has derived a relation which may be used to determine the arrangements of dislocations for a general boundary, this relations are derived as follows (83; 3; 33). If we choose a vector $\boldsymbol{V}$ in terms of the crystallographic coordinates of a grain A and next we draw from the same origin a vector $\boldsymbol{V'}$ that has the same crystallographic indexes with respect to a second grain B as shown in Figure 4.3. The failure between the two grains is given by

$$\boldsymbol{B} = \boldsymbol{V} - \boldsymbol{V'} \tag{4.4}$$

$\boldsymbol{B}$ is the resultant Burger vector of all the dislocations cut by $\boldsymbol{V}$, that is

$$\boldsymbol{B} = \sum_i c_i(\boldsymbol{V})\boldsymbol{b}_i \tag{4.5}$$

where c_i is the number of dislocations of Burger vector $\boldsymbol{b}_i$ cut by $\boldsymbol{V}$. Equation (4.5) is valid for any dislocation wall, if this corresponds to a grain boundary, crystal B is rotated with respect to crystal A. In the small-angle approximation

$$\boldsymbol{B} = \boldsymbol{V} \times \boldsymbol{\omega} = \theta(\boldsymbol{V} \times \boldsymbol{a}) \tag{4.6}$$

where $\boldsymbol{a}$ is the unit vector along the axis of rotation. Equations (4.5) and (4.6) constitute Frank's relations for small-angle grain boundaries.

Expressions for the dislocation density can be obtained from Frank's relation by the introduction of the reciprocal vector $\boldsymbol{N}$. For a set of dislocations i,

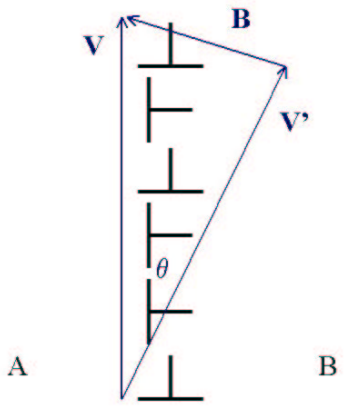

Figure 4.3: Closed failure caused by dislocations in a wall.

$$\boldsymbol{N}_i = \frac{1}{2D_i \sin(\theta/2)}(\boldsymbol{n} \times \boldsymbol{z}_i) \tag{4.7}$$

where $\boldsymbol{n}$ is the normal to the grain boundary and $\boldsymbol{z}_i$ is the sense vector for the dislocation type i. The complete description of a grain boundary is reduced to the determination of $\boldsymbol{N}_i$, $\boldsymbol{n}$ and $\boldsymbol{a}$. In terms of $\boldsymbol{N}_i$,

$$c_i(\boldsymbol{V}) = (\boldsymbol{N}_i \cdot V)2\sin(\theta/2) \tag{4.8}$$

After replacing (4.8) in (4.5) and (4.6),

$$\boldsymbol{V} \times \boldsymbol{a} = \sum_i \boldsymbol{b}_i(\boldsymbol{N}_i \cdot \boldsymbol{V}) \tag{4.9}$$

Only special boundaries can form when only one or two sets of dislocations are introduced into a crystal. Boundaries of both types are described in the following sections.

4.2.1 One set of dislocations

Consider that only one set of dislocations is present, according to (4.9) $\boldsymbol{V} \times \boldsymbol{a}$ must be parallel to the Burger vector $\boldsymbol{b}$, so that $\boldsymbol{b}$ must be perpendicular to both $\boldsymbol{V}$ and $\boldsymbol{a}$. Thus, the boundary plane is perpendicular to $\boldsymbol{b}$ and the rotation axis $\boldsymbol{a}$ is contained in the boundary, the boundary is a tilt

boundary. Since $\boldsymbol{B}$ is zero if $\boldsymbol{V}$ is parallel to $\boldsymbol{z}$, then $\boldsymbol{a}$ is parallel to $\boldsymbol{z}$, hence the dislocations are edge dislocations.

4.2.2 Two sets of dislocations

Consider two sets of dislocations with Burgers vectors $\boldsymbol{b}_1$ and $\boldsymbol{b}_2$, Equation (4.9) becomes

$$\boldsymbol{V} \times \boldsymbol{a} = \boldsymbol{b}_1(\boldsymbol{N}_1 \cdot \boldsymbol{V}) + \boldsymbol{b}_2(\boldsymbol{N}_2 \cdot \boldsymbol{V}) \tag{4.10}$$

Multiplying the last equation by $\boldsymbol{b}_1 \times \boldsymbol{b}_2$:

$$\boldsymbol{V} \cdot [\boldsymbol{a} \times (\boldsymbol{b}_1 \times \boldsymbol{b}_2)] = 0 \tag{4.11}$$

Since $\boldsymbol{V}$ is perpendicular to the normal of the boundary, $\boldsymbol{n}$ is parallel to $\boldsymbol{a} \times (\boldsymbol{b}_1 \times \boldsymbol{b}_2)$. Thus $\boldsymbol{a}$ and $\boldsymbol{b}_1 \times \boldsymbol{b}_2$ lie in the boundary, leading to a tilt boundary.

Another type of boundary that satisfies Equation (4.11) is such that

$$\boldsymbol{a} = \frac{\boldsymbol{b}_1 \times \boldsymbol{b}_2}{|\boldsymbol{b}_1 \times \boldsymbol{b}_2|} \tag{4.12}$$

Replacing (4.12 in (4.11) we get

$$\boldsymbol{V} \times \boldsymbol{a} = \frac{\boldsymbol{b}_1(\boldsymbol{b}_2 \cdot \boldsymbol{V}) - \boldsymbol{b}_2(\boldsymbol{b}_1 \cdot \boldsymbol{V})}{|\boldsymbol{b}_1 \times \boldsymbol{b}_2|} \tag{4.13}$$

For the case:

$$\boldsymbol{n} = \frac{\boldsymbol{b}_1 \times \boldsymbol{b}_2}{|\boldsymbol{b}_1 \times \boldsymbol{b}_2|} \tag{4.14}$$

the boundary is a twist boundary and

$$\boldsymbol{N}_1 = \frac{\boldsymbol{b}_2}{|\boldsymbol{b}_1 \times \boldsymbol{b}_2|} \tag{4.15}$$

$$\boldsymbol{N}_2 = \frac{-\boldsymbol{b}_1}{|\boldsymbol{b}_1 \times \boldsymbol{b}_2|} \tag{4.16}$$

Under these conditions the result is a lozenge-shaped dislocation boundary as the one showed in

Figure 4.4. However this network is not the observed in nature, because crossing dislocation interact and react to form configurations of lower energy as the ones considered in the next section.

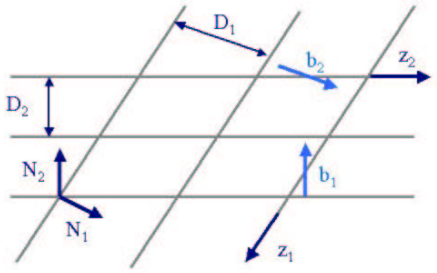

Figure 4.4: A lozenge-shaped dislocation network.

4.3 Direct observation of dislocations

The preceding section treats straight, non-interacting dislocations. These models do not predict true dislocation configurations because dislocation interact and react to form patterns of lower energy. We will now describe two of the patterns observed in twist boundaries (32; 2; 33) that will be simulated using the phase-field model of dislocations.

Square networks

The model for a twist boundary having a $[1,0,0]$ rotation axis and a $(1,0,0)$ contact plane consists of a square grid of screw dislocations with directions $[0,1,1]$ and $[0,1,-1]$ with Burgers vectors:

$$\boldsymbol{b}_1 = \frac{1}{2}[0,1,1] \tag{4.17}$$

$$\boldsymbol{b}_2 = \frac{1}{2}[0,1,-1] \tag{4.18}$$

$$\tag{4.19}$$

An example of a square grid of dislocations is shown in Figure 4.5 for potassium chloride.

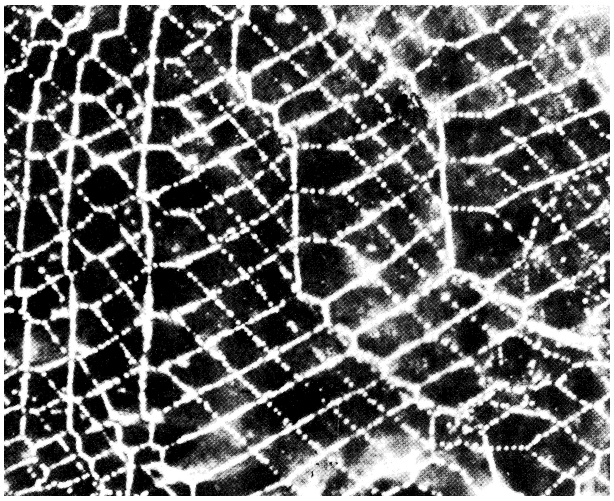

Figure 4.5: Square grid of dislocations in potassium chloride (2).

Hexagonal networks

If the contact plane of the boundary of the boundary is the $(1,1,1)$ plane and the rotation axis is the $[1,1,1]$ the grain boundary consists of a hexagonal grid of screw dislocations with Burgers vectors:

$$\boldsymbol{b}_1 = \frac{1}{2}[-1,1,0] \tag{4.20}$$

$$\boldsymbol{b}_2 = \frac{1}{2}[1,0,-1] \tag{4.21}$$

$$\boldsymbol{b}_3 = \boldsymbol{b}_1 + \boldsymbol{b}_2 \tag{4.22}$$

Figure 4.6 shows a dislocation network in potassium chloride.

4.4 Dislocation interaction

In this section we derive the explicit energy expressions for a general dislocation ensemble in a crystal grain boundary. We will extend the formulation of Chapter 2 to a multiphase field to take

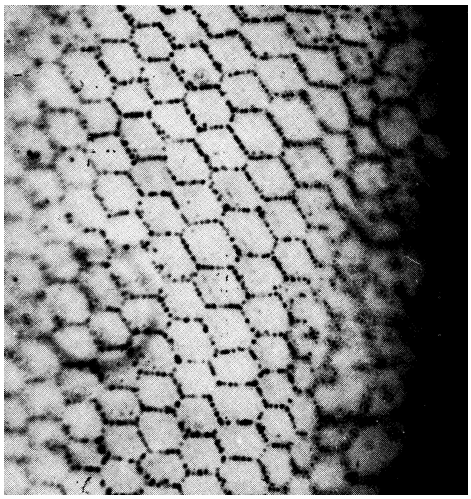

Figure 4.6: Silver-decorated dislocation network in potassium chloride (2).

into account the case where more than one system is active for slip plane.

In order to find the equilibrium configurations, we minimize the energy of the ensemble of dislocations given by the phase-field model described in Chapter 2 with the constraint that the displacement $\boldsymbol{\delta}$ in the crystal boundary is a rotation.

The dislocations are defined by means of a scalar field supported in the plane of the grain boundary (18). Under these conditions, the plastic distortion β_{ij}^{p} has the form:

$$\beta_{ij}^{p} = \sum_{\alpha=1}^{n} \delta_i^{\alpha}\, m_j \delta_S \tag{4.23}$$

where δ_i^{α} is the displacement jump across the plane for each Burgers vector $\boldsymbol{b}_{\alpha}$, $\boldsymbol{m}$ is the unit normal to plane, δ_S is the Dirac distribution supported on the plane S and $\alpha = 1, ..., n$ are the number of active systems.

As in Chapter 2, we can write the elastic interaction of the dislocations as

$$E^{\text{int}} = \frac{1}{(2\pi)^3} \int \frac{1}{2} \hat{A}_{mnuv}(\boldsymbol{k}) \hat{\beta}_{mn}^{p}(\boldsymbol{k}) \hat{\beta}_{uv}^{p*}(\boldsymbol{k}) d^3k \tag{4.24}$$

Replacing Equation (4.23) in (4.24) the interaction energy simplifies to

$$E^{int} = \frac{1}{(2\pi)^2} \int \frac{\mu b^2}{2} \hat{\boldsymbol{\zeta}}^T \cdot \boldsymbol{K} \cdot \hat{\boldsymbol{\zeta}} d^2k \tag{4.25}$$

where the components of $\boldsymbol{\zeta}$ are normalized slip functions such that $\delta_i^\alpha = \zeta_\alpha b_i^\alpha$, $b = |b^\alpha|$ and the components of $\boldsymbol{K}$ are

$$K_{\alpha\beta} = \frac{1}{\mu b^2} \int \hat{A}_{ijkl} b_i^\alpha m_j b_k^\beta m_l dk_3 \tag{4.26}$$

and we have assumed that the plane of the grain boundary is perpendicular to x_3

The interplanar potential $\phi(\boldsymbol{\delta})$ is identified with the energy per unit area that results when two semi-infinite crystals are taken through a relative rigid displacement $\boldsymbol{\delta}$. In this model the interplanar potential is taken to be of the form (7; 18)

$$\phi(\boldsymbol{\delta}^\alpha) = \min_{\xi \in \mathbb{Z}} \frac{1}{2} c_{jl} (\delta_j^\alpha - \xi^\alpha b_j^\alpha)(\delta_l^\alpha - \xi^\alpha b_l^\alpha) \tag{4.27}$$

where

$$c_{jl} = \frac{1}{\mu d} c_{ijkl} m_i m_k \tag{4.28}$$

Inserting (4.25) and (4.27) in (2.3) leads to the energy:

$$E[\boldsymbol{\zeta}|\boldsymbol{\xi}] = \frac{\mu b^2}{2} \int \hat{\boldsymbol{\zeta}}^T \cdot \boldsymbol{K} \cdot \hat{\boldsymbol{\zeta}} \frac{d^2k}{(2\pi)^2} + \frac{\mu b^2}{2} \int (\hat{\boldsymbol{\zeta}} - \hat{\boldsymbol{\xi}})^T \boldsymbol{C} (\hat{\boldsymbol{\zeta}} - \hat{\boldsymbol{\xi}}) \frac{d^2k}{(2\pi)^2} - b \int \hat{\boldsymbol{S}}^T \hat{\boldsymbol{\zeta}} \frac{d^2k}{(2\pi)^2} \tag{4.29}$$

In this expression,

$$C_{\alpha\beta} = \frac{c_{ik}}{b^2} b_i^\alpha b_k^\beta \tag{4.30}$$

and S_α is the resolved shear stress in the plane in the direction $\boldsymbol{b}^\alpha$

$$S_\alpha = \frac{b_i^\alpha}{b} \sigma_{ij} m_j \tag{4.31}$$

The stable configurations of the dislocation ensemble may be identified with the relative minima of the energy (4.29):

$$\inf_{\boldsymbol{\zeta} \in Y} \inf_{\boldsymbol{\xi} \in X} E[\boldsymbol{\zeta}|\boldsymbol{\xi}] \tag{4.32}$$

We seek to express the energy of the dislocation ensemble directly in terms of $\boldsymbol{\xi}$. At this point we may invert the order of minimization in (4.32), which results in the minimization problem:

$$\inf_{\boldsymbol{\xi}\in X} E[\boldsymbol{\xi}] \tag{4.33}$$

where

$$E[\boldsymbol{\xi}] = \inf_{\boldsymbol{\zeta}\in Y} \frac{\mu b^2}{2} \int \hat{\boldsymbol{\zeta}}^T \cdot \boldsymbol{K} \cdot \hat{\boldsymbol{\zeta}} \frac{d^2k}{(2\pi)^2} + \frac{\mu b^2}{2} \int (\hat{\boldsymbol{\zeta}} - \hat{\boldsymbol{\xi}})^T \boldsymbol{C} (\hat{\boldsymbol{\zeta}} - \hat{\boldsymbol{\xi}}) \frac{d^2k}{(2\pi)^2} - b \int \hat{\boldsymbol{S}}^T \hat{\boldsymbol{\zeta}} \frac{d^2k}{(2\pi)^2} \tag{4.34}$$

Minimization with respect to $\boldsymbol{\zeta}$ gives

$$\hat{\boldsymbol{\zeta}} = (\boldsymbol{K} + \boldsymbol{C})^{-1} \boldsymbol{C} \hat{\boldsymbol{\xi}} + (\boldsymbol{K} + \boldsymbol{C})^{-1} \hat{\boldsymbol{S}} \tag{4.35}$$

Replacing (4.35) in (4.29) leads to a linear problem in $\boldsymbol{\xi}$ that can be solved analytically.

$$E[\boldsymbol{\xi}] = \frac{\mu b^2}{2} \int \hat{\boldsymbol{\xi}}^T (\boldsymbol{C} - \boldsymbol{C} (\frac{d}{2}\boldsymbol{K} + \boldsymbol{C})^{-1} \boldsymbol{C}) \hat{\boldsymbol{\xi}} \, \frac{d^2k}{(2\pi)^2} - b \int \boldsymbol{S}^T (\boldsymbol{K} + \boldsymbol{C})^{-1} \boldsymbol{C} \hat{\boldsymbol{\xi}} \, \frac{d^2k}{(2\pi)^2} + E_0 \tag{4.36}$$

where E_0 is independent of $\boldsymbol{\xi}$ and represents the elastic energy of the crystal in absence of dislocations,

$$E_0 = -\frac{1}{2} \boldsymbol{S}^T (\boldsymbol{K} + \boldsymbol{C})^{-1} \boldsymbol{S} \tag{4.37}$$

The dislocation network is defined by Equation (4.36) with the constraint that the displacement $\boldsymbol{\delta}$ in the crystal boundary is a rotation and that it is a stress free surface. We define a system of axis such that x_3 is orthogonal to the plane, in this system any displacement that cames from a rotation for a small angle can be expressed as

$$\boldsymbol{\delta}_c = \theta(-x_2, x_1, 0) \tag{4.38}$$

where θ is the rotation angle and the slip in the plane of the grain boundary is

$$\boldsymbol{\delta} = \sum_{\alpha} \boldsymbol{b}^{\alpha} \xi^{\alpha} \tag{4.39}$$

$$= b\boldsymbol{A} \cdot \boldsymbol{\xi} \tag{4.40}$$

The optimization of the phase field in the crystal boundary may be reduced to a minimization problem with a constraint:

$$\min_{\boldsymbol{\xi}} \int \frac{\mu b^2}{2d} \hat{\boldsymbol{\xi}}^T (\boldsymbol{C} - \boldsymbol{C}(\frac{d}{2}\boldsymbol{K} + \boldsymbol{C})^{-1}\boldsymbol{C})\hat{\boldsymbol{\xi}} \frac{d^2k}{(2\pi)^2} \tag{4.41}$$

subject to

$$\int (\boldsymbol{A}\boldsymbol{\xi} - \boldsymbol{\delta}_c) d^2x = 0 \tag{4.42}$$

We use a Metropolis Monte Carlo algorithm in a periodic cell to obtain the configurations that satisfy the constrained minimization problem (84; 69; 71).

4.5 Simulation of twist boundaries

Here, we apply the general framework developed in the foregoing to the simulation of a twist grain boundary. To this end we consider a two-dimensional cell of size $L = 2 \times 10^{-6} m$ with periodic boundary conditions. The applied resolved shear stress is zero in the plane. The constraint (4.42) was applied in a circle of radii $R = L/4$ inside the periodic cell. In the present simulations the magnitude of the materials parameters were chosen to represent copper ($\mu = 5.5 \times 10^{10} N/m^2$, $\nu = 0.324$ and $|\boldsymbol{b}| = 2.56 \times 10^{-10} m$).

The objective is to characterize the dislocation patterns that arise in response to the misfit of the two crystals in a grain boundary. In this model the topology of the ensemble is governed by i) the interaction between dislocations, ii) the line tension effect resulting from the core structure of the dislocations, iii) the formation of junctions; and iv) the angle of rotation between both crystals.

4.5.1 The Monte Carlo algorithm

The constrained minimization problem was solved with a Metropolis Monte Carlo algorithm (84; 69; 71). The interaction energy (Equation (4.41)) is computed in the Fourier space and the constraint given by Equation (4.42) in the real space. In order to obtain the equilibrium configurations we apply a Metropolis Monte Carlo algorithm that leads to a probability distribution $e^{-\beta \mathcal{L}[\boldsymbol{\xi}, \boldsymbol{\lambda}]}$ with $\beta = 1/kT$ and $\mathcal{L}[\boldsymbol{\xi}, \boldsymbol{\lambda}]$ is the Lagrangian

$$\mathcal{L}[\boldsymbol{\xi},\boldsymbol{\lambda}] = \int \frac{\mu b^2}{2d}\hat{\boldsymbol{\xi}}^T(\boldsymbol{C}-\boldsymbol{C}(\frac{d}{2}\boldsymbol{K}+\boldsymbol{C})^{-1}\boldsymbol{C})\hat{\boldsymbol{\xi}}\frac{d^2k}{(2\pi)^2} - \boldsymbol{\lambda}\int(\boldsymbol{A}\boldsymbol{\xi}-\boldsymbol{\delta}_c)d^2x \tag{4.43}$$

where $\boldsymbol{\lambda}$ are Lagrange multipliers. We start with high temperature to let the system to relax and then we lower the temperature in order to find the configurations that minimize the energy, this process is denoted simulated annealing.

4.5.2 Square networks

For this model we consider the axis x_3 aligned with the rotation axis of the crystal boundary $[1,0,0]$. In this system of coordinates the Burgers vectors in the plane are

$$\boldsymbol{b}_1 = \frac{b}{2}(1,0,0) \tag{4.44}$$

$$\boldsymbol{b}_2 = \frac{b}{2}(0,1,0) \tag{4.45}$$

With these configuration $\boldsymbol{A}$ and $\boldsymbol{K}$ become

$$\boldsymbol{A} = \begin{pmatrix} 1 & 0 \\ 0 & 1 \end{pmatrix} \tag{4.46}$$

$$\boldsymbol{K} = \begin{pmatrix} \frac{k_2^2}{\sqrt{k_1^2+k_2^2}} + \frac{1}{1-\nu}\frac{k_1^2}{\sqrt{k_1^2+k_2^2}} & \frac{k_1k_2}{\sqrt{k_1^2+k_2^2}}\frac{\nu}{2-2\nu} \\ \frac{k_1k_2}{\sqrt{k_1^2+k_2^2}}\frac{\nu}{2-2\nu} & \frac{k_1^2}{\sqrt{k_1^2+k_2^2}} + \frac{1}{1-\nu}\frac{k_2^2}{\sqrt{k_1^2+k_2^2}} \end{pmatrix} \tag{4.47}$$

Figure 4.7 shows the resulting patterns for angles of rotation $\theta = 0.05$ and $\theta = 0.01$. In the plot the dislocations lines are identified with the lines across which the phase-field jumps by one. The dislocation density is induced by the rotation angle θ and the dislocation spacing decreases with an increasing angle, in agreement with Equation (4.3). In agreement with theory (33) and observation (see Figure 4.5) square nets in their equilibrium configuration lie in the cubic plane. All dislocations have pure screw orientations as it is shown in Figure 4.7.

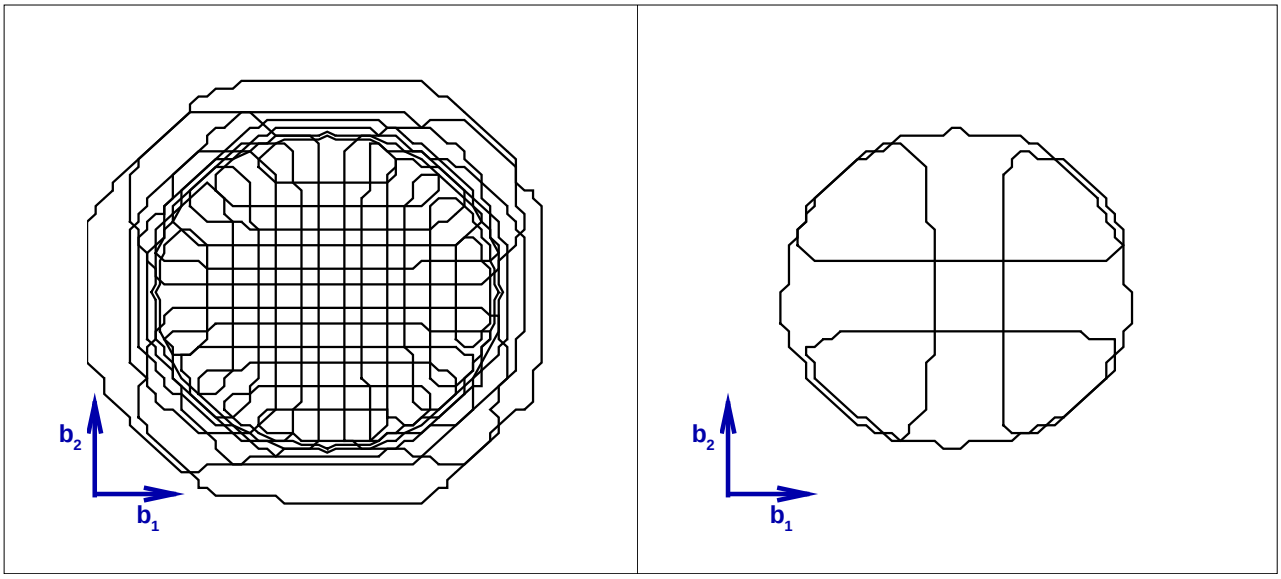

(a) Square net $\theta = 0.05$ (b) Square net $\theta = 0.01$

Figure 4.7: Stable configuration of screw dislocations in a twist grain boundary.

4.5.3 Hexagonal networks

According to theory (32; 2; 33), the plane in which the perfect hexagonal net should lie is the $(1, 1, 1)$ plane and the rotation axis the $[1, 1, 1]$. Here we consider the x_3 axis parallel to the rotation axis, in this coordinate system the Burgers vectors are

$$\boldsymbol{b}_1 = b(\cos(\pi/3), \sin(\pi/3), 0) \tag{4.48}$$

$$\boldsymbol{b}_2 = b(\cos(\pi/3), -\sin(\pi/3), 0) \tag{4.49}$$

$$\boldsymbol{b}_3 = (\boldsymbol{b}_1 + \boldsymbol{b}_2) \tag{4.50}$$

Only $\boldsymbol{b}_1$ and $\boldsymbol{b}_2$ are linearly independent. Therefore any displacement $\boldsymbol{\delta}$ in the plane of the grain boundary can be written as a combination only of ξ_1 and ξ_2. Under these conditions $\boldsymbol{A}$ and $\boldsymbol{K}$ result

$$\boldsymbol{A} = \begin{pmatrix} \cos(\pi/3) & \cos(\pi/3) \\ \sin(\pi/3) & -\sin(\pi/3) \end{pmatrix} \tag{4.51}$$

$$\boldsymbol{K} = \begin{pmatrix} \frac{k_2^2(4-\nu)+k_1^1(4-3\nu)-2\sqrt{3}\nu k_1 k_2}{8(1-\nu)\sqrt{k_1^2+k_2^2}} & \frac{k_2^2(2+\nu)+k_1^1(2-3\nu)}{8(1-\nu)\sqrt{k_1^2+k_2^2}} \\ \frac{k_2^2(2+\nu)+k_1^1(2-3\nu)}{8(1-\nu)\sqrt{k_1^2+k_2^2}} & \frac{k_2^2(4-\nu)+k_1^1(4-3\nu)+2\sqrt{3}\nu k_1 k_2}{8(1-\nu)\sqrt{k_1^2+k_2^2}} \end{pmatrix} \tag{4.52}$$

Figure 4.8 shows the stable dislocation configurations for $\theta = 0.05$ and $\theta = 0.01$. The patterns observed consists of a hexagonal grid of screw dislocations having Burgers vectors $\boldsymbol{b}_1$, $\boldsymbol{b}_2$ and $\boldsymbol{b}_3$ in agreement with experimental observation (Figure 4.6).

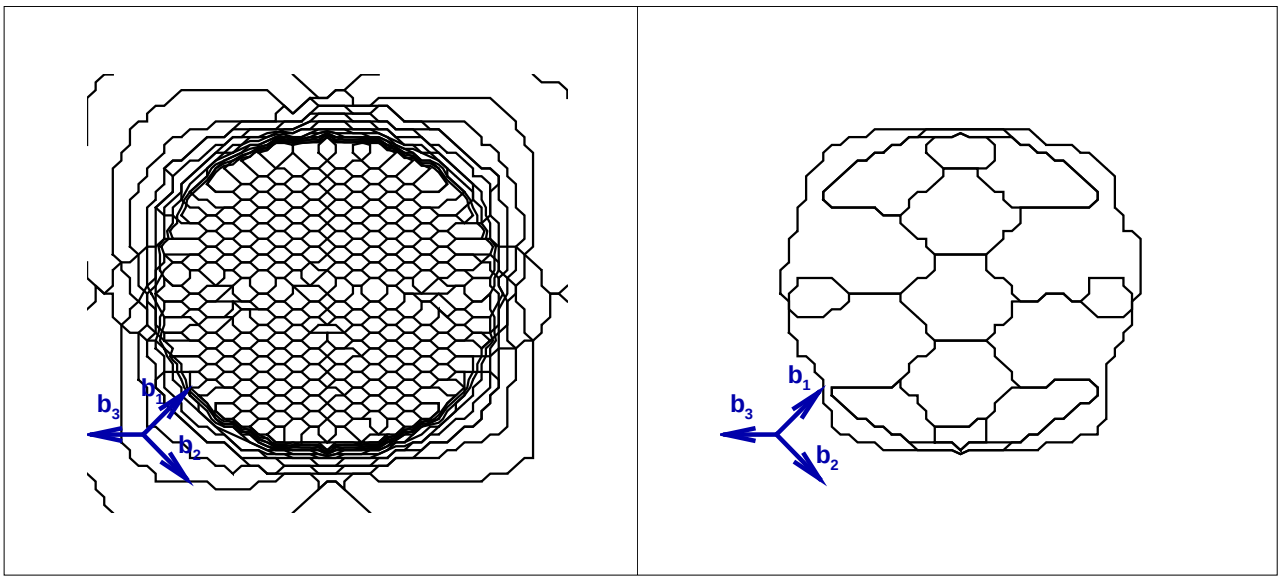

(a) Hexagonal net $\theta = 0.05$ (b) Hexagonal net $\theta = 0.01$

Figure 4.8: Stable configuration of screw dislocations in a twist grain boundary.

4.5.4 Dislocation density

The dislocation spacing can be obtained directly from Frank's relations, combining Equations (4.5), (4.6) and (4.13).

$$c_1\boldsymbol{b}_1 + c_2\boldsymbol{b}_2 = \frac{\theta}{|\boldsymbol{b}_1 \times \boldsymbol{b}_2|}\left(\boldsymbol{b}_1(\boldsymbol{b}_2 \cdot \boldsymbol{V}) - \boldsymbol{b}_2(\boldsymbol{b}_1 \cdot \boldsymbol{V})\right) \tag{4.53}$$

From the simulations and in agreement with experimental observation, all the dislocations in the network are pure screw. Therefore in order to calculate the spacing between dislocations D_1 and D_2, we take $\boldsymbol{V}$ perpendicular to $\boldsymbol{b}_1$ and $\boldsymbol{b}_2$, respectively. The sets of dislocations are parallel and their spacing are

$$D_1 = \frac{|\boldsymbol{V}|}{c_1} = \frac{|\boldsymbol{b}_1|}{\theta} \tag{4.54}$$

$$D_2 = \frac{|\boldsymbol{V}|}{c_2} = \frac{|\boldsymbol{b}_2|}{\theta} \tag{4.55}$$

Figure 4.9 shows the the spacing for different rotation angles θ for the hexagonal and square network. For both networks the computed spacing is in excellent agreement with theory and experimental observation (32; 2; 33).

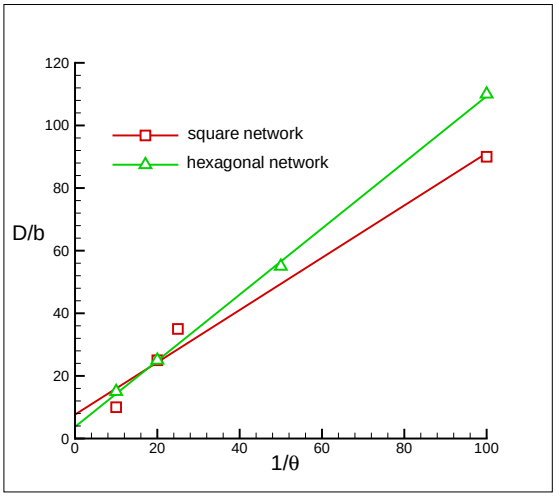

Figure 4.9: Dislocation spacing.

4.6 Summary and concluding remarks

The phase-field representation furnishes an effective and simple method for obtaining stable dislocation configurations and tracking individual dislocations. The energetics accounted for in the theory

include the core energy, represented by a piecewise quadratic potential (7), the long-range elastic interaction between the dislocations in the plane of the grain boundary and the line anisotropy. The theory predicts the true dislocation configurations for a given boundary, because the crossing dislocations interact and react to form configurations of lower energy. This is a clear advantage to the theory which treats non-interacting dislocations and where the stable configurations are found by recurse of interaction models in analogy to surface tension (3; 83; 2). The theory predicts the formation of patterns that are in agreement with the ones observed in twist boundaries (32; 2). The dislocations in the patterns are all pure screw, and the spacing between dislocations D is $|\boldsymbol{b}|/\theta$, for small angles θ in agreement with theory. Simultaneously with the stable configurations the theory naturally predicts the equilibrium dislocation density independently of initial values or sources.

Chapter 5

Conclusions and future work

We have developed a phase-field theory of dislocations which furnishes a simple and effective means of tracking the motion of large numbers of dislocations within discrete slip planes. The theory predicts a range of behaviors which are in qualitative agreement with observation.

At zero temperature, the equilibrium configurations of dislocations are obtained by direct minimization of the energy. The resulting variational problem is strongly *nonlinear* and *nonconvex*. In addition, the variational problem is *nonlocal*, owing to the presence of long-range elastic interactions. These attributes render the energy minimization problem mathematically nontrivial and confer its solutions a rich structure. Despite these difficulties, the choice of a piecewise quadratic Peierls potential lends the problem analytical tractability and a good deal of progress toward the solution can be made analytically.

We have developed a generalization of classical statistical mechanics which describes the behavior of dissipative systems. The ability of the model to allow for hysteresis and to predict its temperature dependence is noteworthy. This theory is applied to the phase-field model of dislocations using a Path Integral Metropolis Monte Carlo algorithm and a mean field approximation. The stress-strain curves show different behavior for different strain rates and temperatures. The system becomes harder with increasing strain rate and decreasing temperature in agreement with experimental observations (29; 30; 31; 1).

The extension of the phase-field to a multifield model allows to study the interaction of dislocations with different burgers vectors an in different slip planes. We apply the multifield model to model the dislocation arrangements in twist grain boundaries. The theory predicts the formation of square and hexagonal patterns that are in agreement with the ones observed in twist boundaries

(32; 2). The dislocations in the patterns are all pure screw, and the spacing between dislocations D is $|\boldsymbol{b}|/\theta$, for small angles θ in agreement with the theory. Simultaneously with the stable configurations the theory naturally predicts the dislocation density with no initial dislocations or sources.

However, in order to build additional physical realism into the theory, a number of extensions and enhancements immediately suggest themselves, to wit:

1. It should be possible, within the general framework outlined in Chapter 2, to formulate a fully three-dimensional theory of crystallographic slip accounting for the full complement of slip systems in a crystal class and, e.g., an infinite stack of uniformly spaced slip planes within each slip system.

2. A topological restriction of the phase-field representation of crystallographic slip, as presented here, is that, since the dislocation lines follow the level contours of a scalar phase field, they must necessarily trace closed loops or form networks of zero net Burgers vector. This topological constraint precludes the effective representation of cross slip, and therefore points to the need for nontrivial mathematical extensions of the theory.

3. As presented here, the theory accounts for the edge/screw line-energy anisotropy predicted by linear elasticity. However, this type of anisotropy does not suffice to model the vastly different behavior of screw and edge segments observed in bcc crystals, which largely owes to differences in the mobility of both types of segments. Within the present theory, a proper accounting of this effect can be achieved simply by allowing the Peierls stress to depend on the gradient $\nabla\xi$ of the phase field, which describes the local orientation of the dislocation segments within the slip plane.

4. Using homogenization methods should be possible to construct a dislocation based model of plasticity obtained from the phase-field model. The introduction of this model in the simulation of real materials will predict macroscopic characteristics of the system (deformation, hardening) as well as the evolution of the dislocation density which is essential for a physically based description of plastic flow.

Finally, the fact that the theory permits the reconstruction of the full dislocation ensemble

from the value of the phase-field at the obstacle sites can hardly be overemphasized. Indeed, the geometry of each dislocation line is given by the theory analytically and in close form. In addition, the same analytical treatment endows each dislocation with a well-defined core, which effectively regularizes—and eliminates the divergences which afflict—linear elastic dislocation theory. The practical effect of this analytical tractability is the elimination of any need for the use of numerical grids to discretize the slip plane or, worse, the entire crystal. Since the theory targets the equilibrium configurations of the dislocation ensemble directly, no costly resolution of transients, often introduced as numerical artifacts in order to advance the solution in time and requiring the use of exceedingly small time steps, is required. These attributes render the complexity of the calculations required by the theory, in its present state of development, commensurate with the number of obstacles. This drastic reduction in complexity may open the way for embedding the theory within a finite-deformation formulation of single-crystal elastic-plastic behavior (e.g., (26; 28)), with a view to its use in large-scale finite element calculations of macroscopic samples.

Bibliography

[1] T. Suzuki, S. Takeuchi, and H. Yoshinaga. *Dislocation dynamics and plasticity.* Springer Verlag, 1990.

[2] S. Amelinckx. Dislocation patterns in potassium chloride. *Acta Metallurgica*, 6:34–58, 1958.

[3] J. P. Hirth and J. Lothe. *Theory of Dislocations.* McGraw-Hill, New York, 1968.

[4] R. J. Asaro. Micromechanics of crystals and polycrystals. *Advances in Applied Mechanics*, 23:1–115, 1983.

[5] U. F. Kocks, A. S. Argon, and M. F. Ashby. Thermodynamics and kinetics of slip. In B. Chalmers, J. W. Christian, and T. B. Massalski, editors, *Progress in Materials Science*, volume 19, 1975.

[6] R. W. Balluffi and A. V. Granato. Dislocations, vacancies and interstitials. In F. R. N. Nabarro, editor, *Dislocations in solids*, pages 1–133. North Holland, 1979.

[7] M. Ortiz and R. Phillips. Nanomechanics of defects in solids. *Advances in Applied Mechanics*, 36:1–79, 1999.

[8] R. Phillips, D. Rodney, V. Shenoy, E. Tadmor, and M. Ortiz. Hierarchical models of plasticity: dislocation nucleation and interaction. *Modelling and Simulation in Materials Science and Engineering*, 7(5):769–780, 1999.

[9] M. Ortiz, A. M. Cuitino, J. Knap, and M. Koslowski. Mixed atomistic continuum models of material behavior: The art of transcending atomistics and informing continua. *MRS Bulletin*, 26(3):216–221, 2001.

[10] A. M. Cuitino, L. Stainier, G. F. Wang, A. Strachan, T. Cagin, W. A. Goddard, and M. Ortiz. A multiscale approach for modeling crystallyne solids. *Journal of computer-aided materials design*, 8:127–149, 2002.

[11] A. G. Khachaturyan. *Theory of structural transformation in solids.* John Wiley and Sons, 1983.

[12] A. Artemev and A. G. Khachaturyan. 3d phase field model of proper martensitic transformations. *Acta Materialia*, 49, 2001.

[13] J. Muller and M. Grant. Model of surface instabilities induced by stress. *Physical Review Letters*, 82, 1999.

[14] D.N. Bhate, A. Kumar, and A. F. Bower. Diffuse interface model for electromigration and stress voiding. *Journal of Applied Physics*, 87:1712–1721, 2000.

[15] L. O. Eastgate, J. P. Sethna, M. Rauscher, T. Cretegny, C. S. Chen, and C. R. Myers. Fracture in mode i using a conserved phase-field model. *Physical Review E*, 65, 2002.

[16] A. Finel and D. Rodney. Phase field methods and dislocations. *MRS Fall meeting, Boston*, 2000.

[17] Y.U Wang, Y.M Jin, A.M. Cuitiño, and A. G. Khachaturyan. Phase field microelasticity theory and modeling of multiple dislocation dynamics. *Applied Physics Letters*, 78(16):2324–2326, 2001.

[18] M. Koslowski, A. Cuitiño, and M. Ortiz. A phase-field theory of dislocations dynamics, strain hardening and hysteresis in ductile single crystals. *Journal of the Mechanics and Physics of Solids*, 50(12):2957–2635, 2001.

[19] L. P. Kubin and G. Canova. The modelling of dislocation patterns. *Scripta Metallurgica et Materialia*, 27:957–962, 1992.

[20] N. M. Ghoniem, S.H Tong, and L.Z. Sun. Parametric dislocation dynamics: A thermodynamics-based approach to investigations of mesoscopic plastic deformation. *Physical Review B*, 61(2):913–927, 2000.

[21] H. M. Zbib, M. Rhee, and J. P. Hirth. On plastic deformation and the dynamics of 3d dislocations. *International Journal of Mechanical Sciences*, 40, 1998.

[22] M. Rhee, H. M. Zbib, , J. P. Hirth, and T. Huang, H. annd dela Rubia. Models for long/short range interactions and cross slip in 3d dislocation simulation of bcc single crystals. *Modelling and Simulation in Materials Science and Engineering*, 6, 1998.

[23] M. Ortiz and E.A. Repetto. Nonconvex energy minimization and dislocation structures in ductile single crystals. *Journal of the Mechanics and Physics of Solids*, 47(2):397–462, 1999.

[24] R. Radovitzky and M. Ortiz. Error estimation and adaptive meshing in strongly nonlinear dynamic problems. *Computer Methods in Applied Mechanics and Engineering*, 172(1-4):203–240, 1999.

[25] M. Ortiz, E.A. Repetto, and L. Stainier. A theory of subgrain dislocation structures. *Journal of the Mechanics and Physics of Solids*, 48(10):2077–2114, 2000.

[26] M. Ortiz and L. Stainier. The variational formulation of viscoplastic constitutive updates. *Computer Methods in Applied Mechanics and Engineering*, 171(3-4):419–444, 1999.

[27] C. Kane, J. E. Marsden, M Ortiz, and M. West. Varaitional integrators and the newmark algorithm for conservative and dissipative mechanical systems. *International Journal for Numerical Methods in Engineering*, 49:1295–1325, 2000.

[28] A. M. Cuitiño and M. Ortiz. Computational modeling of single crystals. *Modelling and Simulation in Materials Science and Engineering*, 1:255–263, 1992.

[29] R. Lacenmann and H. Schultz. Inherent lattice hardening and interstitial solution hardening in tantalum. *Scripta Metallurgica*, 4:709–714, 1970.

[30] S. Takeuchi and K. Maeda. Slip in high purity tantalum between 0.7 and 40k. *Acta Metallurgica*, 25:1485–1490, 1977.

[31] M. Tang, L. P. Kubin, and G. R. Canova. Disocation mobility and the mechanical response of bcc single crystals: A mesoscopic approach. *Acta Materialia*, 46:3221–3235, 1998.

[32] S. Amelinckx. The direct observation of dislocation patterns in transparent crystals. In J. C. Fisher, W. G. Johnston, R. Thomson, and Vreeland T., editors, *Dislocation and mechanical properties of crystals*, pages 3–54. John Wiley, 1956.

[33] A. P. Sutton and R. W. Balluffi. *Interfaces in crystalline materials.* Oxford Science Publications, Oxford, 1995.

[34] M. Ortiz. Plastic yielding as a phase transition. *Journal of Applied Mechanics-Transactions of the ASME*, 66(2):289–298, 1999.

[35] M.I. Baskes, R.G. Hoagland, and T. Tsuji. An atomistic study of the strength of an extended-dislocation barrier. *Modelling and Simulation in Materials Science and Engineering*, 6(1):9–18, 1998.

[36] D. Rodney and R. Phillips. Structure and strength of dislocation junctions: An atomic level analysis. *Physical Review Letters*, 82(8):1704–1707, 1999.

[37] V.B. Shenoy, R.V. Kukta, and R. Phillips. Mesoscopic analysis of structure and strength of dislocation junctions in fcc metals. *Physical Review Letters*, 84(7):1491–1494, 2000.

[38] G. Xu and M. Ortiz. A variational boundary integral method for the analysis of three-dimensional cracks of arbitrary geometry modeled as continuous distributions of dislocation loops. *International Journal for Numerical Methods in Engineering*, 36:3675–3701, 1993.

[39] G. Xu. A variational boundary integral method for the analysis of three-dimensional cracks of arbitrary geometry in anisotropic elastic solids. *Journal of Applied Mechanics, ASME*, 67:403–408, 2000.

[40] E. Kröner. Berechnung der elastischen Konstanten des Vielkristalls aus den Konstanten des Einkristalls. *Zeitung der Physik*, 151:504–518, 1958.

[41] T. Mura. *Micromechanics of defects in solids.* Kluwer Academic Publishers, Boston, 1987.

[42] J. F. Nye. Some geometrical relations in dislocated crystals. *Acta Metallurgica*, 1:153–162, 1953.

[43] J.R. Rice. Dislocation nucleation from a crack tip - an analysis based on the peierls concept. *Journal of the Mechanics and Physics of Solids*, 40(2):239–271, 1992.

[44] Y.M. Sun, G.E. Beltz, and J.R. Rice. Estimates from atomic models of tension shear coupling in dislocation nucleation from a crack tip. *Materials Science and Engineering*, A170(1-2):67–85, 1993.

[45] M. Yamaguchi, V. Vitek, and D. Pope. Planar faults in the li_2 lattice, stability and structure. *Philosophical Magazine*, 43:1027, 1981.

[46] Y. Sun, J. R. Rice, and L. Truskinovsky. *High-Temperature ordered intermetallic alloys*, volume 213, chapter Dislocation nucleation *versus* cleavage in Ni_3Al and Ni, pages 243–248. Materials Research Society, 1991.

[47] Y.M. Juan and E. Kaxiras. Generalized stacking fault energy surfaces and dislocation properties of silicon: A first- principles theoretical study. *Philosophical Magazine*, A74(6):1367–1384, 1996.

[48] Y.M. Juan, Y.M. Sun, and E. Kaxiras. Ledge effects on dislocation emission from a crack tip: A first-principles study for silicon. *Philosophical Magazine Letters*, 73(5):233–240, 1996.

[49] A. M. Mathai and R. K. Saxena. *Generalized Hypergeometric Functions with Applications in Statistics and Physical Sciences*. Kluwer Academic Publishers, Boston, 1987.

[50] F. H. Clarke. *Optimization and Nonsmooth Analysis*. John Wiley & Sons, New York, 1983.

[51] R.Y. Rockafellar. *Convex Analysis*. Princeton University Press, Princeton, N.J., 1970.

[52] K. Hardikar, V. Shenoy, and R. Phillips. Reconciliation of atomic-level and continuum notions concerning the interaction of dislocations and obstacles. *Journal of the Mechanics and Physics of Solids*, 49:1951–1967, 2001.

[53] J. P. Sethna, K. Dahmen, S. Kartha, Krumhansl J. A., B. W. Rpberts, and Shore J. D. Hysteresis and hierarchies: dynamics of disorder-driven first-order phase transformations. *Physical Review Letters*, 70:3347–3350, 1993.

[54] M. F. Ashby. The deformation of plastically non-homogeneous alloys. In A. Kelly and R. B. Nicholson, editors, *Strengthening Methods in Crystals*, pages 137–192. Wiley, 1972.

[55] J. D. Livingston. The density and distribution of dislocations in deformed copper crystals. *Acta Metallurgica*, 10:229–239, 1962.

[56] M. Ortiz and E. P. Popov. A statistical theory of polycrystalline plasticity. *Proceedings of the Royal Society of London*, A379:439–458, 1982.

[57] J. D. Morrow. Unpublished test results, 1975.

[58] S. R. Bodner and A. Lindenfeld. Constitutive modeling of the stored energy of cold work under cyclic loading. *European Journal of Mechanics, A/Solids*, 14(3):333–348, 1995.

[59] D. Kinderlehrer and L. Ma. The hysteric event in the computation of magnetization. *Journal of Nonlinear Science*, 23:101–128, 1997.

[60] K. Dahmen, S. Kartha, A. Krumhansi, B. W. Roberts, Sethna J. P., and Shore J. D. Disorder-driven first-order phase transformations: A model of hysteresis. *Journal of Applied Physics*, 75:5946–5948, 1994.

[61] I. D. Mayergoyz. Mathematical model of hysteresis. *Physical Review Letters*, 56:1518–1521, 1986.

[62] U. Nowak. Magnetization reversal and domain structure in thin magnetic films: Theory and computer simulation. *IEEE Transactions on Magnetics*, 31:4169–4171, 1995.

[63] A. Lyberatos. Monte carlo models of the magnetization reversal in thin films with strong perpendicular anisotropy. *Journal of physics D-Applied Physics*, 33:R117–R133, 2000.

[64] Ph. Blanchard, Ph. Combe, and W. Zheng. *Mathematical and Physical Aspects of Stochastic Mechanics*. Springer-Verlag, 1987.

[65] N. G. Van Kampen. *Stochastic Processes in Physics and Chemistry*. North Holland, 1981.

[66] F. W. Wiegel. *Introduction to Path-Integral Methods in Physics and Polymer Science*. World Scientific, 1986.

[67] R. P. Feynman. *Statistical Mechanics. A set of lectures*, volume 36 of *Frontiers in Physiscs*. Addison Wesley, 13th edition, 1990.

[68] U. Nowak, J. Heimel, T. Kleinefeld, and D. Weller. Domain dynamics of magnetic films with perpendicular anysotropy. *Physical Review B*, 56:8143–8148, 1997.

[69] K. Binder, editor. *The Monte Carlo Method in Condensed Matter Physics*. Springer-Verlag, New York, 1992.

[70] D. C. Khandekar, S. V. Lawande, and K. V Bhagwat. *Path-Integral Methods and their applications*. World Scientific, 1993.

[71] J. M. Thijssen. *Computational Physics*. Cambridge University Press, 1999.

[72] R. D. Kirby, J. X. Shen, R. J. Hardy, and D. J. Sellmyer. Magnetization reversal in nanoscale magnetic films with perpendicular anisotropy. *Physical Review B*, 49:10810–10813, 1994.

[73] J. J. Binney, N. J. Dowrick, A. J. Fisher, and M. E. J. Newman, editors. *The theory of critical phenomena*. Oxford Science Publications, Oxford, 1992.

[74] D. Chandler. *Introduction to modern statistical mechanics*. Oxford University Press, New York, 1978.

[75] J. W. Christian and B. C. Masters. Low-temperature deformation of body-centered cubic metals. yield and flow stress measurements. *Philosophical Transactions of the Royal Society of London A*, 281(138):223–238, 1964.

[76] R. L. Fleischer. Rapid solution hardening, dislocation mobility, and the flow stress of crystals. *Journal of Applied Physics*, 33(12):3504–3508, 1962.

[77] D. Kuhlmann-Wilsdorf and J. H. van der Merve. *Materials Science and Engineering*, 55:79, 1982.

[78] A. N. Gulluoglu, D. J. Srolovitz, R. LeSar, and P. S. Lomdahl. Dislocation distributions in two dimensions. *Scripta Metallurgica*, 23:1347–1352, 1989.

[79] N. Argaman, O. Levy, and G. Makov. Dislocation pattern formation-simulations of annealing in two dimensions. *J. Phys. IV*, 11:61–68, 2001.

[80] J. P. Hirth and B. Carnahan. Anisotropic elastic fields of twist boundaries. *Acta Metallurgica et Materialia*, 40:1237–1242, 1991.

[81] V. Bulatov and Cai W. Nodal effects in dislocation mobility. *Physical Review Letters*, 11(89):115501, 2002.

[82] F.R.N. Nabarro. Sequence of dislocation patterns. *Materials Science and Engineering*, A317:12–16, 2001.

[83] D. Hull and D. J. Bacon. *Introduction to Dislocations*, volume 37 of *International Series on Materials Science and Technology*. Elsevier Science Inc., 3rd edition, 1984.

[84] K. Binder, editor. *Monte Carlo Methods in Statistical Physics*. Springer-Verlag, New York, 2nd edition, 1986.